

## MOLECULAR HYDROGEN AND GLOBAL STAR FORMATION RELATIONS IN GALAXIES

BRANT E. ROBERTSON<sup>1,2,3</sup> AND ANDREY V. KRAVTSOV<sup>1,2</sup>

*Draft version November 21, 2021*

### ABSTRACT

We use hydrodynamical simulations of disk galaxies to study relations between star formation and properties of the molecular interstellar medium (ISM). We implement a model for the ISM that includes low-temperature ( $T < 10^4$  K) cooling, directly ties the star formation rate to the molecular gas density, and accounts for the destruction of  $H_2$  by an interstellar radiation field from young stars. We demonstrate that the ISM and star formation model simultaneously produces a spatially-resolved molecular-gas surface density Schmidt-Kennicutt relation of the form  $\Sigma_{\text{SFR}} \propto \Sigma_{\text{H}_2}^{n_{\text{mol}}}$  with  $n_{\text{mol}} \approx 1.4$  independent of galaxy mass, and a total gas surface density – star formation rate relation  $\Sigma_{\text{SFR}} \propto \Sigma_{\text{gas}}^{n_{\text{tot}}}$  with a power-law index that steepens from  $n_{\text{tot}} \sim 2$  for large galaxies to  $n_{\text{tot}} \gtrsim 4$  for small dwarf galaxies. We show that deviations from the disk-averaged  $\Sigma_{\text{SFR}} \propto \Sigma_{\text{gas}}^{1.4}$  correlation determined by Kennicutt (1998) owe primarily to spatial trends in the molecular fraction  $f_{\text{H}_2}$  and may explain observed deviations from the global Schmidt-Kennicutt relation. In our model, such deviations occur in regions of the ISM where the fraction of gas mass in molecular form is declining or significantly less than unity. Long gas consumption time scales in low-mass and low surface brightness galaxies may owe to their small fractions of molecular gas rather than mediation by strong supernovae-driven winds. Our simulations also reproduce the observed relations between ISM pressure and molecular fraction and between star formation rate, gas surface density, and disk angular frequency. We show that the Toomre criterion that accounts for both gas and stellar densities correctly predicts the onset of star formation in our simulated disks. We examine the density and temperature distributions of the ISM in simulated galaxies and show that the density probability distribution function (PDF) generally exhibits a complicated structure with multiple peaks corresponding to different temperature phases of the gas. The overall density PDF can be well-modeled as a sum of lognormal PDFs corresponding to individual, approximately isothermal phases. We also present a simple method to mitigate numerical Jeans fragmentation of dense, cold gas in Smoothed Particle Hydrodynamics codes through the adoption of a density-dependent pressure floor.

*Subject headings:* Galaxies, Star Formation

### 1. INTRODUCTION

Galaxy formation presents some of the most important and challenging problems in modern astrophysics. A basic paradigm for the dissipational formation of galaxies from primordial fluctuations in the density field has been developed (e.g. White & Rees 1978; Blumenthal et al. 1984; White & Frenk 1991), but many of the processes accompanying galaxy formation are still poorly understood. In particular, star formation shapes the observable properties of galaxies but involves a variety of complicated dynamical, thermal, radiative, and chemical processes on a wide range of scales (see McKee & Ostriker 2007, for a review). Observed galaxies exhibit large-scale correlations between their global star formation rate (SFR) surface density  $\Sigma_{\text{SFR}}$  and average gas surface density  $\Sigma_{\text{gas}}$  (Kennicutt 1989, 1998), and these global correlations serve as the basis for treatments of star formation in many models of galaxy formation. While such models have supplied important insights, detailed observations of galaxies have recently provided evidence that the molecular, rather than the total, gas surface density is the primary driver of global star formation in galaxies (e.g., Wong & Blitz 2002; Boissier et al. 2003; Heyer et al. 2004; Boissier et al. 2007; Calzetti et al. 2007; Kennicutt et al. 2007).

In this study, we adopt an approach in which empirical and theoretical knowledge of the star formation efficiency (SFE) in dense, molecular gas is used as the basis for a star formation model in hydrodynamical simulations of disk galaxy evolution. This approach requires modeling processes that shape properties of the dense phase of the interstellar medium (ISM) in galaxies. The purpose of this paper is to present such a model.

Stellar populations in galaxies exhibit salient trends of colors and metallicities with galaxy luminosity (e.g., Kauffmann et al. 2003; Blanton et al. 2005; Cooper et al. 2007). In the hierarchical structure formation scenario these trends should emerge through the processes of star formation and/or stellar feedback in the progenitors of present-day galaxies. Observationally, ample evidence suggests that the efficiency of the conversion of gas into stars depends strongly and non-monotonically on mass of the system. For example, the faint-end of the galaxy luminosity function has a shallow slope ( $\alpha_L \approx 1.0 - 1.3$ , e.g., Blanton et al. 2001, 2003) compared to the steeper mass function of dark matter halos ( $\alpha_{\text{DM}} \approx 2$ , e.g., Press & Schechter 1974; Sheth & Tormen 1999), indicating a decrease in SFE in low-mass galaxies. At the same time, the neutral hydrogen (HI) and baryonic mass functions may be steeper than the luminosity function ( $\alpha_{\text{HI}} \approx 1.3 - 1.5$ , e.g., Rosenberg & Schneider 2002; Zwaan et al. 2003). The baryonic Tully & Fisher (1977) relation is continuous down to extremely low-mass dwarf galaxies (e.g., McGaugh 2005; Geha et al. 2006), indicating that the fractional baryonic content of galaxies of different mass is similar.

<sup>1</sup> Kavli Institute for Cosmological Physics, and Department of Astronomy and Astrophysics, University of Chicago, 933 East 56th Street, Chicago, IL 60637, USA

<sup>2</sup> Enrico Fermi Institute, 5640 South Ellis Avenue, Chicago, IL 60637, USA

<sup>3</sup> Spitzer Fellow

Hence, low-mass galaxies that are unaffected by environmental processes are gas-rich, yet often form stars inefficiently.

While feedback processes from supernovae and AGN (e.g., Brooks et al. 2007; Sijacki et al. 2007), or the efficiency of gas cooling and accretion (Dekel & Birnboim 2006, 2008), may account for part of these trends, the SFE as a function of galaxy mass may also owe to intrinsic ISM processes (e.g., Tassis et al. 2008; Kaufmann et al. 2007). To adequately explore the latter possibility, a realistic model for the conversion of gas into stars in galaxies is needed.

Traditionally, star formation in numerical simulations of galaxy formation is based on the empirical Schmidt-Kennicutt (SK) relation (Schmidt 1959; Kennicutt 1989, 1998), in which star formation rate is a *universal* power-law function of the total disk-averaged or global gas surface density:  $\Sigma_{\text{SFR}} \propto \Sigma_{\text{gas}}^{n_{\text{tot}}}$  with  $n_{\text{tot}} \approx 1.4$  describing the correlation for the entire population of normal and starburst galaxies. However, growing observational evidence indicates that this relation may not be universal on smaller scales within galaxies, especially at low surface densities.

Estimates of the slope of the SK relation within individual galaxies exhibits significant variations. For example, while Schuster et al. (2007) and Kennicutt et al. (2007) find  $n_{\text{tot}} \approx 1.4$  for the molecular-rich galaxy M51a, similar estimates in other large, nearby galaxies (including the Milky Way (MW); Misiriotis et al. 2006) range from  $n_{\text{tot}} \approx 1.2$  to  $n_{\text{tot}} \approx 3.5$  (Wong & Blitz 2002; Boissier et al. 2003) depending on dust-corrections and fitting methods. The disk-averaged total gas SK relation for normal (non-starburst) galaxies also has a comparably steep slope of  $n_{\text{tot}} \approx 2.4$ , with significant scatter (Kennicutt 1998). While the variations in the  $\Sigma_{\text{SFR}} - \Sigma_{\text{gas}}$  correlation may indicate systematic uncertainties in observational measurements, intrinsic variations or trends in galaxy properties may also induce differences between the global relation determined by Kennicutt (1998) and the  $\Sigma_{\text{SFR}} - \Sigma_{\text{gas}}$  correlation in individual galaxies.

Galaxies with low gas surface densities, like dwarfs or bulgeless spirals, display an even wider variation in their star formation relations. Heyer et al. (2004) and Boissier et al. (2003) show that in low-mass galaxies the SFR dependence on the total gas surface density exhibits a power-law slope  $n_{\text{tot}} \approx 2 - 3$  that is considerably steeper than the global Kennicutt (1998) relation slope of  $n_{\text{tot}} \approx 1.4$ . Further, star formation in the low-surface density outskirts of galaxies also may not be universal. Average SFRs appear to drop rapidly at gas surface densities of  $\Sigma_{\text{gas}} \lesssim 5 - 10 M_{\odot} \text{pc}^{-2}$  (Hunter et al. 1998; Martin & Kennicutt 2001), indicating that star formation may be truncated or exhibit a steep dependence on the gas surface density. The existence of such threshold surface densities have been proposed on theoretical grounds (Kennicutt 1998; Schaye 2004), although recent GALEX results using a UV indicator of star formation suggest that star formation may continue at even lower surface densities (Boissier et al. 2007). Star formation rates probed by damped Lyman alpha absorption (DLA) systems also appear to lie below the Kennicutt (1998) relation, by an order of magnitude (Wolfe & Chen 2006; Wild et al. 2007), which may indicate that the relation between SFR and gas surface density in DLA systems differs from the local relation measured at high  $\Sigma_{\text{gas}}$ .

In contrast, observations generally show that star formation in galaxies correlates strongly with *molecular* gas, especially with the highly dense gas traced by HCN emission (Gao & Solomon 2004; Wu et al. 2005). The power-

law index of the SK relation connecting the SFR to the surface density of molecular hydrogen consistently displays a value of  $n_{\text{mol}} \approx 1.4$  and exhibits considerably less galaxy-to-galaxy variation (Wong & Blitz 2002; Murgia et al. 2002; Boissier et al. 2003; Heyer et al. 2004; Matthews et al. 2005; Leroy et al. 2005, 2006; Gardan et al. 2007). Molecular gas, in turn, is expected to form in the high-pressure regions of the ISM (Elmegreen 1993a; Elmegreen & Parravano 1994), as indicated by observations (Blitz & Rosolowsky 2004, 2006; Gardan et al. 2007).

Analytical models and numerical simulations that tie star formation to the fraction of gas in the dense ISM are successful in reproducing many observational trends (e.g., Elmegreen 2002; Kravtsov 2003; Krumholz & McKee 2005; Li et al. 2005b, 2006; Tasker & Bryan 2006, 2007; Krumholz & Thompson 2007; Wada & Norman 2007; Tassis 2007). Recently, several studies have explored star formation recipes based on molecular hydrogen. Pelupessy et al. (2006) and Booth et al. (2007) implemented models for  $\text{H}_2$  formation in gaseous disks and used them to study the molecular content and star formation in galaxies. However, these studies focused on the evolution of galaxies of a single mass and did not address the origin of the SK relation, its dependence on galaxy mass or structure, or its connection to trends in the local molecular fraction.

Our study examines the SK relation critically, including its dependence on the structural and ISM properties of galaxies of different masses, to explain the observed deviations from the global SK relation, to investigate other connections between star formation and disk galaxy properties such as rotation or gravitational instability, and to explore how the temperature and density structure of the ISM pertains to the star formation attributes of galaxies.

To these ends, we develop a model for the ISM and star formation whose key premise is that star formation on the scales of molecular clouds ( $\sim 10$  pc) is a function of molecular hydrogen density with a universal SFE per free-fall time (e.g., Krumholz & Tan 2007). Molecular hydrogen, which we assume to be a proxy for dense, star forming gas, is accounted for by calculating the local  $\text{H}_2$  fraction of gas as a function of density, temperature, and metallicity using the photoionization code Cloudy (Ferland et al. 1998) to incorporate  $\text{H}_2$ -destruction by the UV radiation of local young stellar populations. We devise a numerical implementation of the star formation and ISM model, and perform hydrodynamical simulations to study the role of molecular gas in shaping global star formation relations of self-consistent galaxy models over a representative mass range.

The results of our study show that many of the observed global star formation correlations and trends can be understood in terms of the dependence of molecular hydrogen abundance on the local gas volume density. We show that the physics controlling the abundance of molecular hydrogen and its destruction by the interstellar radiation field (ISRF) play a key role in shaping these correlations, in agreement with earlier calculations based on more idealized models of the ISM (Elmegreen 1993a; Elmegreen & Parravano 1994). While our simulations focus on the connection between the molecular ISM phase and star formation on galactic scales, the formation of molecular hydrogen has also been recently studied in simulations of the ISM on smaller, subgalactic scales (Glover & Mac Low 2007; Dobbs & Bonnell 2007). These simulations are complementary to the calculations presented in our study and could be used as input to improve the molec-

ular ISM model we present.

The paper is organized as follows. The simulation methodology, including our numerical models for the ISM, interstellar radiation field, and simulated galaxies, is presented in §2. The results of the simulations are presented in §3, where the simulated star formation relations in galactic disks and correlations of the molecular fraction with the structure of the ISM are examined. We discuss our results in §4 and conclude with a summary in §5. Details of our tests of numerical fragmentation in disk simulations and calculations of the model scaling between star formation, gas density, and orbital frequency are presented in the Appendices. Throughout, we work in the context of a dark-energy dominated cold dark matter cosmology with a Hubble constant  $H_0 \approx 70 \text{ km s}^{-1} \text{ Mpc}^{-1}$ .

## 2. METHODOLOGY

To examine molecular gas and star formation in disk galaxies, we develop a model that accounts for low temperature coolants ( $T < 10^4 \text{ K}$ ), calculates the equilibrium abundance of  $\text{H}_2$  in dense gas, and estimates the local SFR based on the local  $\text{H}_2$  density with a universal SFE per free fall time. This ISM model is detailed below in §2.1, and is referred to as the  $\text{H}_2\text{D-SF}$  model (for “ $\text{H}_2$  density-star formation”). We extend the  $\text{H}_2\text{D-SF}$  model to account for the destruction of  $\text{H}_2$  by an interstellar radiation field powered by local star formation, and refer to the extended model as the  $\text{H}_2\text{D-SF+ISRF}$  model (for “ $\text{H}_2$  density-star formation plus interstellar radiation field”). The  $\text{H}_2\text{D-SF+ISRF}$  model is also detailed below in §2.1. The new molecular gas ISM and star formation models are contrasted against a simple ISM model that includes only atomic cooling with a temperature floor  $T = 10^4 \text{ K}$  and a SFR calculated from the total gas density above a density threshold, which we refer to as the  $\text{GD-SF}$  model (for “gas density-star formation”). The  $\text{GD-SF}$  model has been commonly used in previous galaxy formation simulations. Each star formation and ISM model is numerically implemented in the smoothed particle hydrodynamics (SPH) / N-body code GADGET2 (Springel et al. 2001; Springel 2005), which is used to perform the simulations presented in this work. General issues of numerical fragmentation in the disk simulations of the kind presented here are described in §2.3, §2.4, and in the Appendix. The ISM models are applied to simulations of the isolated evolution of disk galaxies with a representative range of circular velocities and structural properties. The galaxy models are designed as analogues of the well-studied nearby galaxies DDO154, M33, and NGC 4501, and are detailed in §2.6. The results of the simulations are presented in §3.

### 2.1. ISM Properties

The thermal properties of the ISM are largely determined by the radiative heating  $\mathcal{H}$  and cooling  $\Lambda$  rates of interstellar gas. Given  $\mathcal{H}$  and  $\Lambda$ , the rate of change of the internal energy  $u$  of gas with a density  $\rho_g$  evolves as

$$\rho_g \frac{du}{dt} = \mathcal{H} - \Lambda, \quad (1)$$

with additional terms to describe the energy input from feedback or hydrodynamical interactions. The temperature dependence of  $\mathcal{H}$  and  $\Lambda$  will depend on the metallicity and density of gas, and on the nature of the external radiation field.

To calculate the above heating and cooling processes, as well as additional cooling processes from molecules and ionic species other than  $\text{H}_2$ , we use the photoionization

code Cloudy version C06.02a, last described by Ferland et al. (1998). Cloudy calculates heating and cooling processes for H, He, and metals, as well as absorption by dust grains, photoelectric absorption, and molecular photoabsorption. The chemical network and cooling includes molecules and atomic ions that allow gas to cool to temperatures  $T < 10^4 \text{ K}$ . For details on the molecular network and cooling, the reader is encouraged to examine Hollenbach & McKee (1979, 1989), Ferland et al. (1998), and the Cloudy documentation suite Hazy<sup>4</sup>. For purposes of calculating the efficiency of molecular line cooling using Cloudy, only the thermal line width is considered. At temperatures below our minimum temperature of ( $T \sim 100 \text{ K}$ ), the influence of nonthermal motions on molecular line cooling will become increasingly important and should be considered when modeling lower temperature gas.

For the heating term  $\mathcal{H}$ , our Cloudy calculations include heating from the cosmic ultraviolet background at  $z = 0$  following Haardt & Madau (1996), extended to include the contribution to the UV background from galaxies (see the Cloudy documentation for details). Cosmic ray heating and ionization are incorporated following Ferland & Mushotzky (1984), and are important at densities where the ISM becomes optically thick to UV radiation. The presence of a blackbody cosmic microwave background radiation with a temperature of  $T \approx 2.7 \text{ K}$  is included. Milky Way-like ( $R_V = 3.1$ ) dust, including both graphite and silicate dust, is modeled with the local ISM abundance. Grain heating and cooling mechanisms are included, following van Hoof et al. (2001) and Weingartner & Draine (2001).

The  $\text{H}_2\text{D-SF}$  model of the ISM includes all the cooling and heating processes described above. In addition, the  $\text{H}_2\text{D-SF+ISRF}$  model includes the following treatment of the ISRF, and is used to examine the consequences of soft UV radiation from star formation for the molecular phase of the ISM.

Mathis et al. (1983) modeled the ISRF needed to power the emission spectrum of dust both in the diffuse ISM and in molecular clouds in the Milky Way. The short-wavelength ( $\lambda \lesssim 0.3 \mu\text{m}$ ) ISRF spectral energy distribution (SED) was inferred to scale roughly exponentially with a scale length  $R_u \sim 4 \text{ kpc}$  in the MW disk (for a solar galactocentric radius of  $R_\odot = 10 \text{ kpc}$ ), tracing the stellar population, while the strength of the long-wavelength ISRF SED varied non-trivially with radius owing to the relative importance of emission from dust. The short-wavelength ISRF SED determined by Mathis et al. (1983) (their Table A3) for  $R = 0.5 - 1.3 R_\odot$ , normalized to a fixed stellar surface density, is roughly independent of radius, with a shape similar to the radiation field considered by Draine (1978) and Draine & Bertoldi (1996). For simplicity, we fix the ISRF spectrum to have its inferred SED in the solar vicinity and scale the intensity with the local SFR density normalized by the solar value as

$$U_{\text{isrf}} \equiv \frac{u_\nu}{u_{\nu,\odot}} = \frac{\Sigma_{\text{SFR}}}{\Sigma_{\text{SFR},\odot}} \quad (2)$$

where  $\Sigma_{\text{SFR},\odot} \approx (2-5) \times 10^{-9} M_\odot \text{ yr}^{-1} \text{ pc}^{-2}$  (e.g., Smith et al. 1978; Miller & Scalo 1979; Talbot 1980; Rana 1987, 1991; Kroupa 1995). For our model, we adopt  $\Sigma_{\text{SFR},\odot} = 4 \times 10^{-9} M_\odot \text{ yr}^{-1} \text{ pc}^{-2}$ . When included, the ISRF is added to the input spectrum for the Cloudy calculations as an additional source of radiation.

<sup>4</sup> <http://www.nublado.org>

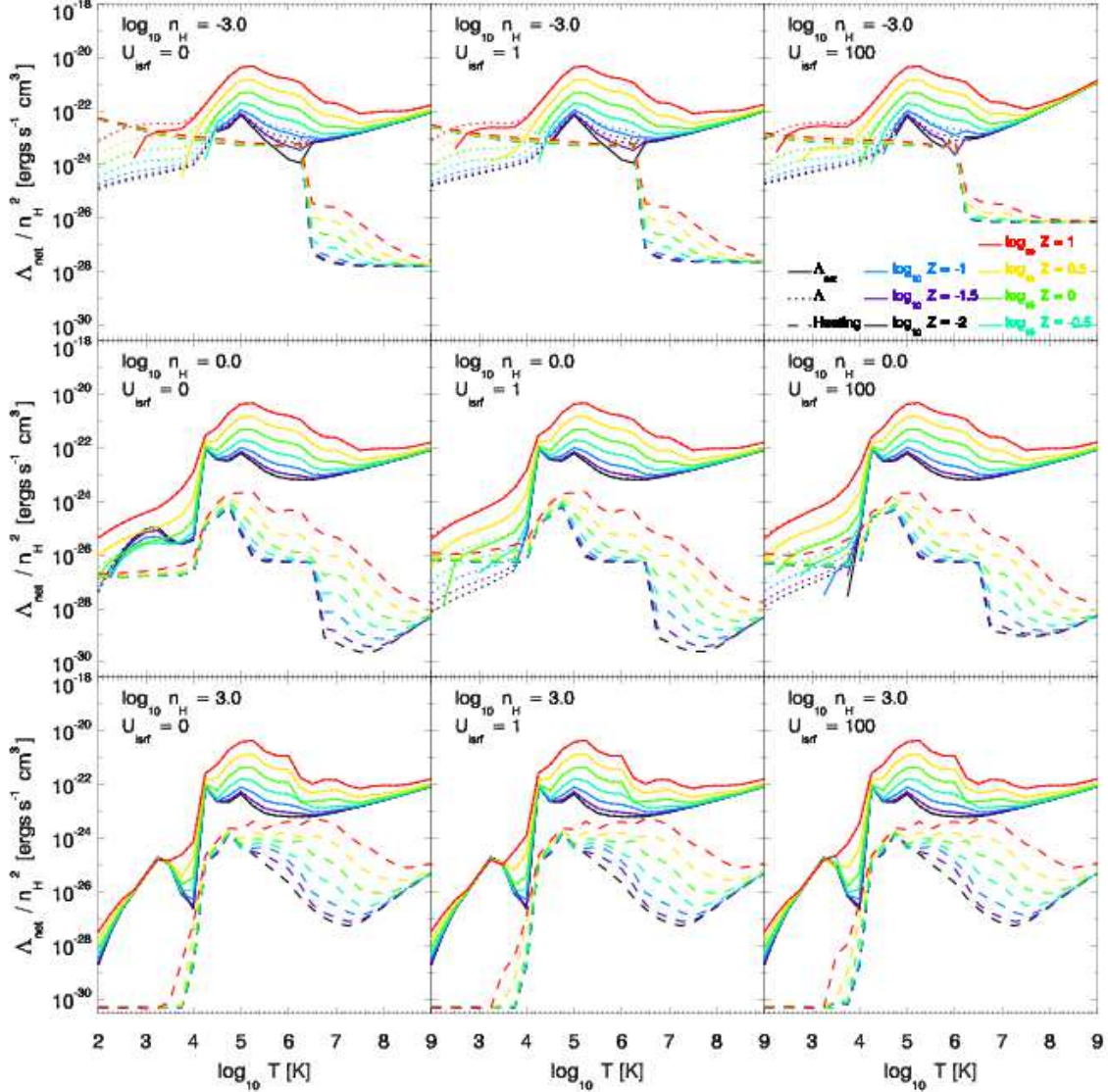


FIG. 1.— Cooling ( $\Lambda$ ) and heating ( $\mathcal{H}$ ) rates for interstellar and intergalactic gas as a function of gas density ( $n_H$ ), temperature ( $T$ ), metallicity ( $Z$ ), and interstellar radiation field (ISRF) strength ( $U_{\text{isrf}}$ ), in units of the ISRF strength in the MW at the solar circle, as calculated by the code Cloudy (Ferland et al. 1998). Shown are the cooling (dotted lines), heating (dashed lines) and net cooling (solid) functions over the temperature range  $T = 10^2 - 10^9$  K. Dense gas can efficiently cool via atomic and molecular coolants below  $T = 10^4$  K, depending on the gas density and the strength of the ISRF. A strong ISRF can enable the destruction of  $\text{H}_2$  gas and thereby reduce the SFR.

Absorption of soft UV ( $\lambda \sim 0.1 \mu\text{m}$ ) photons can enable the destruction of  $\text{H}_2$  through transitions to the vibrational continuum or to excited states that can be photoionized or photodissociated (Stecher & Williams 1967). The ISRF can supply the soft UV photons that lead to  $\text{H}_2$  dissociation and can subsequently regulate the  $\text{H}_2$  abundance at low gas densities ( $n_H \sim 1 \text{cm}^{-3}$ ). For values of  $U_{\text{isrf}} \gtrsim 0.01$ , the ionizing flux of the ISRF dominates over the Haardt & Madau (1996) UV background (see, e.g., Sternberg et al. 2002).

Figure 1 shows the cooling rate  $\Lambda$  (dotted line), the heating rate  $\mathcal{H}$  (dashed line), and net cooling rate  $\Lambda_{\text{net}}$  (solid lines) calculated for a range of temperatures ( $T$ ), densities ( $n_H$ ), metallicities ( $Z$ ), and ISRF strengths ( $U_{\text{isrf}}$ ). For each value of  $T$ ,  $n_H$ ,  $Z$ , and  $U_{\text{isrf}}$  a Cloudy simulation is performed assuming a plane-parallel radiation field illuminating a 10pc thick slab chosen to be comparable to our hydrodynamical spatial resolution. Each simulation is allowed to iterate until convergence, after which the heat-

ing rate, cooling rate, ionization fraction, molecular fraction, electron density, and molecular weight is recorded from the center of the slab. These quantities are tabulated on a grid over the range  $\log_{10} T = \{2, 9\} \log_{10} \text{K}$  with  $\Delta \log_{10} T = 0.25$ ,  $\log_{10} n_H = \{-6, 6\} \log_{10} \text{cm}^{-3}$  with  $\Delta \log_{10} n_H = 1.5$ ,  $\log_{10} Z = \{-2, 1\} \log_{10} Z_{\odot}$  with  $\Delta \log_{10} Z = 1.5$ , and  $U_{\text{isrf}} = \{0, 1, 10, 100, 1000\} U_{\text{isrf}, \odot}$ , and log-linearly interpolated according to the local gas properties. We note that since the slab thickness determines the typical particle column density for a given volume density, the tabulated quantities can depend on the slab thickness. For reference, varying the slab thickness between 100pc and 1pc for a density of  $n_H \sim 30 \text{cm}^{-3}$  changes the molecular fraction by less than 30% and the heating and cooling rates by less than 50%.

The left panels of Figure 1 with  $U_{\text{isrf}} = 0$  correspond to net cooling functions used in the  $\text{H}_2\text{D-SF}$  model, while the  $\text{H}_2\text{D-SF+ISRF}$  model includes all the net cooling functions presented in the figure. The GD-SF model that includes only

atomic cooling incorporates the regions of the net cooling functions in the left ( $U_{\text{isrf}} = 0$ ) panels of Figure 1 at temperatures  $T > 10^4 \text{K}$ . In addition to well known cooling and heating processes operating at high temperatures ( $T > 10^4 \text{K}$ ), the results of the Cloudy simulations show that cooling of gas near  $n_{\text{H}} \sim 1 \text{cm}^{-3}$  is regulated by the presence of the ISRF (Figure 1, middle left and center panels) and an ISRF strength of  $U_{\text{isrf}} \sim 1$  contributes a low-temperature heating rate  $\mathcal{H}$  more than an order of magnitude larger than that supplied by the cosmic UV background. At higher densities ( $n_{\text{H}} \sim 10^3 \text{cm}^{-3}$ ), the gas remains optically-thin to cosmic ray heating but becomes insensitive to the presence of either the ISRF or the cosmic UV background. The correlation between the ISRF field strength and the local SFR limits the applicability of the low- $n_{\text{H}}$  / high- $U_{\text{isrf}}$  region of the cooling function but we include such regimes for completeness.

The simple description of the ISRF used in our modeling is designed to replicate average conditions in systems like the Milky Way. However, the ISRF in special locations in the ISM, such as near photoionized regions, may have a different character than the average SED we employ. Also, changes in the composition of dust or the initial mass function of stars relative to Milky Way properties could alter the frequency-dependent ISRF. We therefore caution that the detailed, frequency-dependent connection between SFR and ISRF strength used in our modeling does not capture every condition within the ISM of a single galaxy or between galaxies. The model we present does realistically capture the physics that regulate the abundance of molecular hydrogen and local SFR for a given spectral form of the ISRF.

## 2.2. Star Formation and Feedback

Modeling the SFR in the ISM as a power-law function of the gas density  $\rho_g$  dates to at least Schmidt (1959), who modeled the past SFR of the Galaxy needed to produce the observed luminosity function of main sequence stars. We assume that star formation occurs in molecular clouds in proportion to the local molecular gas density  $f_{\text{H}_2} \rho_g$ , as suggested by a variety of observations (e.g., Elmegreen & Lada 1977; Blitz & Thaddeus 1980; Beichman et al. 1986; Lada 1987; Young & Scoville 1991). The model thus assumes that  $\text{H}_2$  is a good proxy for star forming gas.

On the scale of individual gas particles the SFR is then determined by the density of molecular hydrogen, which is converted into stars on a time scale  $t_*$ :  $\rho_* \propto f_{\text{H}_2} \rho_g / t_*$ . Observations indicate that at high densities  $t_*$  scales with the local free fall time of the gas,  $t_{\text{ff}} \propto \rho_g^{-0.5}$ , as

$$t_* \approx t_{\text{ff}} / \epsilon_{\text{ff}}, \quad (3)$$

with the SFE per free fall time,  $\epsilon_{\text{ff}} \approx 0.02$ , approximately independent of density at  $n \approx 10^2 - 10^4 \text{cm}^{-3}$  (Krumholz & McKee 2005; Krumholz & Tan 2007).

We adopt  $t_* = 1 \text{Gyr}$  for gas at density  $n_{\text{H}} = 10^3 \text{cm}^{-3}$  ( $t_{\text{ff}} = 2.33 \times 10^7 \text{yrs}$ ), which corresponds to  $\epsilon_{\text{ff}} = 0.023$ . By calibrating the SFE to observations of dense molecular clouds through  $\epsilon_{\text{ff}}$ , our model differs from the usual approach of choosing gas consumption time scale to fit the global SFR and the SK relation in galaxies. As we show below, the chosen efficiency results in global SFR for the entire galaxies consistent with observations (see §3).

Incorporating the assumption that a mass fraction  $\beta$  of young stars promptly explode as supernovae, the SFR in our

models is given by

$$\dot{\rho}_* = (1 - \beta) f_{\text{H}_2} \frac{\rho_g}{t_*} \left( \frac{n_{\text{H}}}{10^3 \text{cm}^{-3}} \right)^{0.5}. \quad (4)$$

We assume  $\beta \approx 0.1$ , appropriate for the Salpeter (1955) initial mass function. Implicit in Equation 4 is that the molecular fraction  $f_{\text{H}_2}$  may vary with a variety of local ISM properties as

$$f_{\text{H}_2} = f_{\text{H}_2}(\rho_g, T, Z_g, U_{\text{isrf}}). \quad (5)$$

The  $\text{H}_2\text{D-SF}$  model includes the dependence on the gas density, temperature  $T$ , metallicity  $Z_g$ . The  $\text{H}_2\text{D-SF+ISRF}$  model additionally includes the dependence of the molecular fraction on the strength of the interstellar radiation field  $U_{\text{isrf}}$  parameterized as a fraction of the local interstellar field energy density. In both the  $\text{H}_2\text{D-SF}$  and  $\text{H}_2\text{D-SF+ISRF}$  models, the equilibrium molecular fraction is tabulated by using the Cloudy calculations discussed in §2.1. Variations in the cosmic ray ionization rate or the dust model could affect the form of Equation 5 but we do not consider them here. For the simple GD-SF model that does not track the molecular gas abundance, we set  $f_{\text{H}_2} = 1$  in gas with densities above the star formation threshold density  $n_{\text{H}} \gtrsim 0.1 \text{cm}^{-3}$  (see, e.g., Governato et al. 2007).

Figure 1 shows that the feature in the cooling rate at  $T \sim 10^3 \text{K}$  for low metallicity, intermediate density gas (e.g., middle left panel), which owes to molecular hydrogen, disappears in the presence of the interstellar radiation field. Equations 1 and 4 then imply that destruction of  $\text{H}_2$  by soft UV photons from young stars regulates star formation in the  $\text{H}_2\text{D-SF+ISRF}$  model. The dissociation of  $\text{H}_2$  by the ISRF means that ISM gas may be cold and dense but its SFR may be suppressed if the local ISRF is strong. We discuss this effect in the context of the simulated galaxy models in §3.

The energy deposition from supernovae into interstellar gas is treated as a thermal feedback, given by

$$\rho_g \frac{du}{dt} = \epsilon_{\text{SN}} \dot{\rho}_* \quad (6)$$

where  $\epsilon_{\text{SN}}$  is the energy per unit mass of formed stars that is deposited into the nearby ISM. We choose  $\epsilon = 1.4 \times 10^{49} \text{ergs } M_{\odot}^{-1}$  or, in the language of Springel & Hernquist (2003b), an effective supernovae temperature of  $T_{\text{SN}} = 3 \times 10^8$ . This value for the energy deposition for supernovae has been used repeatedly in simulations of galaxy mergers (e.g., Robertson et al. 2006a,b,c). Given that extremely short cooling time of dense gas at low resolutions, prescribing supernovae feedback as thermal input into the gas has long been known to have a weak effect on the global evolution of simulated galaxies (e.g., Katz 1992; Steinmetz & Müller 1995). For this reason, the results of this paper also do not depend strongly on the value of  $\epsilon_{\text{SN}}$  or the supernovae mass fraction  $\beta$ . Metal enrichment of the ISM is treated in the instantaneous approximation, with a mass fraction  $y = 0.02$  of the supernovae ejecta being returned into the gas as metals (see Springel & Hernquist 2003a).

## 2.3. Avoiding Numerical Jeans Fragmentation

Perturbations in a self-gravitating medium of mean density  $\rho$  and sound speed  $c_s$  can grow only if their wavelength exceeds the Jeans length  $\lambda_{\text{Jeans}}$  (Jeans 1928). The corresponding Jeans mass contained within  $\lambda_{\text{Jeans}}$  is

$$m_{\text{Jeans}} = \frac{\pi^{5/2} c_s^3}{6G^{3/2} \rho^{1/2}} \quad (7)$$

(see, e.g., §5.1.3 of Binney & Tremaine 1987). Bate & Burkert (1997) identified a resolution requirement for smoothed particle hydrodynamics simulations such that the number of SPH neighbors  $N_{\text{neigh}}$  and gas particle mass  $m_{\text{gas}}$  should satisfy  $2N_{\text{neigh}}m_{\text{gas}} < m_{\text{Jeans}}$  to capture the pressure forces on the Jeans scale and avoid numerical fragmentation. Klein et al. (2004) suggest that the effective resolution of SPH simulations is the number of SPH smoothing lengths per Jeans scale

$$h_{\text{Jeans}} = \frac{\pi^{5/2} c_s^3}{6G^{3/2} N_{\text{neigh}} m_{\text{gas}} \rho^{1/2}}, \quad (8)$$

which is very similar to the number of Jeans masses per SPH kernel mass, if we define the kernel mass as

$$m_{\text{SPH}} \equiv \sum_{i=1}^{N_{\text{neigh}}} m_i. \quad (9)$$

Our simulations include low temperature coolants that allow ISM gas to become cold and dense, and for the typical number of gas particles used in our models ( $N_{\text{gas}} \approx 400,000$ ) the Jeans mass is not resolved at the lowest temperatures and largest galaxy masses. Motivated by techniques used to avoid numerical Jeans fragmentation in grid codes (e.g., Machacek et al. 2001), a density-dependent pressure floor is introduced into our SPH calculations. For every gas particle, the kernel mass is monitored to ensure it resolves some number  $N_{\text{Jeans}}$  of Jeans masses. If not, the particle internal energy is altered following

$$u = u \times \begin{cases} \left(\frac{N_{\text{Jeans}}}{h_{\text{Jeans}}}\right)^{2/3} & : h_{\text{Jeans}} < N_{\text{Jeans}} \\ \left(\frac{2N_{\text{Jeans}}m_{\text{SPH}}}{m_{\text{Jeans}}}\right)^{2/3} & : m_{\text{Jeans}} < 2N_{\text{Jeans}}m_{\text{SPH}} \end{cases}, \quad (10)$$

to provide the largest local pressure and to assure the local Jeans mass is resolved. We discuss the purpose and effect of this pressurization in more detail in the first Appendix, but we note that this requirement scales with the resolution and naturally allows for better-resolved SPH simulations to follow increasingly lower temperature gas. For the simulations results presented in this paper, we use  $N_{\text{Jeans}} = 15$ , which is larger than the effective  $N_{\text{Jeans}} = 1$  used by Bate & Burkert (1997). We have experimented with simulations with  $N_{\text{Jeans}} = 1 - 100$  and find  $N_{\text{Jeans}} \sim 15$  to provide sufficient stability over the time evolution of the simulations for the structure of galaxy models we use. Other simulations may require different values  $N_{\text{Jeans}}$  or a different pressurization than the  $u \propto m_{\text{Jeans}}^{-2/3}$  scaling suggested by Equation 7.

#### 2.4. Median Equation-of-State

In the absence of a numerical pressure floor, the equation-of-state (EOS) of gas will follow the loci where heating balances cooling in the temperature-density phase space. However, the gas pressurization requirements to avoid numerical Jeans fragmentation change the EOS of the gas. For purposes of calculating the molecular or ionization fraction of dense ISM gas that has been numerically pressurized, an estimate of the EOS in the absence of resolution restraints is required. Figure 2 shows the temperature-density phase diagram of ISM gas in a simulation of a Milky Way-sized galaxy without using the SPH pressure floor described in §2.3 and detailed in the Appendix.

The median EOS of this gas, determined by the heating and cooling processes calculated by the Cloudy code for a

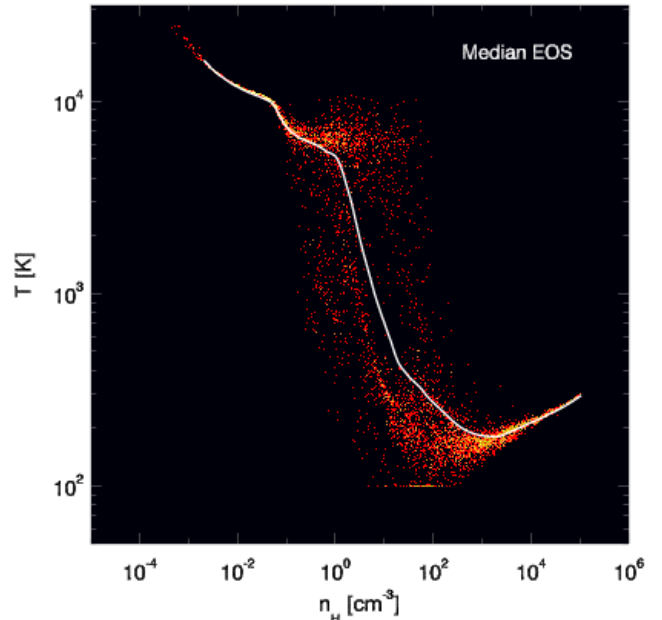


FIG. 2.— Median equation-of-state (EOS) of gas in a Milky Way-sized galactic disk in our ISM model. Shown is the histogram of particles in the hydrogen number density  $n_{\text{H}}$  – temperature  $T$  plane and the median temperature measured in bins of density (white line). The median EOS is used to determine the properties of gas pressurized to avoid numerical Jeans fragmentation (see §2.3 and §2.4). At high densities, the particles follow the loci where heating balances cooling for their densities, temperatures, metallicities, and local interstellar radiation field strengths.

given density, temperature, metallicity, and interstellar radiation field strength, as well as heating from supernovae feedback, is used in our simulations to assign an effective temperature to dense gas pressurized at the Jeans resolution limit. The behavior of gas above a density of  $n_{\text{H}} \sim 100 \text{cm}^{-3}$  is especially influenced by the balance of available cooling mechanisms and supernovae heating, and in the absence of supernovae feedback such dense gas would cool to the minimum temperature treated in our simulations ( $T \sim 100\text{K}$ ).

#### 2.5. Molecular Fraction vs. Gas Density

The molecular content of the ISM in models that account for the abundance of  $\text{H}_2$  and other molecular gas depends on the physical properties of interstellar gas through Equation 5. Since the temperature and density phase structure of the ISM is dictated by the local cooling time, which is nonlinearly dependent on the temperature, density, metallicity, and ISRF strength, the calculation of the equilibrium molecular fraction as a function of the gas properties is efficiently calculated using hydrodynamical simulations of galaxy evolution. We have measured the molecular gas fraction  $f_{\text{H}_2}$  as a function of gas density  $n_{\text{H}}$  after evolving in ISM models with  $\text{H}_2$ -destruction by an ISRF (the  $\text{H}_2\text{D-SF+ISRF}$  model), and without an ISRF (the  $\text{H}_2\text{D-SF}$  model), for  $t = 0.3\text{Gyr}$  for each of the  $v_{\text{circ}} = 50 - 300 \text{km s}^{-1}$  disk galaxy simulations. The galaxy-to-galaxy and point-to-point variations in the metallicity, temperature, ISRF strength contribute to the spread in molecular fractions at a given density  $n_{\text{H}}$ . Without  $\text{H}_2$ -destruction, the molecular hydrogen content of low-density gas calculated using Cloudy is surprisingly large, with  $f_{\text{H}_2} = 0.1$  at  $n_{\text{H}} = 0.1 \text{cm}^{-3}$  and  $f_{\text{H}_2} \sim 0.35$  at  $n_{\text{H}} = 1 \text{cm}^{-3}$ . For the  $\text{H}_2\text{D-SF}$  model, the atomic-to-molecular transition repre-

sents a physical calculation of the star formation threshold density prescription often included in coarse models of star formation in simulations of galaxy formation and evolution.

For the H<sub>2</sub>D-SF+ISRF model, the destruction of H<sub>2</sub> by the ISRF reduces the molecular fraction in the low-density ( $n_{\text{H}} \lesssim 1\text{cm}^{-3}$ ) ISM to  $f_{\text{H}_2} < 0.05$ . The abundance of H<sub>2</sub> in this model is therefore greatly reduced relative to the H<sub>2</sub>D-SF model that does not include an ISRF. The decline in molecular abundance, in turn, produces much lower SFRs in low density gas ( $n_{\text{H}} \lesssim 1\text{cm}^{-3}$ ) compared with either the H<sub>2</sub>D-SF model (which has a larger molecular fraction at low densities) or the GD-SF model (which allows for star formation in all gas above a density threshold,  $n_{\text{H}} > 0.1\text{cm}^{-3}$ ).

For denser gas in the H<sub>2</sub>D-SF+ISRF model (e.g.,  $n_{\text{H}} \gtrsim 1\text{cm}^{-3}$ ), the numerical pressurization of the ISM required to mitigate artificial Jeans fragmentation prevents much of the gas from reaching high densities where the molecular fraction becomes large ( $f_{\text{H}_2} \sim 1$  at  $n_{\text{H}} \gtrsim 100\text{cm}^{-3}$ ). The molecular fraction of the numerically-pressurized gas must be assigned at densities that exceed resolution limit of the simulations. As Figure 2 indicates, the transition between the warm phase at densities  $n_{\text{H}} \lesssim 1\text{cm}^{-3}$  and the cold phase at densities  $n_{\text{H}} \gtrsim 30\text{cm}^{-3}$  is rapid (see also Wolfire et al. 2003). The required pressure floor can artificially limit the density of gas to the range  $n_{\text{H}} \lesssim 30\text{cm}^{-3}$  where, in the presence of an ISRF, the molecular fraction of the gas would be artificially suppressed (without an ISRF, even gas at  $n_{\text{H}} \approx 1\text{cm}^{-3}$  is already mostly molecular and would be relatively unaffected). To account for this numerical limitation, gas at densities  $n_{\text{H}} > 1\text{cm}^{-3}$  that is numerically-pressurized to resolve the Jeans scale is assigned a minimum molecular fraction according to the median EOS and the high-density ( $n_{\text{H}} > 30\text{cm}^{-3}$ )  $f_{\text{H}_2} - n_{\text{H}}$  trend of gas in the absence of the pressure floor. The  $f_{\text{H}_2} - n_{\text{H}}$  relation calculated by Cloudy can be modeled for pressurized gas in this regime as  $f_{\text{H}_2} = \max\{[0.67(\log_{10} n_{\text{H}} + 1.5) - 1], 1\}$ .

The utilization of the median EOS to assign detailed properties to the dense gas in this manner has the further benefit of adaptively scaling with the local resolution, allowing an approximation of the ISM properties that improves with an increase in the particle number used in a simulation. Throughout the paper, when simulation results include gas particles that are pressurized to avoid numerical Jeans fragmentation, their reported temperatures and molecular fractions are determined from the median EOS presented in Figure 2.

While the density dependence of molecular fraction utilized here may not be correct in every detail (i.e., the transition to  $f_{\text{H}_2} = 1$  may occur at an inaccurately low density), for our purposes the primary requirement is that the model captures the fraction of star forming gas as a function of density in a realistic fashion. The gas mass in disks in the H<sub>2</sub>D-SF+ISRF model at  $\Sigma_{\text{gas}} \gtrsim 10M_{\odot}\text{pc}^{-2}$  is mostly molecular and the molecular fraction increases realistically with the external ISM pressure (see §3.3), in good agreement with observations (e.g., Wong & Blitz 2002; Blitz & Rosolowsky 2006).

## 2.6. Isolated Galaxy Models

We use three cosmologically-motivated galaxy models to study global star formation relations. Below we describe the models and list the observational data used to motivate their adopted structure.

The galaxy initial conditions follow the methodology described by Springel et al. (2005), with a few exceptions. The properties of the disks are chosen to be representative of disk galaxies that form within the CDM structure formation

paradigm (e.g., Mo et al. 1998). The model galaxies consist of a Hernquist (1990) dark matter halo, exponential stellar and gaseous disks with scale lengths  $R_{\text{d},*}$  and  $R_{\text{d},\text{g}}$ , and an optional Hernquist (1990) stellar bulge with scale radius  $a_{\text{b},*}$ . For a given virial mass, the Hernquist (1990) dark matter halo parameters are scaled to an effective Navarro et al. (1996) halo concentration. The velocity distributions of the dark matter halos are initialized from the isotropic distribution function provided in Hernquist (1990), using the rejection technique described by Press et al. (1992). The vertical distribution of the stellar disk is modeled with a  $\text{sech}^2(z/2z_{\text{d}})$  function with  $z_{\text{d}} = 0.2 - 0.3R_{\text{d},*}$ . The stellar disk velocity field is initialized by using a Gaussian with the local velocity dispersion  $\sigma_z^2$  determined from the potential and density via the Jeans equations. The stellar disk rotational velocity dispersion and streaming velocity are set with the epicyclic approximation (see §3.2.3 and §4.2.1(c) of Binney & Tremaine 1987). The bulge velocity field is also modeled by a Gaussian with a velocity dispersion determined from the Jeans equations but with no net rotation. The gas disk is initialized as an isothermal medium of temperature of  $T = 10^4\text{K}$  in hydrostatic equilibrium with the total potential, including the disk self-gravity, which determines vertical distribution of the gas self-consistently (see Springel et al. 2005). The gravitational softening lengths for the dark matter and baryons are set to  $\epsilon_{\text{DM}} = 100h^{-1}\text{pc}$  and  $\epsilon_{\text{baryon}} = 50h^{-1}\text{pc}$ , respectively.

The galaxy models are designed to roughly match the observed rotation curves, and HI, H<sub>2</sub>, and stellar surface mass distributions of DDO154 ( $v_{\text{circ}} \approx 50\text{km s}^{-1}$ ), M33 ( $v_{\text{circ}} \approx 125\text{km s}^{-1}$ ), and NGC4501 ( $v_{\text{circ}} \approx 300\text{km s}^{-1}$ ). These systems cover a wide range in circular velocity, gas fractions, disk scale lengths, molecular gas fractions, gas surface densities, and gas volume densities. The parameters of the galaxy models are provided in Table 1.

### 2.6.1. DDO 154 Analogue

DDO 154 is one of the most gas rich systems known and therefore provides unique challenges to models of the ISM in galaxies. For the DDO 154 galaxy analogue, we used the Carignan & Beaulieu (1989) HI map and rotation curves as the primary constraint on the mass distribution. The total gas mass is  $M_{\text{d},\text{g}} \approx 2.7 \times 10^8 h^{-1} M_{\odot}$  (Carignan & Beaulieu 1989; Hunter & Elmegreen 2004). The stellar disk mass has been estimated at  $M_{\text{d},*} \approx 3.4 \times 10^6 h^{-1} M_{\odot}$  (Lee et al. 2006) with a scale length of about  $R_{\text{d},*} \approx 0.38h^{-1}\text{kpc}$  at  $\lambda = 3.6\mu\text{m}$ . The gaseous disk scale length was determined by approximating the HI surface density profile, with  $R_{\text{d},\text{g}} \approx 1.52^{-1}\text{kpc}$  providing a decent mimic of the HI data. These numbers are similar to those compiled by McGaugh (2005) for DDO 154 and, combined with the dark matter virial velocity  $V_{200} = 50\text{km s}^{-1}$  and concentration  $c = 6$ , produce a rotational velocity of  $v_{\text{circ}} \approx 50\text{km s}^{-1}$  (where  $v_{\text{circ}}$  is defined as the maximum of rotation velocity profile) similar to the value of  $v_{\text{circ}} \approx 54\text{km s}^{-1}$  reported by Karachentsev et al. (2004).

### 2.6.2. M33 Analogue

The nearby spiral M33 has well measured stellar, HI, H<sub>2</sub>, and SFR distributions, and serves nicely as an example disk galaxy with an intermediate rotational velocity. For the M33 galaxy analogue, we used the Heyer et al. (2004) HI and H<sub>2</sub> map as guidance for determining the gas distribution with a total gas mass of  $M_{\text{d},\text{g}} \approx 1.68 \times 10^9 h^{-1} M_{\odot}$  (Corbelli 2003; Heyer et al. 2004). According to this data, the gas disk scale

TABLE 1  
 GALAXY MODELS

Galaxy Analogue	$V_{200}$ km s <sup>-1</sup>	$v_{\text{circ}}$ km s <sup>-1</sup>	$c$	Structural Parameters						
				$M_{\text{disk}}$ $h^{-1}M_{\odot}$	$f_{\text{gas}}$	$R_{\text{d},*}$ $h^{-1}\text{kpc}$	$R_{\text{d,g}}$ $h^{-1}\text{kpc}$	$M_{\text{bulge}}$ $h^{-1}M_{\odot}$	$a_{\text{b},*}$ $h^{-1}\text{kpc}$	
DDO 154	50	50	6	$2.91 \times 10^8$	0.99	0.38	1.52	...	...	
M33	100	125	10	$4.28 \times 10^9$	0.40	0.98	2.94	...	...	
NGC 4501	180	300	14	$1.02 \times 10^{11}$	0.04	3.09	2.16	$1.14 \times 10^{10}$	0.62	
Numerical Parameters										
Galaxy Analogue	$N_{\text{DM}}$	$N_{\text{d},*}$	$N_{\text{d,g}}$	$N_{\text{bulge}}$	$\epsilon_{\text{DM}}$ $h^{-1}\text{kpc}$	$\epsilon_{\text{baryon}}$ $h^{-1}\text{kpc}$	$N_{\text{neigh}}$	$N_{\text{neigh}}m_{\text{gas}}$ $h^{-1}M_{\odot}$	Data Refs.	
DDO 154	120000	20000	400000	...	0.1	0.05	64	$4.60 \times 10^4$	1,2,3,4,5	
M33	120000	120000	400000	...	0.1	0.05	64	$2.74 \times 10^5$	5,6,7	
NGC 4501	120000	177600	400000	22400	0.1	0.05	64	$6.51 \times 10^5$	8,9,10,11,12	

REFERENCES. — (1) Carignan & Beaulieu (1989); (2) Hunter & Elmegreen (2004); (3) Hunter et al. (2006); (4) Lee et al. (2006); (5) McGaugh (2005); (6) Corbelli (2003); (7) Heyer et al. (2004); (8) Wong & Blitz (2002); (9) Möllenhoff & Heidt (2001) (10) Guhathakurta et al. (1988); (11) Rubin et al. (1999); (12) Boissier et al. (2003)

length is roughly  $R_{\text{d,g}} \approx 2.7h^{-1}\text{kpc}$ . We set the total stellar disk mass to  $M_{\text{d},*} \approx 2.6 \times 10^9 h^{-1}M_{\odot}$  to match the total baryonic mass of  $M_{\text{baryon}} \approx 4.3 \times 10^9 h^{-1}M_{\odot}$  reported by McGaugh (2005), and set the disk scale length to  $R_{\text{d},*} \approx 0.9h^{-1}\text{kpc}$ . These numbers are similar to those compiled by McGaugh (2005) for M33 and, combined with the dark matter virial velocity  $V_{200} = 100\text{ km s}^{-1}$  and concentration  $c = 10$ , produce a rotational velocity of  $v_{\text{circ}} \approx 125\text{ km s}^{-1}$ .

### 2.6.3. NGC 4501 Analogue

The massive spiral NGC 4501 is a very luminous disk galaxy ( $M_K = -25.38$ , Möllenhoff & Heidt 2001) that is gas poor by roughly a factor of  $\sim 3$  for its stellar mass (Giovanelli & Haynes 1983; Kenney & Young 1989; Blitz & Rosolowsky 2006), and serves as an extreme contrast to the dwarf galaxy DDO 154. To construct an analogue to NGC 4501, we used the rotation curve data compiled by Boissier et al. (2003) from the observations of Guhathakurta et al. (1988) and Rubin et al. (1999) as a guide for designing the potential. The stellar disk scale length  $R_{\text{d},*} \approx 3.1h^{-1}\text{kpc}$  and bulge-to-disk ratio  $M_{\text{bulge}}/M_{\text{disk}} = 0.112$  were taken from the  $K$ -band observations of Möllenhoff & Heidt (2001), and the total stellar mass was chosen to be consistent with the Bell & de Jong (2001)  $K$ -band Tully-Fisher relation. The gas distribution was modeled after the surface mass density profile presented by Wong & Blitz (2002). These structure properties, combined with a virial velocity  $V_{200} = 180\text{ km s}^{-1}$  and dark matter concentration  $c = 14$ , provide a circular velocity of  $v_{\text{circ}} \approx 300\text{ km s}^{-1}$  appropriate for approximating the observed rotation curve.

## 3. RESULTS

The isolated evolution of each of the three disk galaxy models is simulated for  $t = 1.0\text{ Gyr}$  using the three separate ISM and star formation models described in §2: the model H<sub>2</sub>D-SF with H<sub>2</sub>-based star formation, the model H<sub>2</sub>D-SF+ISRF which in addition includes the gas heating by local interstellar radiation, and the GD-SF model with a  $T = 10^4\text{ K}$  temperature floor and constant threshold density for star formation. In all cases, the ISM of galaxies is assumed to have initial metallicity of  $10^{-2}Z_{\odot}$  and is self-consistently enriched by supernovae during the course of simulation.

### 3.1. Galactic Structure and Evolution

The gas distributions in the simulated disk galaxies after  $t = 0.3\text{ Gyr}$  of evolution in isolation are shown in Figure 3. The image intensity reflects the disk surface density while the color indicates the local mass-weighted temperature of the ISM. A variety of structural properties of the galaxies are evident from the images, including ISM morphologies qualitatively similar to those observed in real galaxies. The large-scale structure of each disk model changes slowly over gigayear time-scales, excepting only the H<sub>2</sub>D-SF model for the  $v_{\text{circ}} = 50\text{ km s}^{-1}$  galaxy. In this case, the ISM fragments owing to the large cold gas reservoir that becomes almost fully molecular in the absence of H<sub>2</sub>-destruction (see §3.2.1 and §3.2.2 for further discussion).

The simulated disks can develop spiral structure and bar-like instabilities during their evolution, especially when modeled with  $T < 10^4\text{ K}$  coolants. The detailed structures of the spiral patterns and bar instabilities are likely influenced by numerical fluctuations in the potential, but they illustrate the role of spiral structure in the ISM of real galaxies. As the ISM density is larger in these structures, the equilibrium gas temperature is lower compared with the average disk properties. These structures also contain higher molecular fractions (see §3.3) and will be sites of enhanced star formation in our ISM model, similar to real galaxies.

The small-mass systems evolved with the GD-SF model are more diffuse and have less pronounced structure than those evolved with low-temperature coolants, owing to the higher ( $T > 10^4\text{ K}$ ) ISM temperature (and hence pressure) in high-density regions. The diffuse morphologies of low-mass galaxies in the GD-SF and H<sub>2</sub>D-SF+ISRF models owe to the abundance of warm atomic gas with thermal energy comparable to the binding energy of the gas. The tendency of low-mass galaxy disks to be more diffuse and extended than more massive systems owing to inefficient cooling was shown by Kravtsov et al. (2004) and Tassis et al. (2008) to successfully reproduce the faint end of the luminosity function of galactic satellites and scaling relations of dwarf galaxies. Kaufmann et al. (2007) used hydrodynamical simulations of the dissipative formation of disks to demonstrate that the temperature floor of  $T = 10^4\text{ K}$  results in the equilibrium disk scale height-to-scale length ratio in systems with  $v_{\text{circ}} \sim 40\text{ km s}^{-1}$  to be roughly three times larger than for galaxies with  $v_{\text{circ}} \sim 80\text{ km s}^{-1}$ . The disk morphologies in our GD-SF runs are qualitatively consistent with their results.



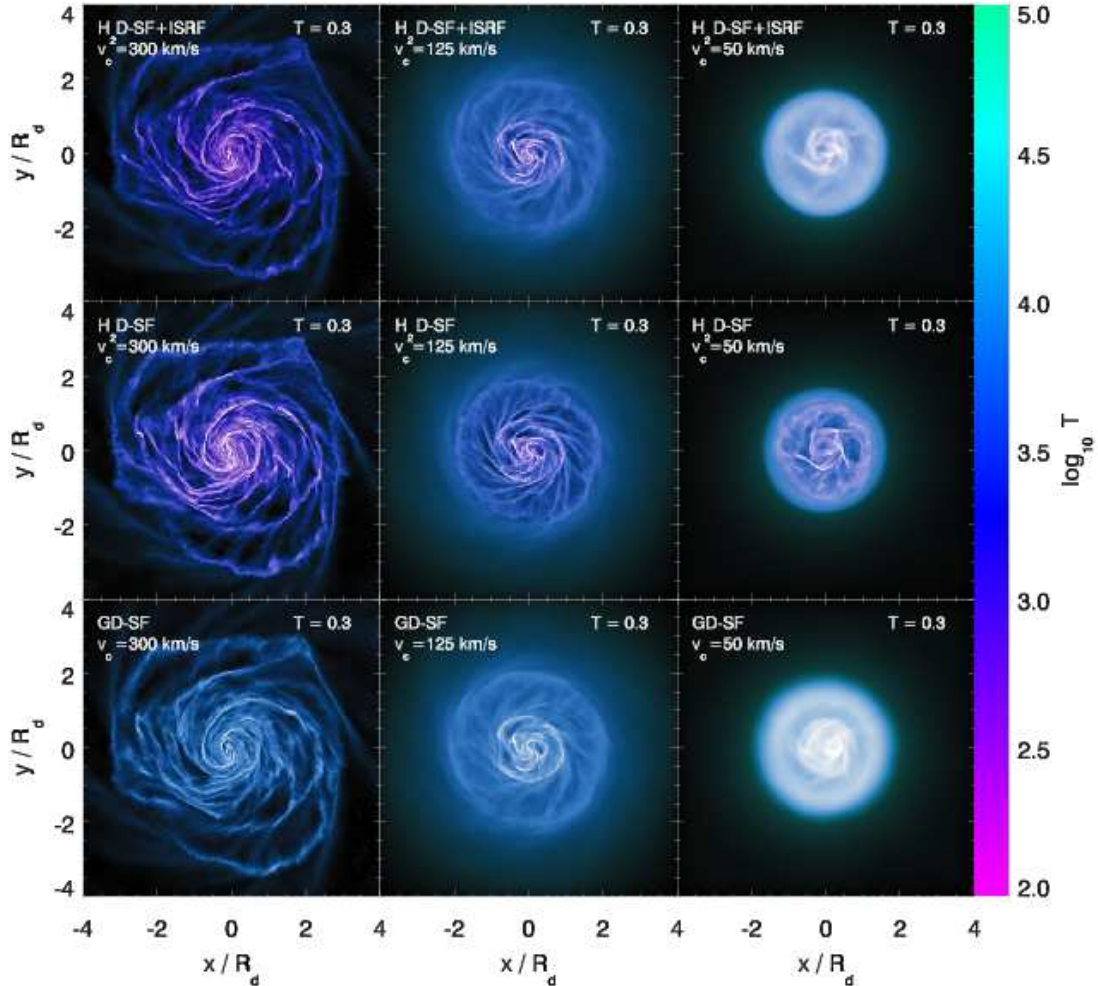


FIG. 3.— Gas distribution in galaxies with circular velocities of  $v_{\text{circ}} = 300 \text{ km s}^{-1}$  (left column),  $v_{\text{circ}} = 125 \text{ km s}^{-1}$  (middle column), and  $v_{\text{circ}} = 50 \text{ km s}^{-1}$  (right column) for differing models of the ISM and star formation. Shown are an atomic cooling model with a  $T = 10^4 \text{ K}$  temperature floor and star formation based on the gas density above a threshold of  $n_{\text{H}} = 0.1 \text{ cm}^{-3}$  ("GD-SF", bottom row), an atomic+molecular cooling model with a  $T = 10^2 \text{ K}$  temperature floor and star formation based on the molecular gas density ("H<sub>2</sub>D-SF", middle row), and an atomic+molecular cooling model with a  $T = 10^2 \text{ K}$  temperature floor, star formation based on the molecular gas density, and H<sub>2</sub>-destruction by an interstellar radiation field ("H<sub>2</sub>D-SF+ISRF", top row). The intensity of the images reflects the gas surface density and is color-coded by the local effective gas temperature. The diffuse morphologies of low-mass galaxies in the GD-SF and H<sub>2</sub>D-SF+ISRF models owe to the abundance of warm atomic gas with temperatures comparable to the velocity scale of the local potential.

### 3.1.1. Molecular Fraction vs. Disk Radius

The variations in the molecular fraction  $f_{\text{H}_2}$  as a function of the gas volume density  $n_{\text{H}}$  discussed in §2.5 map into  $f_{\text{H}_2}$  gradients with surface density or disk radius on the global scale of a galaxy model. Figure 4 shows azimuthally-averaged molecular fraction  $f_{\text{H}_2}$  as a function of radius normalized to the disk scale length in the simulated disk galaxies with  $v_{\text{circ}} = 50 - 300 \text{ km s}^{-1}$  for molecular ISM models H<sub>2</sub>D-SF+ISRF and H<sub>2</sub>D-SF, after  $t = 0.3 \text{ Gyr}$  of evolution. The average molecular fraction decreases with decreasing rotational velocity, from  $f_{\text{H}_2} > 0.6$  within a disk scale length for the  $v_{\text{circ}} = 300 \text{ km s}^{-1}$  system (left panel) to  $f_{\text{H}_2} < 0.4$  within a disk scale length for the  $v_{\text{circ}} = 50 \text{ km s}^{-1}$  system (right column) in the H<sub>2</sub>D-SF+ISRF model. The radial dependence of the molecular fraction steepens in smaller mass galaxies relative to the  $v_{\text{circ}} = 300 \text{ km s}^{-1}$  model since a larger fraction of gas has densities below the atomic-to-molecular transition. The impact of this trend on the global star formation relation is discussed below in §3.2.1. We note that details of the

model initial conditions can influence the radial distribution of the molecular gas by changing the typical gas density in the disk. In particular, the  $v_{\text{circ}} = 125 \text{ km s}^{-1}$  model galaxy has a more centrally concentrated molecular gas distribution than does M33.

Figure 4 clearly shows that the ISRF in the H<sub>2</sub>D-SF+ISRF model steepens the dependence of molecular fraction  $f_{\text{H}_2}$  on the radius  $R$  for each galaxy compared with the H<sub>2</sub>D-SF model.

### 3.1.2. Star Formation Histories

The star formation histories of the simulated galaxies provide a summary of the efficiency of gas consumption for systems with different disk structures and models for ISM physics. Figure 5 shows the SFR over the time interval  $t = 0 - 1 \text{ Gyr}$  for the isolated galaxy models evolved with the GD-SF, H<sub>2</sub>D-SF, and H<sub>2</sub>D-SF+ISRF models. In most simulations, the SFR experiences a general decline as the gas is slowly converted into stars. Substantial increases in the SFR with time are driven either by the formation of bar-like structures

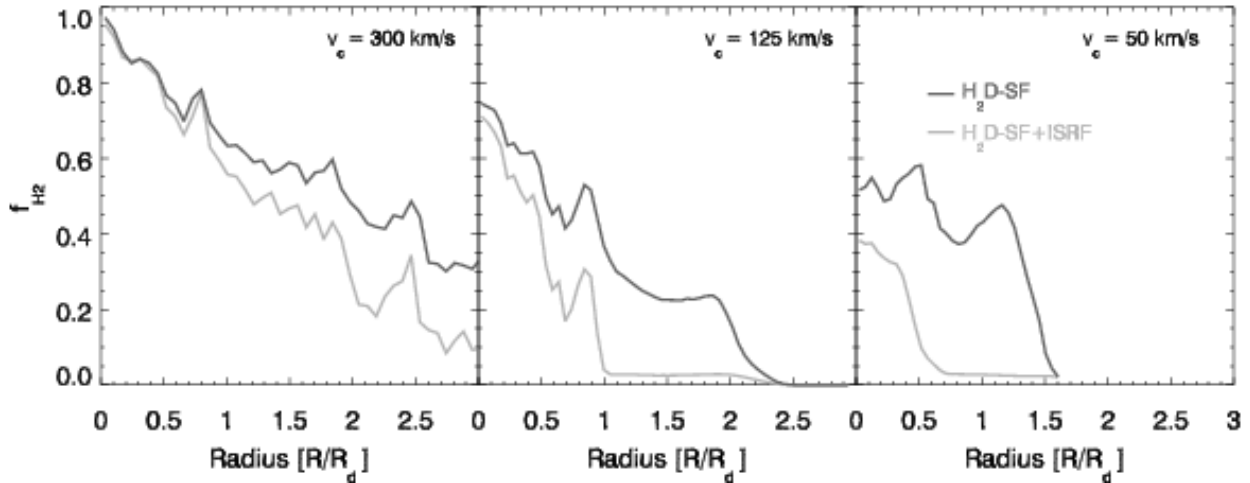


FIG. 4.— Molecular fraction as a function of radius in three simulated disk galaxies with ISM models with (light gray lines) and without (dark gray lines) an interstellar radiation field. The general trend is for molecular fraction to decrease and its dependence on radius to steepen with decreasing mass of the system. This trend is more pronounced in the model with an interstellar radiation field.

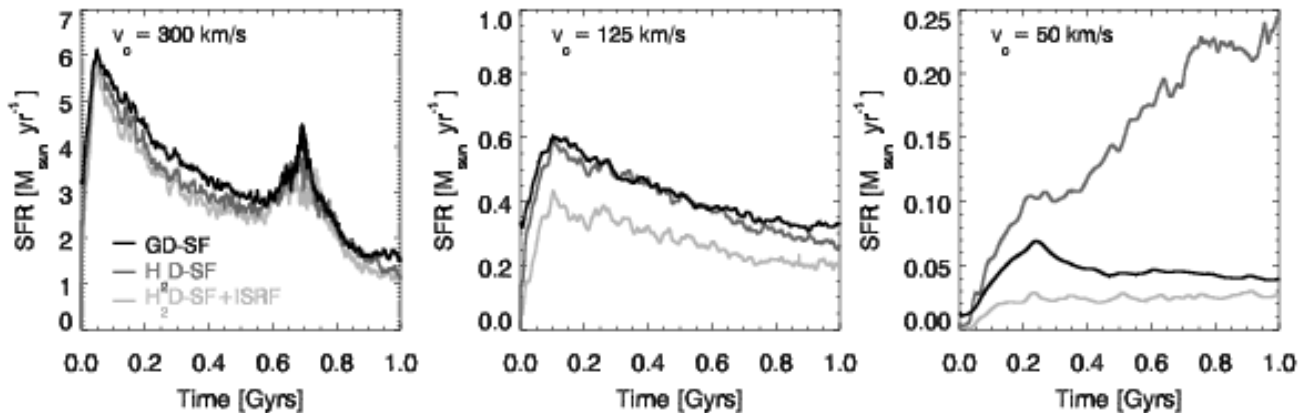


FIG. 5.— Star formation rates (SFRs) as a function of time in isolated disks. Shown are the SFRs for galaxy models with  $v_{\text{circ}} = 50 \text{ km s}^{-1}$  (right panel),  $v_{\text{circ}} = 125 \text{ km s}^{-1}$  (middle panel), and  $v_{\text{circ}} = 300 \text{ km s}^{-1}$  (left panel) calculated from interstellar medium models that allow for cooling at temperatures  $T > 10^4 \text{ K}$  (black lines) or cooling at temperatures  $T > 10^2 \text{ K}$  with (light gray lines) and without (dark gray lines) destruction of  $\text{H}_2$  by a local interstellar radiation field (ISRF). The star formation efficiency of the low-mass systems is strongly influenced by  $\text{H}_2$ -destruction from the ISRF.

(e.g., after  $t \approx 0.7 \text{ Gyr}$  for the  $v_{\text{circ}} = 300 \text{ km s}^{-1}$  galaxy) or, in one case, fragmentation of the cold ISM (after  $t \approx 0.4 \text{ Gyr}$  for the  $v_{\text{circ}} = 50 \text{ km s}^{-1}$  galaxy evolved with the  $\text{H}_2\text{D-SF}$  model).

For the most massive galaxy, differences in the relative star formation efficiencies of models that tie the SFR to the total gas density (the GD-SF model) or to the molecular gas density (the  $\text{H}_2\text{D-SF}$  and  $\text{H}_2\text{D-SF+ISRF}$  models) are not large. The ISM in the massive galaxy is dense, and when  $\text{H}_2$  abundance is modeled much of the gas becomes molecular (see Figure 4). When  $\text{H}_2$ -destruction is included the molecular content of the ISM in this galaxy is reduced at large radii and small surface densities, but much of the mass of the ISM (e.g., interior to a disk scale length) retains a molecular fraction comparable to the ISM model without  $\text{H}_2$ -destruction. The effect of the ISRF on the SFR of this galaxy is fairly small.

The SFR history of the intermediate-mass ( $v_{\text{circ}} = 125 \text{ km s}^{-1}$ ) galaxy model is more strongly influenced by the  $\text{H}_2$ -destroying ISRF. While the GD-SF and  $\text{H}_2\text{D-SF}$  ISM models produce similar star formation efficiencies, reflecting the substantial molecular fraction in the ISM for the  $\text{H}_2\text{D-SF}$  model, the effects of  $\text{H}_2$ -destruction in the  $\text{H}_2\text{D-SF+ISRF}$  model reduce the SFR by  $\sim 30\text{--}40\%$ . The time derivative of the SFR in the  $\text{H}_2\text{D-SF+ISRF}$  model is also shallower than for

the GD-SF or  $\text{H}_2\text{D-SF}$  models, reflecting a reservoir of non-star-forming gas. In each model, the SFR of the whole system is similar to that estimated for M33 ( $\text{SFR} \sim 0.25\text{--}0.7 M_{\odot} \text{ yr}^{-1}$ , Kennicutt 1998; Hippelein et al. 2003; Blitz & Rosolowsky 2006; Gardan et al. 2007).

The effects of  $\text{H}_2$ -destruction play a crucial role in determining the star formation history of the  $v_{\text{circ}} = 50 \text{ km s}^{-1}$  dwarf system. The single phase ISM (GD-SF) model produces a SFR history qualitatively similar to the more massive galaxies, but in the  $\text{H}_2\text{D-SF}$  model the star formation history changes dramatically. The colder ISM temperature allows the gaseous disk to become substantially thinner in this case compared to the GD-SF model, leading to higher densities and SFRs. After  $t \approx 0.4 \text{ Gyr}$  of evolution, the cold, dense gas in the  $\text{H}_2\text{D-SF}$  model allows the ISM in the dwarf to undergo large-scale instabilities and, quickly thereafter, fragmentation. The dense knots of gas rapidly increase their SFE compared with the more diffuse ISM of the GD-SF model and the SFR increases to a rate comparable to that calculated for the  $v_{\text{circ}} = 125 \text{ km s}^{-1}$  model. In the  $\text{H}_2\text{D-SF+ISRF}$  model, the equilibrium temperature of most diffuse (and metal poor) gas in the dwarf is increased and the vertical structure of the disk becomes thicker than in the  $\text{H}_2\text{D-SF}$  model. The molec-

ular content of the disk is thus substantially reduced (see the right panel of Figure 4) and the disk remains diffuse. As a result, the SFR drops to a low and roughly constant level. The constancy of the SFR in the H<sub>2</sub>D-SF+ISRF model is a result of the large gas reservoir that remains atomic and is therefore unavailable for star formation. As the molecular gas, which comprises a small fraction of the total ISM in the dwarf ( $f_{\text{H}_2} \lesssim 0.1$  by mass), is gradually consumed it is continually refueled by the neutral gas reservoir.

The star formation history of the dwarf galaxy system in the H<sub>2</sub>D-SF+ISRF model demonstrates that physics other than energetic supernova feedback can regulate star formation and produce long gas consumption time scales in dwarf galaxies. Star formation rates in real galaxies similar to the  $v_{\text{circ}} = 50 \text{ km s}^{-1}$  model fall in the wide range  $\text{SFR} \sim 10^{-4} - 0.1 M_{\odot} \text{ yr}^{-1}$  (e.g., Hunter & Elmegreen 2004). While the H<sub>2</sub>D-SF+ISRF simulation of the dwarf galaxy produces a steady  $\text{SFR} \sim 0.025 M_{\odot} \text{ yr}^{-1}$ , we note that the galaxy DDO 154 that served as a model for the  $v_{\text{circ}} = 50 \text{ km s}^{-1}$  system has a star formation rate of only  $\text{SFR} \sim 0.004 M_{\odot} \text{ yr}^{-1}$  (Hunter & Elmegreen 2004).

### 3.2. Star Formation Relations in Galactic Disks

The disk-averaged SK relation in galaxies, determined by Kennicutt (1998), is well described by the power-law

$$\Sigma_{\text{SFR}} = (2.5 \pm 0.7) \times 10^{-4} \times \left( \frac{\Sigma_{\text{gas}}}{1 M_{\odot} \text{ pc}^{-2}} \right)^{1.4 \pm 0.15} M_{\odot} \text{ yr}^{-1} \text{ kpc}^{-2}. \quad (11)$$

However, as discussed in the Introduction, spatially-dependent determinations of the total gas SK relation slope vary in the range  $n_{\text{tot}} = 1.7 - 3.55$ . While the slope of the spatially-resolved molecular gas SK relation is consistently measured to be  $n_{\text{mol}} \approx 1.4$  in the same systems, with a two-sigma variation of  $n_{\text{mol}} \sim 1.2 - 1.7$  (Wong & Blitz 2002; Boissier et al. 2003; Heyer et al. 2004; Boissier et al. 2007; Kennicutt et al. 2007). Below, we examine SK relations in the simulated disks and compare our results directly with these observations.

#### 3.2.1. The Total Gas Schmidt-Kennicutt Relation

A dichotomy between the total gas and molecular gas SK relations is currently suggested by the data and should be a feature of models of the ISM and star formation. Figure 6 shows the simulated total gas SK relation that compares the SFR surface density  $\Sigma_{\text{SFR}}$  to the total gas surface density  $\Sigma_{\text{gas}}$  for different galaxy models. The quantities  $\Sigma_{\text{SFR}}$  and  $\Sigma_{\text{gas}}$  are azimuthally-averaged in annuli of width  $\Delta r = 150 h^{-1} \text{ pc}$  for the  $v_{\text{circ}} = 300 \text{ km s}^{-1}$  and  $v_{\text{circ}} = 125 \text{ km s}^{-1}$  systems and  $\Delta r = 75 h^{-1} \text{ pc}$  for the smaller  $v_{\text{circ}} = 50 \text{ km s}^{-1}$  disk. Regions within the radius enclosing 95% of the gas disk mass are shown. The SK relation is measured in each disk at times  $t = 0.3 \text{ Gyr}$  and  $t = 1.0 \text{ Gyr}$  to monitor its long-term evolution. Power-law fits to the SFR density as a function of the total gas surface mass densities in the range  $\Sigma_{\text{gas}} = 5 - 100 M_{\odot} \text{ pc}^{-2}$  measured at  $t = 0.3 \text{ Gyr}$  are indicated in each panel, with the range chosen to approximate regimes that are currently observationally accessible. The simulated relations between  $\Sigma_{\text{SFR}}$  and  $\Sigma_{\text{gas}}$  are not strict power-laws, and different choices for the range of surface densities or simulation time of the fit may slightly change the inferred power-law index, with lower surface densities typically leading to larger indices and, similarly,

later simulation times probing lower surface densities and correspondingly steeper indices. Exceptions are noted where appropriate, but the conclusions of this paper are not strongly sensitive to the fitting method of the presented power-law fits. Disk-averaged SFR and surface mass densities are also measured and plotted for comparison with the non-starburst galaxies of Kennicutt (1998).

Each row of panels in Figure 6 shows results for the three galaxy models evolved with different models for the ISM and star formation. For the traditional GD-SF model, the  $\Sigma_{\text{SFR}} - \Sigma_{\text{gas}}$  correlation in massive, thin-disk systems tracks the input relation for this model,  $\dot{\rho}_{\star} \propto \rho_g^{1.5}$ , at intermediate surface densities. At low surface densities, massive disks deviate from the  $\Sigma_{\text{SFR}} \propto \Sigma_{\text{gas}}^{1.5}$  relation as the imposed density threshold is increasingly probed in the disk interior and disk flaring begins to steepen the relation between the volume density  $\rho_g$  and the gas surface density  $\Sigma_{\text{gas}}$ . In lower mass galaxies, the disks are thicker at a given gas surface density, as dictated by hydrostatic equilibrium (e.g., Kaufmann et al. 2007), with a correspondingly lower average three-dimensional density. The SK relation therefore steepens somewhat between galaxies with  $v_{\text{circ}} = 300 \text{ km s}^{-1}$  and  $v_{\text{circ}} = 125 \text{ km s}^{-1}$  in this star formation model, but does not fully capture the mass-dependence of the SK relation apparent in the observations.

The middle row of Figure 6 shows the total gas SK relation measured in disks evolved with the H<sub>2</sub>D-SF model, which are generally similar to the more prescriptive GD-SF model in terms of the relation slope. The arbitrary density threshold for star formation included in the GD-SF model roughly mimics the physics of the atomic-to-molecular gas transition calculated by Cloudy for the H<sub>2</sub>D-SF model, as molecular transition begins at densities of  $n_{\text{H}} \sim 0.1 \text{ cm}^{-3}$  when the effects of H<sub>2</sub>-destruction by an ISRF are *not* included.

Note that the H<sub>2</sub>D-SF model allows gas to cool to considerably lower temperatures than in the atomic cooling-only GD-SF model. This allows the ISM gas in the  $v_{\text{circ}} = 50 \text{ km s}^{-1}$  galaxy to become cold enough to settle into a thin, dense disk and reach high molecular fractions. Indeed, the increase in the molecular content of the disk contributes to the increase in the SFE in the dwarf galaxy at  $t = 1 \text{ Gyr}$  during its evolution seen in the middle right panel of Figure 6. However, observed  $v_{\text{circ}} \approx 50 \text{ km s}^{-1}$  galaxies have *very low* molecular fractions and the high molecular content of the dwarf at  $t = 1 \text{ Gyr}$  is a potential deficit of the H<sub>2</sub>D-SF model.

The bottom row of Figure 6 shows the SK relation for the most complete "H<sub>2</sub>D-SF+ISRF" model. In this model, the SK relation power-law index increases systematically from  $n_{\text{tot}} = 2.2$  for the  $v_{\text{circ}} = 300 \text{ km s}^{-1}$  galaxy to  $n_{\text{tot}} = 4.3$  for the  $v_{\text{circ}} = 50 \text{ km s}^{-1}$  dwarf. The decreased abundance of H<sub>2</sub> at low densities has steepened the SK relation at low gas surface densities compared with either the GD-SF or H<sub>2</sub>D-SF models. The ISM in the dwarf galaxy is prevented from becoming fully molecular and maintains an extremely steep SK relation over its evolution from  $t = 0.3 \text{ Gyr}$  to  $t = 1 \text{ Gyr}$ . Consequently, the global SFR of the model dwarf galaxy in this case stays low and approximately constant. The global gas consumption time scale is also much longer than in the other two models.

While the disk-averaged SK relation determination for the galaxies have the lowest SFE in the H<sub>2</sub>D-SF+ISRF model, the values are still consistent with the observational determinations by Kennicutt (1998), Wong & Blitz (2002), Boissier et al. (2003), and Boissier et al. (2007).

#### 3.2.2. The Molecular Gas Schmidt-Kennicutt Relation

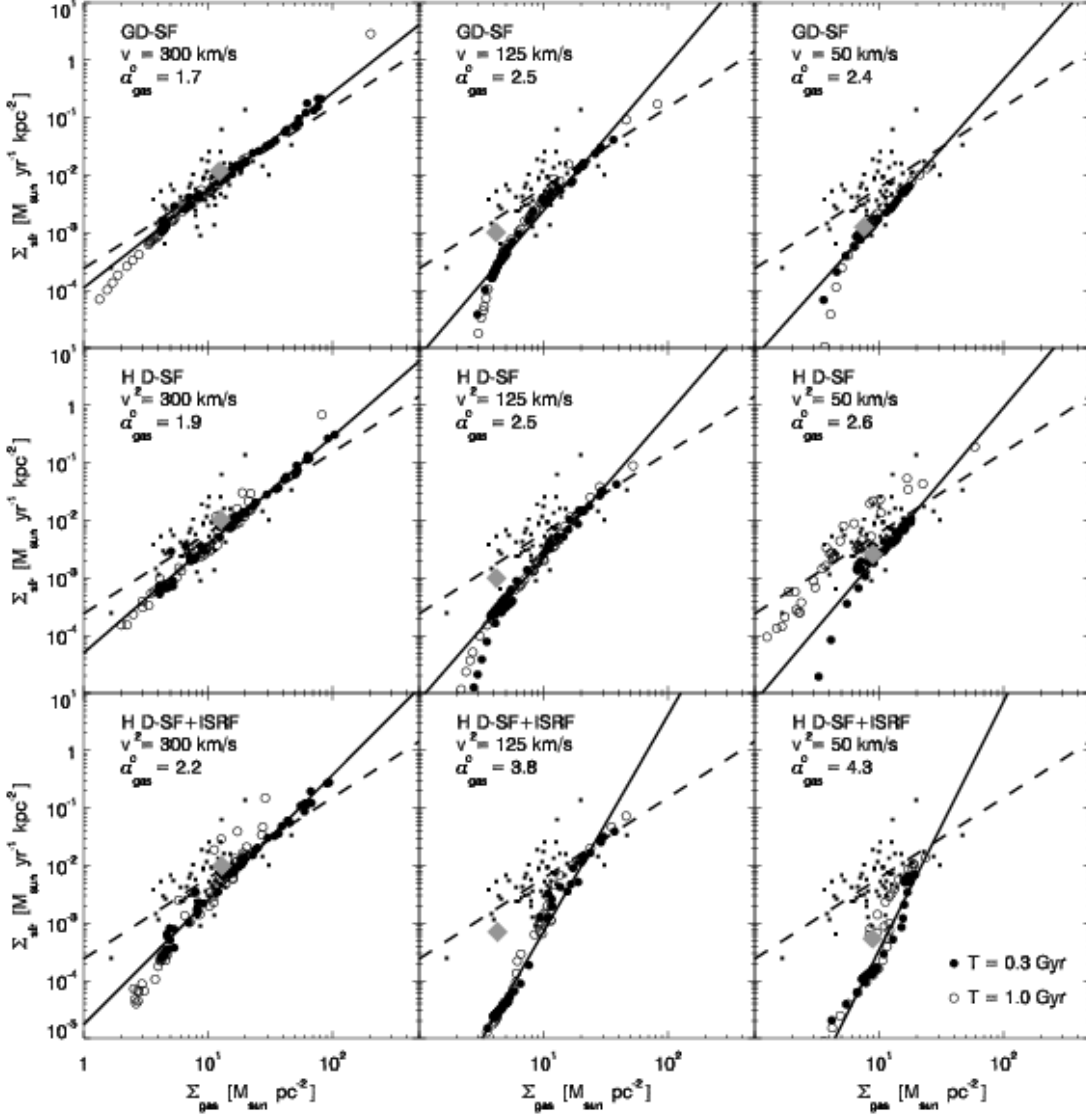


FIG. 6.— Schmidt-Kennicutt relation for total gas surface densities. Shown is the SFR surface density  $\Sigma_{\text{SFR}}$  as a function of the total gas surface density  $\Sigma_{\text{gas}}$  for galaxy models with circular velocities of  $v_{\text{circ}} = 50 \text{ km s}^{-1}$  (right column),  $v_{\text{circ}} = 125 \text{ km s}^{-1}$  (middle column), and  $v_{\text{circ}} = 300 \text{ km s}^{-1}$  (left column) for ISM models that include atomic coolants (upper row), atomic+molecular coolants with (lower row) and without (middle row)  $\text{H}_2$ -destruction from a local interstellar radiation field. The surface densities  $\Sigma_{\text{SFR}}$  and  $\Sigma_{\text{gas}}$  are measured in annuli from the simulated disks after evolving for  $t = 0.3 \text{ Gyr}$  (solid circles) and  $t = 1 \text{ Gyr}$  (open circles) in isolation. The disk-averaged data from Kennicutt (1998) is shown for comparison (small dots). The best power-law fits to the individual galaxies have indices in the range  $\alpha \approx 1.7 - 4.3$  (solid lines). Deviations from the  $\Sigma_{\text{SFR}} \propto \Sigma_{\text{gas}}^{1.5}$  relation are caused by the radial variation in the molecular gas fraction  $f_{\text{H}_2}$ , the scale height of star-forming gas  $h_{\text{SFR}}$ , and the scale height of the total gas distribution  $h_{\text{gas}}$ . The total disk averaged surface densities (grey diamonds) are consistent with the Kennicutt (1998) normalization for normal, massive star-forming galaxies (dashed lines).

As discussed in §3.2, the two-sigma range in observational estimates of the molecular gas SK relation power-law index is  $n_{\text{mol}} \approx 1.2 - 1.7$ , and is smaller than the variation in the slope of the  $\Sigma_{\text{SFR}} - \Sigma_{\text{gas}}$  relation. Figure 7 shows the molecular gas SK relation measured in galaxies evolved with the two molecular ISM models considered in this paper. The SFR and molecular gas surface densities are measured from the simulations as described in §3.2.1 and the reported power-law indices were fit to molecular gas surface densities in the range  $\Sigma_{\text{H}_2} = 0.1 - 100 M_{\odot} \text{ pc}^{-2}$ . Note that the correlation of the SFR surface density with the  $\text{H}_2$  surface density is not an entirely trivial consequence of our  $\text{H}_2$ -based implementation of star formation, as we implement our star formation model on the scale of individual gas particles in three dimensions

and the observational correlations we consider are azimuthal surface density averages in annuli. The two are not equivalent, as we discuss below in the next subsection (see also Schaye & Dalla Vecchia 2008).

The disk-averaged SFR and molecular gas surface densities in the  $\text{H}_2\text{D-SF}$  model are consistent with observations of the molecular gas SK relation by Kennicutt (1998). The molecular gas SK relation power-law index of this model is similar for galaxies of different mass  $n_{\text{mol}} = 1.4 - 1.5$ . Unlike the  $\Sigma_{\text{SFR}} - \Sigma_{\text{gas}}$  relation, the molecular gas SK relation is well-described by a power-law over a wide range in surface densities in the  $\text{H}_2\text{D-SF}$  model. As discussed previously, the low-mass dwarf galaxy experiences an increase in the SFE at a fixed surface density during the evolutionary period be-

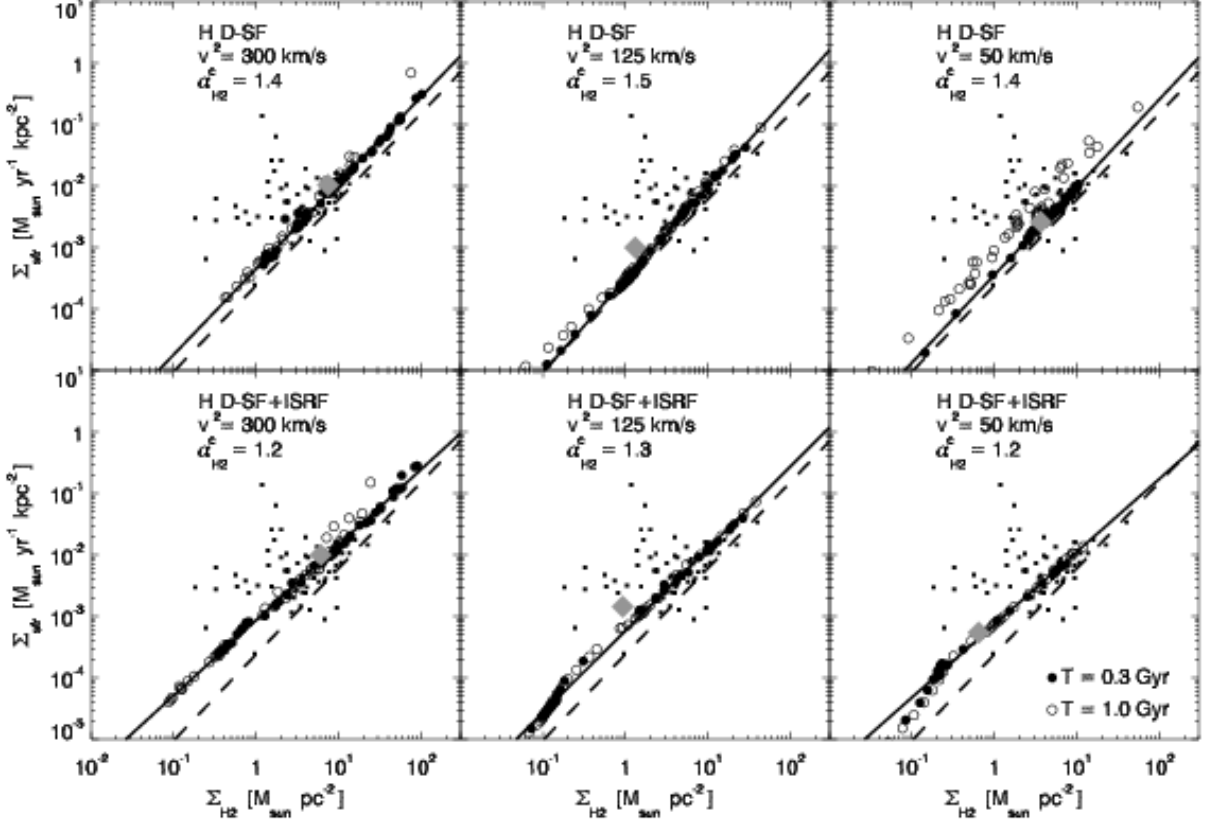


FIG. 7.— Schmidt-Kennicutt relation for molecular gas surface densities. Shown is the star formation rate surface density  $\Sigma_{\text{SFR}}$  as a function of the molecular gas surface density  $\Sigma_{\text{H}_2}$  for galaxy models with circular velocities of  $v_{\text{circ}} = 50 \text{ km s}^{-1}$  (right panels),  $v_{\text{circ}} = 125 \text{ km s}^{-1}$  (middle panels), and  $v_{\text{circ}} = 300 \text{ km s}^{-1}$  (left panels) and ISM models that include atomic+molecular coolants with (lower panels) and without (upper panels)  $\text{H}_2$ -destruction from a local interstellar radiation field. The surface densities  $\Sigma_{\text{SFR}}$  and  $\Sigma_{\text{H}_2}$  are measured in annuli (dark circles) from the simulated disks after evolving for  $t = 0.3 \text{ Gyr}$  and  $t = 1 \text{ Gyr}$  (open circles) in isolation. The disk-averaged data from Kennicutt (1998) is shown for comparison (small dots). The best power-law fits to the individual galaxies have indices in the range  $\alpha \approx 1.2\text{--}1.5$  (solid lines). The total disk averaged surface densities (grey diamonds) are consistent with the Kennicutt (1998) relation for normal, massive star-forming galaxies (dashed lines).

tween  $t = 0.3 \text{ Gyr}$  and  $t = 1.0 \text{ Gyr}$  owing to a nearly complete conversion of its ISM to molecular gas in the  $\text{H}_2\text{D-SF}$  model.

Panels in the bottom row of Figure 7 show that the addition of a local interstellar radiation field in the  $\text{H}_2\text{D-SF+ISRF}$  model controls the amplitude of the  $\Sigma_{\text{SFR}} - \Sigma_{\text{H}_2}$  relation, but does not strongly affect its slope. The normalization and power-law index of the molecular gas SK relation in this model are quite stable with time, reflecting how the equilibrium temperature and molecular fractions of the ISM in the  $\text{H}_2\text{D-SF+ISRF}$  are maintained between simulation times  $t = 0.3 \text{ Gyr}$  and  $t = 1.0 \text{ Gyr}$ . Only the most massive galaxy experiences noticeable steepening of the  $\Sigma_{\text{SFR}} - \Sigma_{\text{H}_2}$  correlation at high surface densities. The disk-averaged observations of the molecular gas SK relation by Kennicutt (1998) are well-matched by the simulations and remain approximately constant over their duration.

While the scale height of the cold, dense gas in the disks is typically comparable to our gravitational softening, the slope of the molecular gas SK relation appears to be insensitive to modest changes in the simulation resolution. Additional resimulations of the calculations presented here with an increased resolution of  $N_{\text{d,g}} = 1.2 \times 10^6$  gas particles show that the slope of the molecular gas SK relation changes by less than 5%.

### 3.2.3. Structural Schmidt-Kennicutt Relation

While the observational total and molecular gas SK relations are well-reproduced by the simulated galaxy models, lo-

cal deviations from a power-law  $\Sigma_{\text{SFR}} - \Sigma_{\text{gas}}$  or  $\Sigma_{\text{SFR}} - \Sigma_{\text{H}_2}$  correlation are abundant. Although these deviations are physical, exhibited by real galaxies, and are well-understood within the context of the simulations, a question remains as to whether a relation that trivially connects the SFR density  $\Sigma_{\text{SFR}}$  and the properties of the disks exists.

The primary relation between the local star formation rate and the gas properties in 3D in the simulations are encapsulated by Equation 4, which relates the three-dimensional SFR density to the molecular gas density. We can relate the three-dimensional properties in the ISM to surface densities through the characteristic scale heights of the disks. The SFR surface density is related to an average local SFR volume density  $\langle \dot{\rho}_* \rangle$  through the scale height of star-forming gas  $h_{\text{SFR}}$  as

$$\Sigma_{\text{SFR}} \propto \langle \dot{\rho}_* \rangle h_{\text{SFR}} \quad (12)$$

Here, the averaging of the three-dimensional density is understood to operate over the region of the disk where the two-dimensional surface density is measured. Similarly, the gas surface and volume densities are related by the proportionality

$$\Sigma_{\text{gas}} \propto \langle \rho_g \rangle h_g. \quad (13)$$

If Equation 4 is averaged over the scale on which  $\Sigma_{\text{SFR}}$  is measured as

$$\langle \dot{\rho}_* \rangle \propto \langle f_{\text{H}_2} \rangle \langle \rho_g \rangle^{1.5}, \quad (14)$$

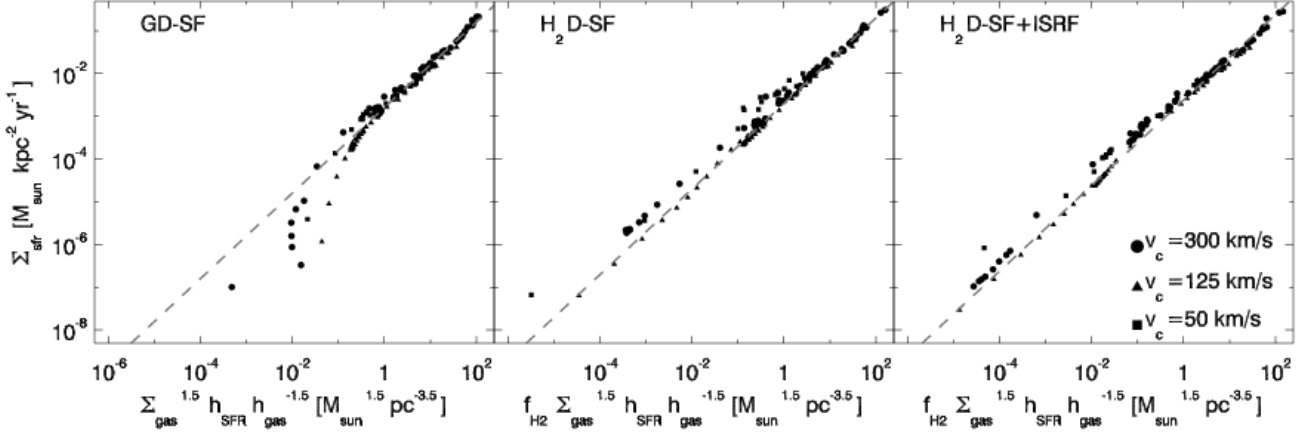


FIG. 8.— A predicted star formation correlation for disk galaxies. The star formation rate (SFR) density in the simulations is calculated as  $\dot{\rho}_* = f_{\text{H}_2} \rho_g / t_*$   $\propto f_{\text{H}_2} (\rho_g) \rho_g^{1.5}$ , where  $f_{\text{H}_2}$  is the molecular fraction,  $\rho_g$  is the gas density, and  $t_*$  is a star formation time-scale that varies with the local gas dynamical time. The local SFR surface density should scale as  $\Sigma_{\text{SFR}} \propto \dot{\rho}_* h_{\text{SFR}}$ , where  $h_{\text{SFR}}$  is the scale height of star-forming gas. Similarly,  $\Sigma_{\text{gas}} \propto \rho_g h_{\text{gas}}$ , where  $h_{\text{gas}}$  is the total gas scale height. The simulations predict that the SFR density in disks should correlate with the gas surface density as  $\Sigma_{\text{SFR}} \propto f_{\text{H}_2} h_{\text{SFR}} h_{\text{gas}}^{-1.5} \Sigma_{\text{gas}}^{1.5}$  (dashed lines).

then the proportionalities can be combined to give

$$\Sigma_{\text{SFR}} \propto \langle f_{\text{H}_2} \rangle \frac{h_{\text{SFR}}}{h_{\text{g}}^{1.5}} \Sigma_{\text{gas}}^{1.5}. \quad (15)$$

Equation 15 can be interpreted as a SK-like correlation, which depends *both* on the molecular gas abundance and the structure of the disk.

Figure 8 shows this expected structural SK relation for the simulated disk galaxies. The star formation, and surface densities are azimuthally-averaged in annuli, as before, and limited to regions of the disk where star formation is active. The characteristic gas scale height  $h_{\text{gas}}$  is determined as a mass-weighted average of the absolute value of vertical displacement for the annular gas distributions. The characteristic star-forming gas scale height  $h_{\text{SFR}}$  is determined in a similar manner, but for gas that satisfies the condition for star formation: namely,  $f_{\text{H}_2} > 0$  for the H<sub>2</sub>D-SF and H<sub>2</sub>D-SF+ISRF models or  $n_{\text{H}} > 0.1 \text{ cm}^{-3}$  for the GD-SF model. Measurements from the simulations are presented after evolving the systems for  $t = 0.3 \text{ Gyr}$  with the GD-SF, H<sub>2</sub>D-SF, and H<sub>2</sub>D-SF+ISRF ISM models. In each case, as expected,  $\Sigma_{\text{SFR}}$  in the disks linearly correlates with quantity  $f_{\text{H}_2} h_{\text{SFR}} h_{\text{gas}}^{-1.5} \Sigma_{\text{gas}}^{1.5}$ .

This relation shows explicitly that the behavior of the  $\Sigma_{\text{SFR}} - \Sigma_{\text{gas}}$  relation can be understood in terms of the dependence of  $f_{\text{H}_2}$  and  $h_{\text{gas}}$  on  $\Sigma_{\text{gas}}$ . For example, the SK relation can have a fixed power law  $\Sigma_{\text{SFR}} \propto \Sigma_{\text{gas}}^{1.5}$  when  $f_{\text{H}_2}$  and  $h_{\text{gas}}$  are roughly independent of  $\Sigma_{\text{gas}}$  (e.g., M51a, Kennicutt et al. 2007), but then steepen when the mass fraction of star-forming gas becomes a strong function of gas surface density in a manner characteristic of dwarf galaxies, large low surface brightness galaxies, or the outskirts of normal galaxies. Deviations from the  $\Sigma_{\text{SFR}}^{1.5}$  relation can also occur when  $h_{\text{gas}}$  changes quickly with decreasing  $\Sigma_{\text{gas}}$  in the flaring outer regions of the disks. Such flaring, for example, is observed for the Milky Way at  $R \gtrsim 10 \text{ kpc}$  (e.g., Wolfire et al. 2003, and references therein).

### 3.3. Local Pressure, Stellar Radiation, and H<sub>2</sub>-Fraction

Elmegreen (1993b) calculated the dependence of the ISM molecular fraction  $f_{\text{H}_2}$  on the local pressure and radiation field

<sup>5</sup> Small deviations in the GD-SF model at low surface densities owe to the sharp density threshold for star formation adopted in this model (see Schaye & Dalla Vecchia 2008, for a related discussion).

strength, including the effects of H<sub>2</sub> self-shielding and dust extinction. The calculations of Elmegreen (1993b) suggested that

$$f_{\text{H}_2} \propto P_{\text{ext}}^{2.2} j^{-1}, \quad (16)$$

where  $P_{\text{ext}}$  is the external pressure and  $j$  is the volume emissivity of the radiation field. Wong & Blitz (2002) used observations to determine the correlation between molecular fraction  $f_{\text{H}_2}$  and the hydrostatic equilibrium mid-plane pressure in galaxies, given by

$$P_{\text{ext}} \approx \frac{\pi}{2} G \Sigma_{\text{gas}} \left( \Sigma_{\text{gas}} + \frac{\sigma}{c_*} \Sigma_* \right), \quad (17)$$

where  $c_*$  is the stellar velocity dispersion and  $\sigma$  is the gas velocity dispersion (see Elmegreen 1989). From observations of seven disk galaxies and the Milky Way, Wong & Blitz (2002) determined that the observed molecular fraction scaled with pressure as

$$\Sigma_{\text{H}_2} / \Sigma_{\text{HI}} \propto P_{\text{ext}}^{0.8}. \quad (18)$$

Subsequently, Blitz & Rosolowsky (2004) and Blitz & Rosolowsky (2006) studied these correlations in a larger sample of 28 galaxies. Blitz & Rosolowsky (2006) found that if the mid-plane pressure was defined as

$$\frac{P_{\text{ext}}}{k} = 272 \text{ cm}^{-3} \text{ K} \left( \frac{\Sigma_{\text{g}}}{M_{\odot} \text{ pc}^{-2}} \right) \left( \frac{\Sigma_*}{M_{\odot} \text{ pc}^{-2}} \right)^{0.5} \times \left( \frac{\sigma}{\text{km s}^{-1}} \right) \left( \frac{h_*}{\text{pc}} \right)^{-0.5}, \quad (19)$$

where  $h_*$  is the stellar scale height, and if the local mass density was dominated by stars, then the molecular fraction scaled with  $P_{\text{ext}}$  as

$$\Sigma_{\text{H}_2} / \Sigma_{\text{HI}} \propto P_{\text{ext}}^{0.92}. \quad (20)$$

Wong & Blitz (2002) state that if the ISRF volume emissivity  $j \propto \Sigma_* \propto \Sigma_g$  and the stellar velocity dispersion was constant, then the Elmegreen (1993b) calculations would provide a relation  $f_{\text{H}_2} \propto P_{\text{ext}}^{1.7}$  much steeper than observed. Blitz & Rosolowsky (2006) suggested that if the stellar velocity dispersion scales as  $c_* \propto \Sigma_*^{0.5}$  and  $j \propto \Sigma_*$ , then the predicted scaling is closer to the observed scaling. These assumptions provide  $f_{\text{H}_2} \propto P_{\text{ext}}^{1.2}$ .

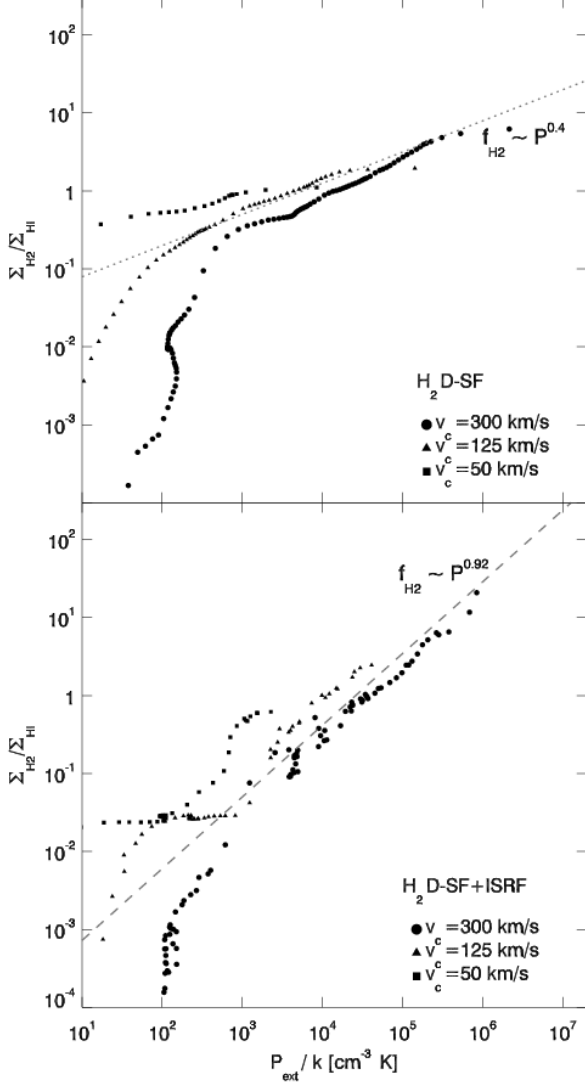


FIG. 9.— Molecular fractions as a function of external pressure in isolated disks. Shown are the molecular-to-atomic gas surface density ratios  $\Sigma_{\text{H}_2}/\Sigma_{\text{HI}}$  measured in radial bins as a function of the local external pressure  $P_{\text{ext}}$  defined by Blitz & Rosolowsky (2004) for galaxies with  $v_{\text{circ}} \approx 300 \text{ km s}^{-1}$  (circles),  $v_{\text{circ}} \approx 125 \text{ km s}^{-1}$  (triangles), and  $v_{\text{circ}} \approx 50 \text{ km s}^{-1}$  (squares) circular velocities. The simulations that include  $\text{H}_2$ -destruction by an ISRF (lower panel) follow the observed  $\Sigma_{\text{H}_2}/\Sigma_{\text{HI}} \propto P_{\text{ext}}^{0.9}$  power-law scaling (dashed line), while the simulations that do not include an ISRF (upper panel) have a weaker scaling than that found observationally ( $\Sigma_{\text{H}_2}/\Sigma_{\text{HI}} \sim P_{\text{ext}}^{0.4}$ , dotted line).

The relation between  $\Sigma_{\text{H}_2}/\Sigma_{\text{HI}}$  and  $P_{\text{ext}}$  can be measured for the simulated disks. Figure 9 shows  $\Sigma_{\text{H}_2}/\Sigma_{\text{HI}}$  as a function of  $P_{\text{ext}}$ , measured from the simulations according to Equation 19 in annuli, for simulated disks with (bottom panel) and without (top panel)  $\text{H}_2$ -destruction by an ISRF. The simulations with an ISRF scale in a similar way to the systems observed by Blitz & Rosolowsky (2006), while the simulated disks without an ISRF have a weaker scaling. The simulated galaxies have  $c_* \propto \Sigma_*^{0.5}$  and roughly constant gas velocity dispersions.

Given the scaling of the ISRF strength in the simulations, for which  $U_{\text{isrf}} \propto \Sigma_{\text{SFR}} \propto \Sigma_{\text{gas}}^{n_{\text{tot}}}$  with  $n_{\text{tot}} \sim 2-4$  according to the total gas SK relations measured in §3.2.1, and the scale-dependent SFE, which will instill the proportionality  $\Sigma_* \propto$

$\Sigma_{\text{gas}}^\beta$  with  $\beta \neq 1$  in general, the scaling between the molecular fraction and pressure  $f_{\text{H}_2} \propto P_{\text{ext}}^{0.9}$  is not guaranteed to be satisfied in galaxies with greatly varying SK relations. However, given the relation  $f_{\text{H}_2} \propto P_{\text{ext}}^{2.2} j^{-1}$  calculated by Elmegreen (1993b), a general relation between the molecular fraction and interstellar pressure can be calculated in terms of the power-law indices  $n$  of the total gas SK relation and  $\beta$  that describes the relative distribution gas and stars in the disk.

Assuming a steady state, the volume emissivity in the simulated ISM then scales with the gas surface density as

$$j \propto U_{\text{isrf}} \propto \Sigma_{\text{gas}}^{n_{\text{tot}}}. \quad (21)$$

Given the ISRF strength in the simulations and a proportionality of the stellar surface density with the total gas surface density of the form  $\Sigma_* \propto \Sigma_{\text{gas}}^\beta$ , we find that, with the scaling between the molecular fraction, pressure, and ISRF volume emissivity calculated by Elmegreen (1993b), the  $f_{\text{H}_2} - \Sigma_{\text{gas}}$  relation should follow

$$f_{\text{H}_2} \propto \Sigma_{\text{gas}}^{2.2(1+\beta/2)-n}. \quad (22)$$

If the molecular fraction scales with the mid-plane pressure as  $f_{\text{H}_2} \propto P^\alpha$ , then the index  $\alpha$  can be expressed in terms of the power-law dependences of the SK relation and the  $\Sigma_* - \Sigma_{\text{gas}}$  correspondence as

$$\alpha = \frac{2.2(1+\beta/2)-n}{1+\beta/2}. \quad (23)$$

The largest galaxy simulated, with a circular velocity of  $v_{\text{circ}} \approx 300 \text{ km s}^{-1}$ , has a total gas SK relation with a scaling  $\Sigma_{\text{SFR}} \propto \Sigma_{\text{gas}}^2$  (see Figure 6) and a nearly linear scaling of the stellar and gas surface densities ( $\beta \approx 0.97$ ). According to Equation 23, power-law index for this system is then expected to follow  $\alpha = 0.85$ . At the opposite end of the mass spectrum, the  $v_{\text{circ}} = 50 \text{ km s}^{-1}$  dwarf galaxy, which obeys a very different SK relation ( $n_{\text{tot}} \approx 4$ ) and  $\Sigma_* - \Sigma_{\text{gas}}$  scaling ( $\beta \approx 4$ ), has an expected  $\alpha \approx 0.87$ . These  $\alpha$  values are remarkably close to the relation observed by Blitz & Rosolowsky (2006), who find  $\alpha \approx 0.92$ . That the ISRF model reproduces the observed correlation in galaxies of different masses then owes to the opposite compensating effects of the scaling of  $j$  with  $\Sigma_{\text{gas}}$  and the  $\Sigma_* - \Sigma_{\text{gas}}$  scaling.

For the simulations that do not include an ISRF, the scaling between molecular fraction and pressure must be independent of the ISRF volume emissivity. We find that  $f_{\text{H}_2} \sim \Sigma_{\text{gas}}^{0.6}$  in these galaxies, with significant scatter, which provides the much weaker relation  $\Sigma_{\text{H}_2}/\Sigma_{\text{HI}} \sim P_{\text{ext}}^{0.4}$ . The simulations without an ISRF have  $f_{\text{H}_2} - P_{\text{ext}}$  scalings similar to this estimate or intermediate between this estimate and the observed relation.

The good agreement between the  $f_{\text{H}_2} - P_{\text{ext}}$  scaling in the simulations with an ISRF and the observations provide an *a posteriori* justification for the chosen scaling of the ISRF strength in the simulations (Equation 2), even as the ISRF strength was physically motivated by the generation of soft UV photons by young stellar populations. The robustness of the  $f_{\text{H}_2} - P_{\text{ext}}$  may be a consequence of the regulatory effects of  $\text{H}_2$ -destruction by the ISRF, which motivated in part the original calculations by Elmegreen (1993b), in concert with the influence of the external pressure (Elmegreen & Parravano 1994). However, we note that systems with a steep total gas SK relation, such as the  $v_{\text{circ}} \sim 50 \text{ km s}^{-1}$  and  $v_{\text{circ}} \sim 125 \text{ km s}^{-1}$  systems, do break from the  $f_{\text{H}_2} - P_{\text{ext}}$  relation in the very exterior of the disk where the molecular fraction quickly declines. Observations of M33, the real galaxy analogue to

the  $v_{\text{circ}} \sim 125 \text{ km s}^{-1}$  simulated galaxy, indicate that the system may deviate from the observed  $f_{\text{H}_2} - P_{\text{ext}}$  relation determined at higher surface densities in the very exterior of the disk (Gardan et al. 2007). The surface density of M33 in these exterior regions is dominated by gas rather than stars, and the Blitz & Rosolowsky (2006) relation may not be expected to hold under such conditions. The high-surface density regions of M33 do satisfy the  $f_{\text{H}_2} - P_{\text{ext}}$  relation (Blitz & Rosolowsky 2006), as does the simulated M33 analogue. We delay a more thorough examination of the exterior disk regions until further work.

Recently, Booth et al. (2007) presented a model of star formation based on a subgrid model for the formation of molecular clouds from thermally unstable gas in a multiphase ISM. In their model, molecular clouds are represented as ballistic particles which can coagulate through collisions. This is quite different from the treatment of ISM in our model, as we do not attempt to model molecular clouds on small scales via a subgrid model, but calculate the equilibrium abundance of molecular hydrogen using the local gas properties. Booth et al. (2007) show that their simulations also reproduce the molecular fraction-pressure relation of Blitz & Rosolowsky (2004, 2006). However, the interpretation of this relation in their model must be different from our interpretation involving the relation between the gas surface density, the stellar surface density, and the ISRF strength, because their model does not include the dissociating effects of the interstellar radiation field.

In addition, in contrast to our model, the global SK relation in simulations of Booth et al. (2007) does not show a break or steepening down to very small surface densities ( $\Sigma \approx 10^{-2} M_{\odot} \text{ pc}^{-2}$ ; see their Fig. 15). Given the differences, it will be interesting to compare results of different models of  $\text{H}_2$ -based star formation in more detail in future studies.

### 3.4. Star Formation and Angular Velocity

The SFR surface density  $\Sigma_{\text{SFR}}$  has been shown to correlate with the product of the gas surface density  $\Sigma_{\text{gas}}$  and the disk angular frequency  $\Omega$  as

$$\Sigma_{\text{SFR}} \simeq C_{\Sigma\Omega} \Sigma_{\text{gas}} \Omega \quad (24)$$

with the constant  $C_{\Sigma\Omega} = 0.017$  (Kennicutt 1998) and where the angular frequency is defined as

$$\Omega^2 = \frac{1}{R} \frac{d\Phi}{dR} \quad (25)$$

(e.g., §3.2.3 of Binney & Tremaine 1987). Star formation relations of this form have been forwarded to connect the SFR to the cloud-cloud collision time-scale (e.g., Wyse 1986; Wyse & Silk 1989; Tan 2000), to tie the gas consumption time-scale to the orbital time-scale (e.g., Silk 1997; Elmegreen 1997), or to reflect the correlation between the ISM density and the tidal density (Elmegreen 2002). These ideas posit that the  $\Sigma_{\text{SFR}} - \Sigma_{\text{gas}} \Omega$  correlation provides a reasonable physical interpretation of the  $\Omega \propto \sqrt{\rho}$  scaling.

Figure 10 shows the SFR surface density  $\Sigma_{\text{SFR}}$  as a function of the total gas surface density consumed per orbit  $C_{\Sigma\Omega} \Sigma_{\text{gas}} \Omega$  and molecular gas surface density consumed per orbit  $C_{\Sigma\Omega} \Sigma_{\text{H}_2} \Omega$ , compared to the observed  $\Sigma_{\text{SFR}} - \Sigma_{\text{gas}} \Omega$  relation Kennicutt (1998). The local values of  $\Sigma_{\text{gas}}$  and  $\Sigma_{\text{H}_2}$  are measured in radial annuli from the gas properties, while  $\Omega$  is measured from the rotation curve at the same location. The SFR surface density scales as  $\Sigma_{\text{gas}} \Omega$  at  $\Sigma_{\text{SFR}} \gtrsim 5 \times 10^{-3} M_{\odot} \text{ yr}^{-1} \text{ kpc}^{-2}$ . The offset between the disk-averaged

$\Sigma_{\text{SFR}} - \Sigma_{\text{gas}} \Omega$  relation found by Kennicutt (1998) and the simulated relation may owe in part to the typically higher values of  $\Omega$  in the disk interior that can affect the normalization of the azimuthally-averaged  $\Sigma_{\text{SFR}} - \Sigma_{\text{gas}} \Omega$  relation. This offset is comparable to the observed offset between the disk-averaged relation of Kennicutt (1998) and the spatially-resolved  $\Sigma_{\text{SFR}} - \Sigma_{\text{gas}} \Omega$  relation found in M51a by Kennicutt et al. (2007). As in the previous sections, scaling  $\Sigma_{\text{SFR}} - \Sigma_{\text{H}_2} \Omega$  works throughout the disk, while the  $\Sigma_{\text{SFR}} - \Sigma_{\text{gas}} \Omega$  scaling steepens significantly at lower surface densities where the molecular fraction is declining.

That the SFR in the simulated disks correlates well with the quantity  $\Sigma_{\text{gas}} \Omega$ , even though the SFR in the simulations is determined directly from the *local* molecular gas density and dynamical time without direct knowledge of  $\Omega$ , may be surprising. The correlation suggests that the local gas density should scale with  $\Omega$ , although the physical reason for such a correlation in our simulations is unclear. While previous examinations of the  $\Sigma_{\text{SFR}} - \Sigma_{\text{gas}} \Omega$  correlation have developed explanations of why  $\Omega \propto \sqrt{\rho_d}$ , these simulations have a coarser treatment of the ISM than is invoked in such models; the molecular fraction and SFR are primarily functions of the local density. The  $\Omega \sim \sqrt{\rho_d}$  correlation should then reflect the structural properties galaxy models rather than the detailed properties of the ISM that are somehow influenced by global processes in the disk.

The galaxy models used in the simulations remain roughly axisymmetric after their evolution, modulo spiral structure and disk instabilities. Hence, the fundamental equation that describes the gravitational potential  $\Phi$  of the galaxies is the Poisson equation

$$\frac{d^2\Phi}{dz^2} + \frac{d^2\Phi}{dR^2} + \Omega^2 = 4\pi G \rho_{\text{total}}. \quad (26)$$

where the density  $\rho_{\text{total}}$  reflects the total density of the multi-component system. If the form of the potential generated by  $\rho_{\text{total}}$  has the property that  $\Omega^2 = (1/R)d\Phi/dR \propto \rho_d$ , then the quantity  $\Sigma_{\text{gas}} \Omega$  will mimic the scaling of  $\Sigma_{\text{SFR}}$ . In the second Appendix, we examine the solutions for  $\Omega$  determined from Equation 26 for the limiting cases of locally disk-dominated ( $\rho_{\text{total}} \approx \rho_{\text{disk}}$ ) and halo-dominated ( $\rho_{\text{total}} \approx \rho_{\text{DM}}$ ) potentials, and show that typically  $\Omega \propto \sqrt{\rho_d} B(\rho_d)$  where  $B(\rho_d) \sim \mathcal{O}(1)$  is a weak function of density if the disk density is exponential with radius. This behavior suggests that whether the disk dominates the local potential, as is the case for massive galaxies, or the dark matter halo dominates the potential as it does in low-mass dwarfs, the angular frequency scales as  $\Omega \propto \sqrt{\rho_d}$  throughout most of the disk. Based on these calculations, we conclude that the correlation  $\Sigma_{\text{SFR}} \propto \Sigma_{\text{gas}} \Omega$  in the simulations is likely a consequence of the density-dependent star formation relation (Equation 4) and the galaxy structure inducing the correlation  $\Omega \propto \sqrt{\rho_d}$ . This correlation may be established during the formation of the exponential disk in the extended dark matter halo, and the correlation observed in real galaxies therefore may have a similar origin. Star formation may then correlate with  $\Sigma_{\text{gas}} \Omega$ , but not be directly controlled or influenced by the global kinematics of the disk.

### 3.5. Star Formation and Critical Surface Density Thresholds

Disk surface density, dynamical instabilities, and the formation of molecular clouds and stars may be connected. A single-component thin disk will experience growing axisymmetric instabilities if its surface mass density exceeds the crit-



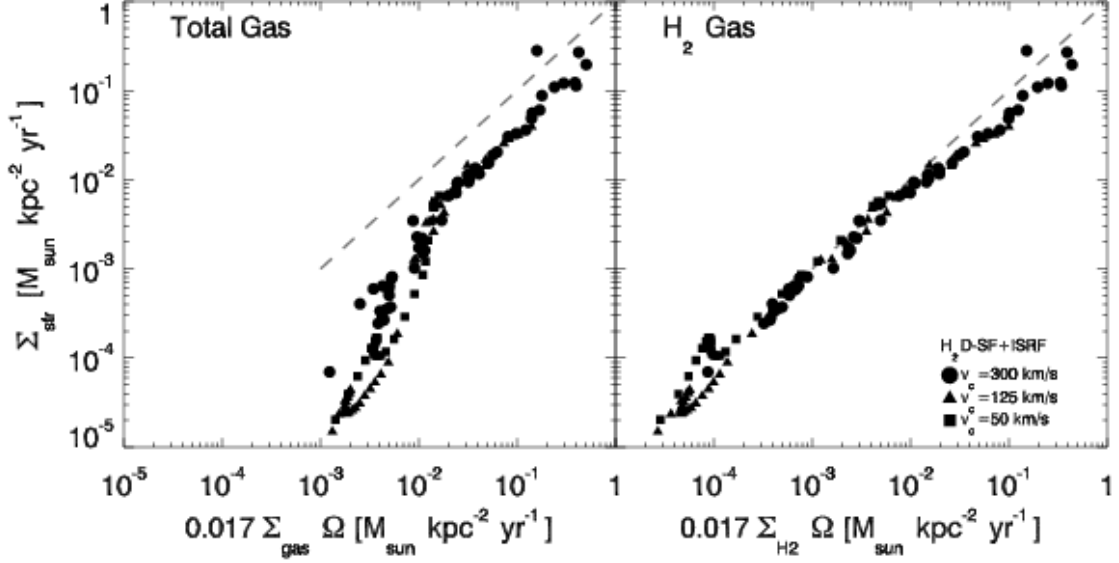


FIG. 10.— Star formation rate surface density  $\Sigma_{\text{SFR}}$  as a function of the total gas surface density consumed per orbit  $C_{\Sigma\Omega}\Sigma_{\text{gas}}\Omega$  (left panel) and molecular gas surface density consumed per orbit  $C_{\Sigma\Omega}\Sigma_{\text{H}_2}\Omega$  (right panel), where  $\Omega$  is the orbital frequency and the efficiency  $C_{\Sigma\Omega} = 0.017$  was determined from observations by Kennicutt (1998) (represented by the *dashed* line which extends over the range probed by observations). Shown are the local values of  $\Sigma_{\text{gas}}$ ,  $\Sigma_{\text{H}_2}$  and  $\Omega$  in annuli for galaxy models with circular velocities of  $v_{\text{circ}} = 50 \text{ km s}^{-1}$  (squares),  $v_{\text{circ}} = 125 \text{ km s}^{-1}$  (triangles), and  $v_{\text{circ}} = 300 \text{ km s}^{-1}$  (circles) evolved with atomic+molecular cooling and destruction of  $\text{H}_2$  by a local interstellar radiation field for  $t = 0.3 \text{ Gyr}$ . The star formation rate in the simulations display the correlations  $\Sigma_{\text{SFR}} \propto \Sigma_{\text{H}_2}\Omega$  and, in the high surface density region where the molecular gas and total gas densities are comparable,  $\Sigma_{\text{SFR}} \propto \Sigma_{\text{gas}}\Omega$ .

ical value  $\Sigma_Q$ , given by

$$\Sigma_Q(\sigma) \approx \frac{\alpha_Q \kappa \sigma}{\pi G}, \quad (27)$$

where  $\kappa$  is the epicyclic frequency

$$\kappa^2 = 2 \left( \frac{v^2}{R^2} + \frac{v}{R} \frac{dv}{dR} \right), \quad (28)$$

$\sigma$  is the characteristic velocity dispersion of the fluid, and the parameter  $\alpha_Q \sim \mathcal{O}(1)$  (Safronov 1960; Toomre 1964). For a two component system, consisting of stars with surface mass density  $\Sigma_*$  and velocity dispersion  $c_*$ , and gas with surface mass density  $\Sigma_{\text{gas}}$  and velocity dispersion  $\sigma$ , the instability criterion for axisymmetric modes with a wavenumber  $k$  can be expressed in terms of the normalized wavenumber  $q \equiv kc_*/\kappa$  and the ratio of velocity dispersions  $R \equiv \sigma/c_*$

$$Q_{\text{sg}}^{-1} \equiv \frac{2}{Q_s} \frac{q}{1+q^2} + \frac{2}{Q_g} R \frac{q}{1+q^2 R^2} > 1 \quad (29)$$

(Jog & Solomon 1984; Rafikov 2001), where  $Q_s = \Sigma_Q(c_*)/\Sigma_*$  and  $Q_g = \Sigma_Q(\sigma)/\Sigma_{\text{gas}}$ . The most unstable wavenumber  $q$  can be determined by maximizing this relation.

Elmegreen (1993a) considered another critical surface density  $\Sigma_A$ , given by

$$\Sigma_A \approx \frac{\alpha_A A \sigma}{\pi G} \quad (30)$$

where the parameter  $\alpha_A \sim \mathcal{O}(1)$ , and the Oort constant  $A$  is

$$A = -0.5R \frac{d\Omega}{dR} \quad (31)$$

(e.g., Binney & Tremaine 1987), above which density perturbations can grow through self-gravity before being disrupted by shear. This instability criterion has been shown to work well in Milky Way spiral arms (e.g., Luna et al. 2006) and ring galaxies (Vorobyov 2003). In regions of low shear, the magneto-Jeans instability may induce the growth of perturbations (e.g., Kim et al. 2002).

Observational evidence for connection between global disk instabilities and star formation has been a matter of considerable debate (e.g., Kennicutt 1989; Martin & Kennicutt 2001; Hunter et al. 1998; Boissier et al. 2003, 2007; Kennicutt et al. 2007; Yang et al. 2007). In particular, the existence of global star formation thresholds related to Toomre instability (e.g., Kennicutt 1989; Martin & Kennicutt 2001) has been challenged (Boissier et al. 2007). It is thus interesting to use model galaxies to explore the role of critical surface densities in star formation. While proper radiative transfer calculations are needed to assign either  $\text{H}\alpha$  or UV emissivities to the simulated disk galaxies, an indirect comparison between simulations and observations can be made by measuring surface mass densities, velocity dispersions, dynamical properties, and a characteristic extent of star formation in the model disks. These comparisons are presented in Figure 11, where the instability parameters  $Q_{\text{sg}}^{-1}$  and  $\Sigma_{\text{gas}}/\Sigma_A$  are plotted as a function of radius in the disk galaxies simulated with the  $\text{H}_2\text{D-SF+ISRF}$  molecular ISM and star formation model. For comparison with the two-fluid Toomre axisymmetric instability criterion, the parameter  $Q_{\text{sg}}$  is measured by determining the locally most unstable wavenumber  $q$  from  $Q_s$  and  $Q_g$  with  $\alpha = 0.69$  to approximate the observational results of Kennicutt (1989) and Martin & Kennicutt (2001). When examining the shearing instability criterion, the parameter  $\alpha_A = 2$  is chosen for comparison with the observational estimation of critical surface densities by Martin & Kennicutt (2001) and only the gas surface density is utilized. A “critical” radius  $R_{\text{SFR}}$  containing 99.9% of the total star formation in each simulated disk is measured and used as a proxy for the star formation threshold radius observationally determined from, e.g., the  $\text{H}\alpha$  emission.

The shearing instability criterion (upper panel Figure 11) is supercritical ( $\Sigma_{\text{gas}}/\Sigma_A > 1$ ) over the extent of star formation in the low-mass galaxy, but the larger galaxies are either marginally supercritical or subcritical. Given the large gas content in this dwarf system and that this comparison only

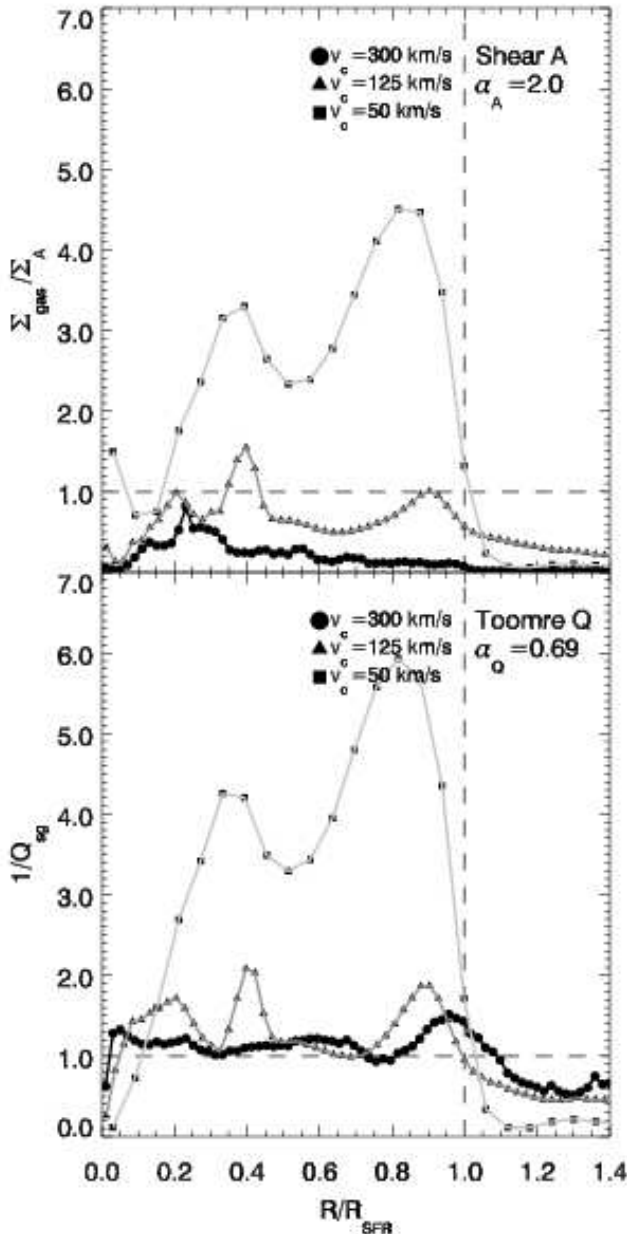


FIG. 11.— Stability parameters for two-fluid Toomre instability ( $Q_{\text{sg}}^{-1}$ , bottom panel) or shear instability ( $\Sigma_{\text{gas}}/\Sigma_A$ , top panel) as a function of radius normalized to the radius  $R_{\text{SFR}}$  containing 99.9% of the total active disk star formation. Shown are the parameters  $Q_{\text{sg}}^{-1}$  and  $\Sigma_{\text{gas}}/\Sigma_A$  for galaxy models with circular velocities of  $v_{\text{circ}} = 50 \text{ km s}^{-1}$  (squares, light gray lines),  $v_{\text{circ}} = 125 \text{ km s}^{-1}$  (triangles, dark gray lines), and  $v_{\text{circ}} = 300 \text{ km s}^{-1}$  (circles, black lines). The proportionality constants  $\alpha_Q = 0.69$  and  $\alpha_A = 2$  are taken to match the values used by Martin & Kennicutt (2001). For each simulated galaxy, the parameter  $Q_{\text{sg}}^{-1}$  approaches the transition to stability at the radius  $R_{\text{SFR}}$  beyond which only very little star formation operates. An increase in the stability against growing shearing modes also occurs near  $R_{\text{SFR}}$  for the simulated disks, but the transition is less uniform than for Toomre instability.

uses the gas surface mass density  $\Sigma_{\text{gas}}$ , the result is unsurprising. While the  $v_{\text{circ}} \sim 125 \text{ km s}^{-1}$  and  $v_{\text{circ}} \sim 300 \text{ km s}^{-1}$  galaxies are subcritical at  $R = R_{\text{SFR}}$ , we note that there is still a noticeable drop in  $\Sigma_{\text{gas}}/\Sigma_A$  near  $R = R_{\text{SFR}} \sim 1$  for these systems.

Interestingly, with the chosen definition of  $R_{\text{SFR}}$ , the bottom panel of Figure 11 shows that the two-component Toomre instability parameter  $Q_{\text{sg}}$  is a remarkably accurate indicator of where the majority of star formation operates in the simulated disk galaxies. Each galaxy approaches the  $Q_{\text{sg}} \sim 1$  transition near  $R_{\text{SFR}}$ , demonstrating that much of the star formation is operating within Toomre-unstable regions of the disks. These results appear most consistent with the observations by Kennicutt (1989), Martin & Kennicutt (2001), and Yang et al. (2007), who find that star formation operates most efficiently in regions that are gravitationally unstable.

Our simulations are also qualitatively consistent with the theoretical findings of Li et al. (2005a,b, 2006), who used hydrodynamical simulations of isolated galaxies with sink particles to represent dense molecular gas and star clusters. They found that if the accretion onto the sink particles resulted in star formation with some efficiency, the two-component Toomre parameter was  $Q_{\text{sg}} < 1.6$  in regions of active star formation. Although a direct comparison is difficult given their use of sink particles, we similarly find that the majority of star formation in our simulations occurs in regions of the disk where  $Q_{\text{sg}} \lesssim 1$ .

In related theoretical work, a gravothermal instability criterion for star formation was explored by Schaye (2004), who suggested that the decrease in thermal velocity dispersion associated with the atomic-to-molecular transition in the dense ISM may induce gravitational instability and the corresponding connection between critical surface densities and star formation. The simulated galaxies do experience a decline in thermal sound speed near the  $Q_{\text{sg}} \sim 1$  transition, consistent with the mechanism advocated by Schaye (2004). However, of our  $\text{H}_2\text{D-SF+ISRF}$  simulations (that include physics necessary for such instability), only the dwarf galaxy model displays a sharp transition in  $Q_{\text{sg}}$  near the critical radius while the stability of the other, more massive galaxies are more strongly influenced by the turbulent gas velocity dispersion and have more modest increases in  $Q_{\text{sg}}$ . Further, we note that the gravothermal mechanism suggested by Schaye (2004) should not operate in isothermal treatments of the ISM such as those presented by Li et al. (2005a,b, 2006). Similarly our GD-SF simulations, which are effectively isothermal ( $T \approx 10^4 \text{ K}$ ) at ISM densities, display similar transitions to  $Q_{\text{sg}} \lesssim 1$  at the critical radius even as such simulations do not include a cold phase to drive gravitational instability.

We stress that the definition of  $R_{\text{SFR}}$  may affect conclusions about the importance of threshold surface densities. For instance, if a 90% integrated star formation threshold was used  $R_{\text{SFR}}$  would be lowered to 0.3–0.6 of the chosen value and the subsequent interpretations about the applicability of the instability parameter  $Q_{\text{sg}}$  could be quite different. Detailed radiative transfer calculations may therefore be necessary to determine the integrated star formation fraction that brings  $R_{\text{SFR}}$  in the best agreement with observationally-determined critical radii.

### 3.6. Temperature and Density Structure of the ISM

The temperature and density structure of interstellar gas is determined by a variety of processes including radiative heating, cooling, and, importantly, turbulence (see, e.g.,

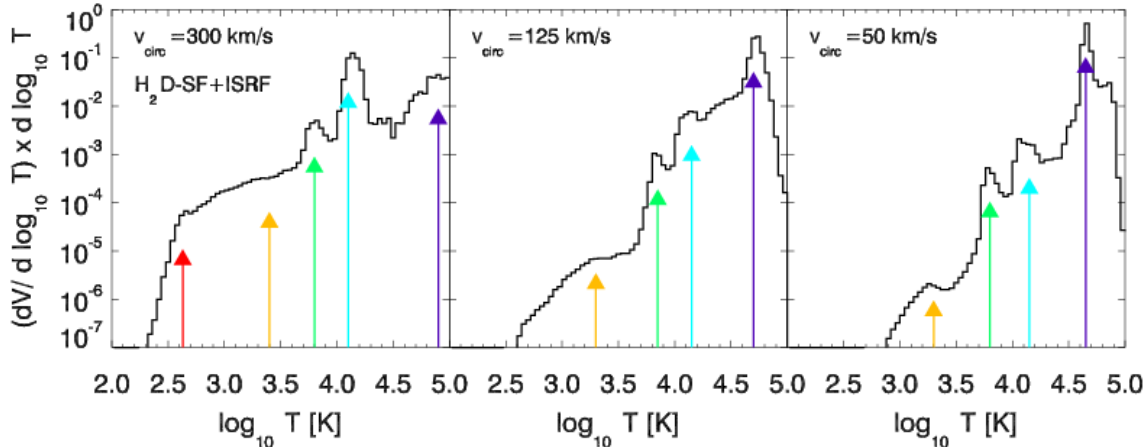


FIG. 12.— Temperature structure of the interstellar medium in galaxies of different mass. Shown are the probability distribution functions (PDF) of the fractional volume of the ISM with a temperature  $T$  (black histograms), for systems with circular velocities of  $v_{\text{circ}} = 300 \text{ km s}^{-1}$  (left panel),  $v_{\text{circ}} = 125 \text{ km s}^{-1}$  (middle panel), and  $v_{\text{circ}} = 50 \text{ km s}^{-1}$  (right panel). The simulations use the  $\text{H}_2\text{D-SF+ISRF}$  model to evolve the systems in isolation for  $t = 0.3 \text{ Gyr}$ . The peaks in the temperature PDF correspond to regions of density-temperature phase space where the cooling time  $t_{\text{cool}}$  has local maxima (i.e., where  $t_{\text{cool}}$  is locally a weak function of density). These peaks in the temperature PDF correspond to features in the density PDF, and the colored arrows highlight regions that can be modeled approximately as separate isothermal phases (i.e., lognormals) in the density PDF (see Figure 13 and §3.6 of the text for details).

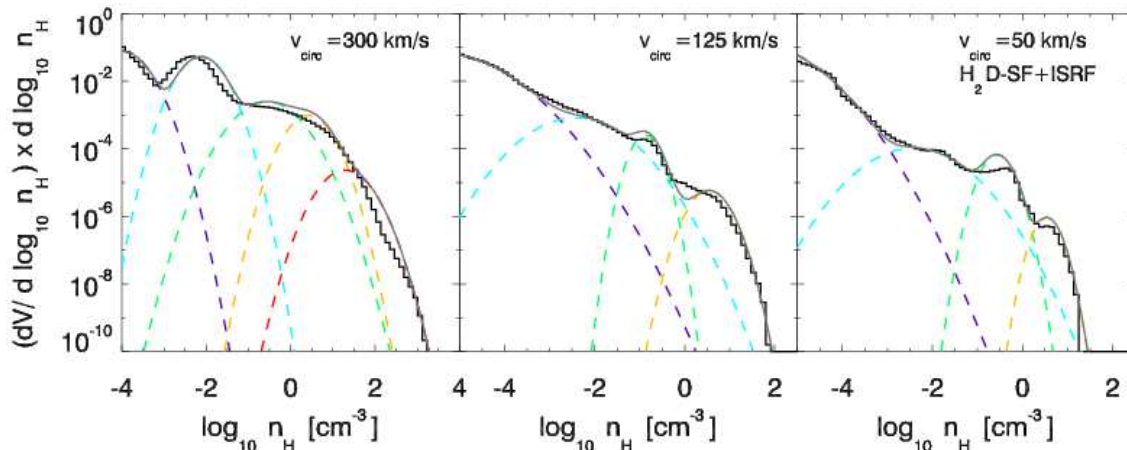


FIG. 13.— Density structure of the interstellar medium in galaxies of different mass. Shown are the probability distribution functions (PDF) of the fractional volume of the ISM with a density  $n_{\text{H}}$  (black histograms), for systems with circular velocities of  $v_{\text{circ}} = 300 \text{ km s}^{-1}$  (left panel),  $v_{\text{circ}} = 125 \text{ km s}^{-1}$  (middle panel), and  $v_{\text{circ}} = 50 \text{ km s}^{-1}$  (right panel) for the  $\text{H}_2\text{D-SF+ISRF}$  model at  $t = 0.3 \text{ Gyr}$ . The features in the density PDF correspond to regions of density-temperature phase space where the cooling time  $t_{\text{cool}}$  has local maxima (i.e., where  $t_{\text{cool}}$  is locally a weak function of density). The density PDF of the ISM in these simulated galaxies is not well-modeled by a single log-normal, except at the high-density tail. The figure shows that the density PDF may be modeled approximately as a sum of isothermal phases (i.e., lognormal PDFs in density, colored dashed lines), where the characteristic density of each phase is determined by using the ISM equation-of-state to find the typical density of peaks in the temperature PDF (see Figure 12 and §3.6 of the text for details).

Elmegreen 2002). The calculation of the density probability distribution function (PDF) of an isothermal gas, defined as a volume fraction of gas with a given density, suggests that the PDF will resemble a lognormal distribution with a dispersion  $\sigma$  that scales linearly with the mean gas Mach number  $\sigma \propto \beta M$ . The origin of the lognormal form is discussed in detail in Padoan et al. (1997) and Passot & Vázquez-Semadeni (1998). For a non-isothermal gas the density PDF may more generally follow a power-law distribution (Passot & Vázquez-Semadeni 1998; Scalo et al. 1998).

Although the lognormal PDF was initially discussed in the context of molecular clouds, Wada & Norman (2001) found that two-dimensional numerical simulations of a multiphase ISM on galactic scales produced a lognormal density PDF for dense gas, while at low densities gas followed a flatter distribution in  $\log \rho$  (see Wada & Norman 2007; Wada 2007, for more recent investigations of this issue). A similar PDF

was found in a cosmological simulation of galaxy formation at  $z \approx 4$  by Kravtsov (2003). Motivated in part by the result of Wada & Norman (2001), Elmegreen (2002) suggested that the SK relation could be explained in terms of the density PDF of ISM gas if a fraction  $f_c$  of gas that resides above some critical density threshold  $\rho_c$  converts into stars with a constant efficiency and  $\rho_c$  scales linearly with the average ISM density  $\langle \rho \rangle$ . Similarly, Kravtsov (2003) found that the fraction of dense gas in cosmological simulations of disk galaxy formation at redshifts  $z \gtrsim 4$  varied with the surface density in a manner to produce the  $\Sigma_{\text{SFR}} \propto \Sigma_{\text{gas}}^{1.4}$  relation at high surface densities. The gas density distribution in these simulations also followed a log-normal PDF at large densities and flattened at lower densities (see also Kravtsov & Gnedin 2005).

Joung & Mac Low (2006) used three-dimensional models of the stratified ISM to demonstrate that supernovae explosions can act to regulate star formation by inputting energy on small scales. Their scheme produced temperature and density

structures consistent with those observed in the real ISM, with density and temperature PDFs that contain multiple peaks. Tasker & Bryan (2007) found the density PDF in their multiphase simulations could be approximated by a single lognormal at high densities, but exhibited deviations from the lognormal in the form of peaks and dips at smaller densities.

Figure 12 shows the probability distribution function (PDF) of the fractional volume in the ISM at a temperature  $T$  in the H<sub>2</sub>D-SF+ISRF simulations at  $t = 0.3$  Gyr. The temperature PDF is measured by assigning an effective volume to each particle based on its mass and density, counting the particles in bins of fixed width in  $\log_{10} T$ , and then normalizing by the total effective volume of the ISM. The temperature PDF displays structure corresponding to gas at several phases. These temperature peaks correspond to features in the density-temperature phase diagram of the ISM, set by the cooling and heating processes. The abundance of gas in different regions of this diagram depend on the local cooling time, with regions corresponding to long local cooling times becoming more populated. The overall gravitational potential of the system also influences the density of gas in the disks and thus indirectly influences cooling and abundance of cold, dense gas, as denser ISM gas can reach lower equilibrium temperatures. Figure 12 shows that the temperature PDFs of the galaxies do differ, with more massive galaxies containing more volume at low ISM temperatures. In smaller mass galaxies, the ISM densities are lower, gas distributions are more extended, and the abundance of cold gas is greatly decreased.

Figure 13 shows the PDF of gas densities for each model galaxy in the H<sub>2</sub>D-SF+ISRF model at  $t = 0.3$  Gyr. The density PDFs are measured in the same manner as the temperature PDFs, but the particles are binned according to the  $\log_{10} n_{\text{H}}$ . Each galaxy has a PDF with noticeable features that change depending on the galaxy mass scale. None of the density PDFs are well represented by a single lognormal distribution, reflecting the multiple peaks apparent in the temperature PDFs (Figure 12).

Motivated by the multiphase structure of the ISM displayed in Figure 12, a model of the density PDFs can be constructed by identifying characteristic temperature peaks in the temperature PDF and assigning separate lognormal distributions to represent each approximately isothermal gas phase. The colored arrows in Figure 12 identify characteristic temperatures in the ISM of each galaxy. The characteristic density corresponding to each selected temperature, determined by the median equation-of-state calculated using Cloudy, is employed as the mean of a lognormal distribution used to model a feature in the density PDF (colored dashed lines in Figure 13). The heights and widths of the lognormals are constrained to provide the same relative volume fraction in the density PDFs as the phase occupies in the temperature PDF, resulting in a model shown by the solid gray lines in Figure 13.

Clearly the ISM is best understood in terms of a continuous distribution of temperatures, represented in the simulations by Figure 12, but the multiphase model of the density PDFs provides some conceptual insight into the ISM phase structure. First, the model of separate isothermal ISM phases can capture the prominent features of the density PDFs. Second, the galaxies share common features in the density (and temperature) PDFs, such as a warm neutral phase ( $\log_{10} T \sim 3.8$ ) and the mix of cold neutral and molecular gas at low temperatures ( $\log_{10} T \lesssim 3.5$ ). Third, the relative widths of the lognormal distributions representing the dense ISM in each

galaxy increase with increasing galaxy mass (i.e., the orange lognormals centered near  $\log_{10} n_{\text{H}} \sim 0.5$ ), as do their normalizations. The increasing widths of the lognormals mimic the increasing velocity dispersions (and turbulent Mach numbers) of the dense gas in the more massive galaxy models.

Note that for the ISM of the  $v_{\text{circ}} = 300 \text{ km s}^{-1}$  system the cold dense phase contributes the majority of the ISM by mass, while shock heated gas at  $T \sim 10^5 \text{ K}$  contributes the largest ISM fraction by volume. We note that this result qualitatively resembles the effect of the volume-averaged equation-of-state utilized in subgrid models of the multiphase ISM (e.g. Springel & Hernquist 2003a).

For purposes of calculating the overall SFE of galaxies, our results suggest that approximating the density PDF by a single lognormal distribution is overly simplistic. The detailed shape of the PDF is set by global properties of galaxies and heating and cooling processes in their ISM and can therefore be expected to vary from system to system. Nevertheless, a single PDF modeling may be applicable for the cases when most of the ISM mass is in one dominant gas phase (e.g., dense cold gas), as is the case for the massive galaxy in our simulations. We leave further exploration of this subject for future work.

#### 4. DISCUSSION

Results presented in the previous sections indicate that star formation prescriptions based on the local abundance of molecular hydrogen lead to interesting features of the global star formation relations.

We show that the inclusion of an interstellar radiation field is critical to control the amount of diffuse H<sub>2</sub> at low gas densities. For instance, without a dissociating ISRF the low mass dwarf galaxy eventually becomes almost fully molecular, in stark contrast with observations. We also show that without the dissociating effect of the ISRF our model galaxies produce a much flatter relation between molecular fraction  $f_{\text{H}_2}$  and pressure  $P_{\text{ext}}$ , as can be expected from the results of Elmegreen (1993a). Including H<sub>2</sub>-destruction by an ISRF results in a  $f_{\text{H}_2} - P_{\text{ext}}$  relation in excellent agreement with the observations of Wong & Blitz (2002) and Blitz & Rosolowsky (2004, 2006).

Our model also predicts that the relation between  $\Sigma_{\text{SFR}}$  and  $\Sigma_{\text{gas}}$  should not be universal and can be considerably steeper than the canonical value of  $n_{\text{tot}} = 1.4$ , even if the three-dimensional Schmidt relation in molecular clouds is universal. The slope of the relation is controlled by the dependence of molecular fraction (i.e., fraction of star forming gas) on the total local gas surface density. This relation is non-trivial because the molecular fraction is controlled by pressure and ISRF strength, and can thus vary between different regions with the same total gas surface density. The relation can also be different in the regions where the disk scale-height changes rapidly (e.g., in flaring outer regions of disks), as can be seen from equation 15 (see also Schaye & Dalla Vecchia 2008). We show that the effect of radial variations in the molecular fraction  $f_{\text{H}_2}$  and gas scale heights ( $h_{\text{SFR}}$  and  $h_{\text{gas}}$ ) on the SFR can be accounted for in terms of a structural, SK-like correlation,  $\Sigma_{\text{SFR}} \propto f_{\text{H}_2} h_{\text{SFR}} h_{\text{gas}}^{-1.5} \Sigma_{\text{gas}}^{1.5}$ , that trivially relates the local SFR to the consumption of molecular gas with an efficiency that scales with the local dynamical time.

A generic testable prediction of our model is that deviations from the SK  $\Sigma_{\text{SFR}} - \Sigma_{\text{gas}}$  relation are expected in galaxies or regions of galaxies where the molecular fraction is declining or much below unity. As we discussed above, star formation in the molecule-poor ( $f_{\text{H}_2} \sim 0.1$ ) galaxy M33 supports

this view as its total gas SK power-law index is  $n_{\text{tot}} \approx 3.3$  (Heyer et al. 2004). While our simulations of an M33 analogue produce a steep SK power-law, the overall SFE in our model galaxies lies below that observed for M33. However, as recently emphasized by Gardan et al. (2007), the highest surface density regions of M33 have unusually efficient star formation compared with the normalization of the Kennicutt (1998) relation and so the discrepancy is not surprising. Given that dwarf galaxies generally have low surface densities and are poor in molecular gas, it will be interesting to examine SK relation in other small-mass galaxies.

Another example of a low-molecular fraction galaxy close to home is M31, which has only a fraction  $f_{\text{H}_2} \approx 0.07$  of its gas in molecular form within 18 kpc of the galactic center (Nieten et al. 2006). Our model would predict that this galaxy should deviate from the total gas SK relation found for molecular-rich galaxies. Observationally, the SK relation of M31 measured by Boissier et al. (2003) is rather complicated and even has an increasing SFR with decreasing gas density over parts of the galaxy. Low molecular fractions can also be expected in the outskirts of normal galaxies and in the disks of low surface brightness galaxies. The latter have molecular fractions of only  $f_{\text{H}_2} \lesssim 0.10$  (Matthews et al. 2005; Das et al. 2006), and we therefore predict that they will not follow the total gas SK relation obeyed by molecule-rich, higher surface density galaxies. At the same time, LSBs do lie on the same relation between  $\text{H}_2$  mass and far infrared luminosity as higher surface brightness (HSB) galaxies (Matthews et al. 2005), which suggests that the dependence of star formation on molecular gas may be the same in both types of galaxies.

An alternative formulation of the global star formation relation is based on the angular frequency of disk rotation:  $\Sigma_{\text{SFR}} \propto \Sigma_{\text{gas}} \Omega$ . That this relation works in real galaxies is not trivial, because star formation and dynamical time-scale depend on the local gas density, while  $\Omega$  depends on the total mass distribution *within* a given radius. Although several models were proposed to explain such a correlation (see, e.g., Kennicutt 1998; Elmegreen 2002, for reviews), we show in §3.4 and the second Appendix that the star formation correlation with  $\Omega$  can be understood as a fortuitous correlation of  $\Omega$  with gas density of  $\Omega \propto \rho_{\text{gas}}^\alpha$ , where  $\alpha \approx 0.5$ , for self-gravitating exponential disks or exponential disks embedded in realistic halo potentials. Moreover, we find that  $\Sigma_{\text{SFR}} \propto \Sigma_{\text{gas}} \Omega$  breaks down at low values of  $\Sigma_{\text{gas}} \Omega$  where the molecular fraction declines, similarly to the steepening of the SK relation. Our models therefore predict that the  $\Sigma_{\text{SFR}} \propto \Sigma_{\text{H}_2} \Omega$  relation is more robust than the  $\Sigma_{\text{SFR}} \propto \Sigma_{\text{gas}} \Omega$  relation.

An important issue related to the global star formation in galaxies is the possible existence of star formation thresholds (Kennicutt 1998; Martin & Kennicutt 2001). Such thresholds are expected to exist on theoretical grounds, because the formation of dense, star-forming gas is thought to be facilitated by either dynamical instabilities (see, e.g., Elmegreen 2002; McKee & Ostriker 2007, for comprehensive reviews) or gravothermal instabilities (Schaye 2004). We find that the two-component Toomre instability threshold that accounts for both stars and gas,  $Q_{\text{sg}} < 1$ , works well in predicting the transition from atomic gas, inert to star formation, to the regions where molecular gas and star formation occur in our simulations. Our results are in general agreement with Li et al. (2005b,a, 2006), who used sink-particle simulations of the dense ISM in isolated galaxies to study the relation between star formation and the development of gravitational instabil-

ities, and with observations of star formation in the LMC (Yang et al. 2007). Our simulations further demonstrate the importance of accounting for all mass components in the disk to predict correctly which regions galactic disks are gravitationally unstable.

Given that our star formation prescription is based on molecular hydrogen, the fact that  $Q_{\text{sg}}$  is a good threshold indicator may imply that gravitational instabilities strongly influence the abundance of dense, molecular gas in the disk. Conversely, the gas at radii where the disk is stable remains at low density and has a low molecular fraction. We find that in our model galaxies, the shear instability criterion of Elmegreen (1993a) does not work as well as the Toomre  $Q_{\text{sg}}$ -based criterion. Almost all of the star formation in our model galaxies occurs at surface densities  $\Sigma_{\text{gas}} \gtrsim 3 M_\odot \text{pc}^{-2}$ , which is formally consistent with the Schaye (2004) constant surface density criterion for gravothermal instability. However, as Figure 6 shows, we do not see a clear indication of threshold at a particular surface density and our GD-SF models that have an effectively isothermal ISM with  $T \approx 10^4 \text{K}$  (and hence do not have a gravothermal instability) still show a good correlation between regions where  $Q_{\text{sg}} < 1$  and regions where star formation operates.

Our results have several interesting implications for interpretation of galaxy observations at different epochs. First, low molecular fractions in dwarf galaxies mean that only a small fraction of gas is participating in star formation at any given time. This connection between SFE and molecular hydrogen abundance may explain why dwarf galaxies are still gas rich today compared to larger mass galaxies (Geha et al. 2006), without relying on mediation of star formation or gas blowout by supernovae. Note that a similar reasoning may also explain why large LSBs at low redshifts are gas rich but anemic in their star formation. Understanding the star formation and evolution of dwarf galaxies is critical because they serve as the building blocks of larger galaxies at high redshifts. Such small-mass galaxies are also expected to be the first objects to form large masses of stars and should therefore play an important role in enrichment of primordial gas and the cosmic star formation rate at high redshifts (Hopkins 2004; Hopkins & Beacom 2006).

The star-forming disks at  $z \sim 2$  that may be progenitors of low-redshift spiral galaxies are observed to lack centrally-concentrated bulge components (Elmegreen et al. 2007). Given that galaxies are expected to undergo frequent mergers at  $z > 2$ , bulges should have formed if a significant fraction of baryons are converted into stars during such mergers (e.g., Gnedin et al. 2000). The absence of the bulge may indicate that star formation in the gas rich progenitors of these  $z \sim 2$  systems was too slow to convert a significant fraction of gas into stars. This low SFE can be understood if the high cosmic UV background, low-metallicities, and low dust content of high- $z$  gas disks keep their molecular fractions low (Pelupessy et al. 2006), thereby inhibiting star formation over most of gas mass and keeping the progenitors of the star-forming  $z \sim 2$  disks mostly gaseous. Gas-rich progenitors may also help explain the prevalence of extended disks in low-redshift galaxies despite the violent early merger histories characteristic of  $\Lambda$ CDM universes, as gas-rich mergers can help build high-angular momentum disk galaxies (Robertson et al. 2006a). Mergers of mostly stellar disks, on the other hand, would form spheroidal systems.

Our results may also provide insight into the interpretation of the results of Wolfe & Chen (2006), who find that

the SFR associated with neutral atomic gas in damped Lyman alpha (DLA) systems is an order of magnitude lower than predicted by the local Kennicutt (1998) relation. The DLAs in their study sample regions with column densities  $N_{\text{H}} \approx 2 \times 10^{21} \text{ cm}^{-2}$ , or surface gas densities of  $\Sigma_{\text{DLA}} \approx 20 M_{\odot} \text{ pc}^{-2}$ , assuming a gas disk with a thickness of  $h \approx 100 \text{ pc}$ . Suppose the local SK relation steepens from the local relation with the slope  $n_0 = 1.4$  to a steeper slope  $n_1$  below some surface density  $\Sigma_{\text{b}} > \Sigma_{\text{DLA}}$ . Then for  $\Sigma_{\text{gas}} < \Sigma_{\text{b}}$ , the SFR density will be lower than predicted by the local relation by a factor of  $(\Sigma_{\text{gas}}/\Sigma_{\text{b}})^{n_1-n_0}$ . For  $n_0 = 1.4$  and  $n_1 = 3$  the SFR will be suppressed by a factor of  $> 10$  for  $\Sigma_{\text{gas}}/\Sigma_{\text{b}} < 0.25$ . Thus, the results Wolfe & Chen (2006) can be explained if the total gas SK relation at  $z \sim 3$  steepens below  $\Sigma_{\text{gas}} \lesssim 100 M_{\odot} \text{ pc}^{-2}$ . We suggest that if the majority of the molecular hydrogen at these redshifts resides in rare, compact, and dense systems (e.g., Zwaan & Prochaska 2006), then both the lack of star formation and the rarity of molecular hydrogen in damped Ly $\alpha$  absorbers may be explained simultaneously.

Our results also indicate that the thermodynamics of the ISM can leave an important imprint on its density probability distribution. Each thermal phase in our model galaxies has its own log-normal density distribution. Our results thus imply that using a single lognormal PDF to build a model of global star formation in galaxies (e.g., Elmegreen 2002; Wada & Norman 2007) is likely an oversimplification. Instead, the global star formation relation may vary depending on the dynamical and thermodynamical properties of the ISM. We can thus expect differences in the SFE between the low-density and low-metallicity environments of dwarf and high-redshift galaxies and the higher-metallicity, denser gas of many large nearby spirals. Note that many of the results and effects we discuss above may not be reproduced with a simple 3D density threshold for star formation, as commonly implemented in galaxy formation simulations. Such a threshold can reproduce the atomic-to-molecular transition only crudely and would not include effects of the local interstellar radiation field, metallicity and dust content, etc.

A clear caveat for our work is that the simulation resolution limits the densities we can model correctly. At high densities, the gas in our simulations is over-pressurized to avoid numerical Jeans instability. The equilibrium density and temperature structure of the ISM and the molecular fraction are therefore not correct in detail. Note, however, that our pressurization prescription is designed to scale with the resolution, and should converge to the ‘‘correct’’ result as the resolution improves. In any event, the simulations likely do not include all the relevant physics shaping density and temperature PDFs of the ISM in real galaxies. The results may of course depend on other microphysics of the ISM as they influence both the temperature PDF and the fraction of gas in a high-density, molecular form. Future simulations of the molecular ISM may need to account for new microphysics as they resolve scales where such processes become important.

## 5. SUMMARY

Using hydrodynamical simulations of the ISM and star formation in cosmologically motivated disk galaxies over a range of representative masses, we examine the connection between molecular hydrogen abundance and destruction, observed star formation relations, and the thermodynamical structure of the interstellar medium. Our simulations provide a variety of new insights into the mass dependence of star formation efficiency in galaxies. A summary of our methodology and results fol-

lows.

1. A model of heating and cooling processes in the interstellar medium (ISM), including low-temperature coolants, dust heating and cooling processes, and heating by the cosmic UV background, cosmic rays, and the local interstellar radiation field (ISRF), is calculated using the photoionization code Cloudy (Ferland et al. 1998). Calculating the molecular fraction of the ISM enables us to implement a prescription for the star formation rate (SFR) that ties the SFR directly to the molecular gas density. The ISM and star formation model is implemented in the SPH/N-body code GADGET2 (Springel 2005) and used to simulate the evolution of isolated disk galaxies.
2. We study the correlations between gas surface density ( $\Sigma_{\text{gas}}$ ), molecular gas surface density ( $\Sigma_{\text{H}_2}$ ), and SFR surface density ( $\Sigma_{\text{SFR}}$ ). We find that in our most realistic model that includes heating and destruction of  $\text{H}_2$  by the interstellar radiation field, the power law index of the SK relation,  $\Sigma_{\text{SFR}} \propto \Sigma_{\text{gas}}^{n_{\text{tot}}}$  (measured in annuli) varies from  $n_{\text{tot}} \sim 2$  in massive galaxies to  $n_{\text{tot}} \gtrsim 4$  in small mass dwarfs. The corresponding slope of the  $\Sigma_{\text{SFR}} \propto \Sigma_{\text{H}_2}^{n_{\text{mol}}}$  molecular-gas Schmidt-Kennicutt relation is approximately the same for all galaxies, with  $n_{\text{mol}} \approx 1.3$ . These results are consistent with observations of star formation in different galaxies (e.g., Kennicutt 1998; Wong & Blitz 2002; Boissier et al. 2003; Heyer et al. 2004; Boissier et al. 2007; Kennicutt et al. 2007).
3. In our models, the SFR density scales as  $\Sigma_{\text{SFR}} \propto f_{\text{H}_2} h_{\text{SFR}} h_{\text{gas}}^{-1.5} \Sigma_{\text{gas}}^{1.5}$ , where  $h_{\text{gas}}$  is the scale-height of the ISM and  $h_{\text{SFR}}$  is the scale-height of star-forming gas. The different  $\Sigma_{\text{SFR}} - \Sigma_{\text{gas}}$  relations in galaxies of different mass and in regions of different surface density in our models therefore owe to the dependence of molecular fraction  $f_{\text{H}_2}$  and scale height of gas on the gas surface density.
4. We show that the  $\Sigma_{\text{SFR}} \propto \Sigma_{\text{gas}} \Omega$  and  $\Sigma_{\text{SFR}} \propto \Sigma_{\text{H}_2} \Omega$  correlations describe the simulations results well where the molecular gas and total gas densities are comparable, while the simulations deviate from  $\Sigma_{\text{SFR}} \propto \Sigma_{\text{gas}} \Omega$  (e.g., Kennicutt 1998) at low  $\Sigma_{\text{gas}}$  owing to a declining molecular fraction. We demonstrate that these relations may owe to the fact that the angular frequency and the disk-plane gas density are generally related as  $\Omega \propto \sqrt{\rho}$  for exponential disks if the potential is dominated by either the disk, a Navarro et al. (1996) halo, Hernquist (1990) halo, or an isothermal sphere. The correlation of  $\Sigma_{\text{SFR}}$  with  $\Omega$  is thus a secondary correlation in the sense that  $\Omega \propto \sqrt{\rho}$  is set during galaxy formation and  $\Omega$  does not directly influence star formation.
5. The role of critical surface densities for shear instabilities ( $\Sigma_A$ ) and Toomre (1964) instabilities ( $\Sigma_Q$ ) in star formation (e.g., Martin & Kennicutt 2001) is examined in the context of the presented simulations. We find that the two-component Toomre instability criterion  $Q_{\text{sg}} < 1$  is an accurate indicator of the star-forming regions of disks, and that gravitational instability and star formation are closely related in our simulations. Further, the

$Q_{\text{sg}}$  criterion works even in simulations in which cooling is restricted to  $T > 10^4$  K where gravothermal instability cannot operate.

6. Our simulations that include H<sub>2</sub>-destruction by an ISRF naturally reproduce the observed scaling  $f_{\text{H}_2} \propto P_{\text{ext}}^{0.9}$  between molecular fraction and external pressure (e.g., Wong & Blitz 2002; Blitz & Rosolowsky 2004, 2006), but we find that simulations without an ISRF have a weaker scaling  $f_{\text{H}_2} \propto P_{\text{ext}}^{0.4}$ . We calculate how the connection between the scalings of the gas surface density, the stellar surface density, and the ISRF strength influence the  $f_{\text{H}_2} - P_{\text{ext}}$  relation in the ISM, and show how the simulated scalings reproduce the  $f_{\text{H}_2} - P_{\text{ext}}$  relation even as the power-law index of the total gas Schmidt-Kennicutt relation varies dramatically from galaxy to galaxy.
7. We present a method for mitigating numerical Jeans fragmentation in Smoothed Particle Hydrodynamics simulations that uses a density-dependent pressurization of gas on small scales to ensure that the Jeans mass is properly resolved, similar to techniques used in grid-based simulations (e.g., Truelove et al. 1997; Machacek et al. 2001). The gas internal energy  $u$  at the Jeans scale is scaled as  $u \propto m_{\text{Jeans}}^{-2/3}$ , where  $m_{\text{Jeans}}$  is the local Jeans mass, to ensure the Jeans mass is resolved by some  $N_{\text{Jeans}}$  number of SPH kernel masses  $2N_{\text{neigh}}m_{\text{SPH}}$ , where  $N_{\text{neigh}}$  is the number of SPH neighbor particles and  $m_{\text{SPH}}$  is the gas particle mass. For the simulations presented here, we find the Bate & Burkert (1997) criterion of  $N_{\text{Jeans}} = 1$  to be insufficient to avoid numerical fragmentation and that  $N_{\text{Jeans}} \sim 15$  provides sufficient stability against numerical fragmentation over the time evolution of our simulations. Other simulations may have more stringent resolution requirements (e.g., Commercon et al. 2008). We also demonstrate that isothermal galactic disks with temperatures of  $T =$

$10^4$  K may be susceptible to numerical Jeans instabilities at resolutions common in cosmological simulations of disk galaxy formation, and connect this numerical effect to possible angular momentum deficiencies in cosmologically simulated disk galaxies.

The results of our study indicate that star formation may deviate significantly from the relations commonly assumed in models of galaxy formation in some regimes and that these deviations can be important for the overall galaxy evolution. Our findings provide strong motivation for exploring the consequences of such deviations and for developing further improvements in the treatment of star formation in galaxy formation simulations.

BER gratefully acknowledges support from a Spitzer Fellowship through a NASA grant administrated by the Spitzer Science Center. AVK is supported by the NSF grants AST-0239759, AST-0507596, AST-0708154 and by the Kavli Institute for Cosmological Physics at the University of Chicago. AVK thanks the Miller Institute and Astronomy department of UC Berkeley for hospitality during completion of this paper. We thank Andrew Baker, Leo Blitz, Bruce Elmegreen, Nick Gnedin, Dan Marrone, Chris McKee, Eve Ostriker, Erik Rosolowsky, and Konstantinos Tassis for helpful ideas, comments, and discussions. We also thank Gary Ferland and collaborators for developing and maintaining the Cloudy code used to tabulate cooling and heating rates and molecular fractions in our simulations, and Volker Springel for making his hydrodynamical simulation code GADGET2 available. Simulations presented here were performed at the `cobalt` system at the National Center for Supercomputing Applications (NCSA) under project TG-MCA05S017. We made extensive use of the NASA Astrophysics Data System and `arXiv.org` preprint server in this study.

#### REFERENCES

- Bate, M. R., & Burkert, A. 1997, MNRAS, 288, 1060  
 Beichman, C. A., Myers, P. C., Emerson, J. P., Harris, S., Mathieu, R., Benson, P. J., & Jennings, R. E. 1986, ApJ, 307, 337  
 Bell, E. F., & de Jong, R. S. 2001, ApJ, 550, 212  
 Binney, J., & Tremaine, S. 1987, Galactic dynamics (Princeton, NJ, Princeton University Press, 1987, 747 p.)  
 Blanton, M. R., et al. 2001, AJ, 121, 2358  
 Blanton, M. R., Eisenstein, D., Hogg, D. W., Schlegel, D. J., & Brinkmann, J. 2005, ApJ, 629, 143  
 Blanton, M. R., et al. 2003, ApJ, 592, 819  
 Blitz, L., & Rosolowsky, E. 2004, ApJ, 612, L29  
 —. 2006, ApJ, 650, 933  
 Blitz, L., & Thaddeus, P. 1980, ApJ, 241, 676  
 Blumenthal, G. R., Faber, S. M., Flores, R., & Primack, J. R. 1986, ApJ, 301, 27  
 Blumenthal, G. R., Faber, S. M., Primack, J. R., & Rees, M. J. 1984, Nature, 311, 517  
 Boissier, S., et al. 2007, ApJS, 173, 524  
 Boissier, S., Prantzos, N., Boselli, A., & Gavazzi, G. 2003, MNRAS, 346, 1215  
 Booth, C. M., Theuns, T., & Okamoto, T. 2007, MNRAS, 376, 1588  
 Brooks, A. M., Governato, F., Booth, C. M., Willman, B., Gardner, J. P., Wadsley, J., Stinson, G., & Quinn, T. 2007, ApJ, 655, L17  
 Calzetti, D., et al. 2007, ApJ, 666, 870  
 Carignan, C., & Beaulieu, S. 1989, ApJ, 347, 760  
 Commercon, B., Hennebelle, P., Audit, E., Chabrier, G., & Teyssier, R. 2008, A&A submitted (astro-ph/0801.3092)  
 Cooper, M. C., et al. 2007, MNRAS, 376, 1445  
 Corbelli, E. 2003, MNRAS, 342, 199  
 Das, M., O’Neil, K., Vogel, S. N., & McGaugh, S. 2006, ApJ, 651, 853  
 Dekel, A., & Birnboim, Y. 2006, MNRAS, 368, 2  
 —. 2008, MNRAS, 383, 119  
 Dobbs, C. L., & Bonnell, I. A. 2007, MNRAS, 376, 1747  
 Draine, B. T. 1978, ApJS, 36, 595  
 Draine, B. T., & Bertoldi, F. 1996, ApJ, 468, 269  
 Elmegreen, B. G. 1989, ApJ, 338, 178  
 Elmegreen, B. G. 1993a, in Star-Forming Galaxies and Their Interstellar Media, ed. J. Franco, F. Ferrini, & G. Tenorio-Tagle, 337  
 —. 1993b, ApJ, 411, 170  
 Elmegreen, B. G. 1997, in Revista Mexicana de Astronomia y Astrofisica Conference Series, ed. J. Franco, R. Terlevich, & A. Serrano, Vol. 6, 165  
 —. 2002, ApJ, 577, 206  
 Elmegreen, B. G., & Lada, C. J. 1977, ApJ, 214, 725  
 Elmegreen, B. G., & Parravano, A. 1994, ApJ, 435, L121+  
 Elmegreen, D. M., Elmegreen, B. G., Ravindranath, S., & Coe, D. A. 2007, ApJ, 658, 763  
 Ferland, G. J., Korista, K. T., Verner, D. A., Ferguson, J. W., Kingdon, J. B., & Verner, E. M. 1998, PASP, 110, 761  
 Ferland, G. J., & Mushotzky, R. F. 1984, ApJ, 286, 42  
 Freeman, K. C. 1970, ApJ, 160, 811  
 Gao, Y., & Solomon, P. M. 2004, ApJ, 606, 271  
 Gardan, E., Braine, J., Schuster, K. F., Brouillet, N., & Sievers, A. 2007, ArXiv e-prints, 707  
 Geha, M., Blanton, M. R., Masjedi, M., & West, A. A. 2006, ApJ, 653, 240  
 Giovanelli, R., & Haynes, M. P. 1983, AJ, 88, 881  
 Glover, S. C. O., & Mac Low, M.-M. 2007, ApJS, 169, 239  
 Gnedin, N. Y., Norman, M. L., & Ostriker, J. P. 2000, ApJ, 540, 32

- Gnedin, O. Y., Kravtsov, A. V., Klypin, A. A., & Nagai, D. 2004, *ApJ*, 616, 16
- Governato, F., Willman, B., Mayer, L., Brooks, A., Stinson, G., Valenzuela, O., Wadsley, J., & Quinn, T. 2007, *MNRAS*, 374, 1479
- Guhathakurta, P., van Gorkom, J. H., Kotanyi, C. G., & Balkowski, C. 1988, *AJ*, 96, 851
- Haardt, F., & Madau, P. 1996, *ApJ*, 461, 20
- Hernquist, L. 1990, *ApJ*, 356, 359
- Heyer, M. H., Corbelli, E., Schneider, S. E., & Young, J. S. 2004, *ApJ*, 602, 723
- Hippelein, H., Haas, M., Tuffs, R. J., Lemke, D., Stickel, M., Klaas, U., & Völk, H. J. 2003, *A&A*, 407, 137
- Hollenbach, D., & McKee, C. F. 1979, *ApJS*, 41, 555
- , 1989, *ApJ*, 342, 306
- Hopkins, A. M. 2004, *ApJ*, 615, 209
- Hopkins, A. M., & Beacom, J. F. 2006, *ApJ*, 651, 142
- Hultman, J., & Pharasyn, A. 1999, *A&A*, 347, 769
- Hunter, D. A., & Elmegreen, B. G. 2004, *AJ*, 128, 2170
- Hunter, D. A., Elmegreen, B. G., & Baker, A. L. 1998, *ApJ*, 493, 595
- Hunter, D. A., Elmegreen, B. G., & Martin, E. 2006, *AJ*, 132, 801
- Jeans, J. H. 1928, *Astronomy and cosmogony* (Cambridge [Eng.] The University press, 1928.)
- Jog, C. J., & Solomon, P. M. 1984, *ApJ*, 276, 114
- Joung, M. K. R., & Mac Low, M.-M. 2006, *ApJ*, 653, 1266
- Karachentsev, I. D., Karachentseva, V. E., Huchtmeier, W. K., & Makarov, D. I. 2004, *AJ*, 127, 2031
- Katz, N. 1992, *ApJ*, 391, 502
- Kauffmann, G., et al. 2003, *MNRAS*, 341, 54
- Kaufmann, T., Wheeler, C., & Bullock, J. S. 2007, *MNRAS*, 382, 1187
- Kenney, J. D. P., & Young, J. S. 1989, *ApJ*, 344, 171
- Kennicutt, R. C. 1989, *ApJ*, 344, 685
- , 1998, *ApJ*, 498, 541
- Kennicutt, Jr., R. C., et al. 2007, *ApJ*, 671, 333
- Kim, W.-T., Ostriker, E. C., & Stone, J. M. 2002, *ApJ*, 581, 1080
- Klein, R. I., Fisher, R., & McKee, C. F. 2004, in *Revista Mexicana de Astronomia y Astrofisica Conference Series*, Vol. 22, *Revista Mexicana de Astronomia y Astrofisica Conference Series*, ed. G. Garcia-Segura, G. Tenorio-Tagle, J. Franco, & H. W. Yorke, 3–7
- Kravtsov, A. V. 2003, *ApJ*, 590, L1
- Kravtsov, A. V., Berlind, A. A., Wechsler, R. H., Klypin, A. A., Gottlöber, S., Allgood, B., & Primack, J. R. 2004, *ApJ*, 609, 35
- Kravtsov, A. V., & Gnedin, O. Y. 2005, *ApJ*, 623, 650
- Kroupa, P. 1995, *MNRAS*, 277, 1522
- Krumholz, M. R., & McKee, C. F. 2005, *ApJ*, 630, 250
- Krumholz, M. R., & Tan, J. C. 2007, *ApJ*, 654, 304
- Krumholz, M. R., & Thompson, T. A. 2007, *ApJ*, 669, 289
- Lada, C. J. 1987, in *IAU Symposium*, Vol. 115, *Star Forming Regions*, ed. M. Peimbert & J. Jugaku, 1–17
- Lee, H., Skillman, E. D., Cannon, J. M., Jackson, D. C., Gehrz, R. D., Polomski, E. F., & Woodward, C. E. 2006, *ApJ*, 647, 970
- Leroy, A., Bolatto, A., Walter, F., & Blitz, L. 2006, *ApJ*, 643, 825
- Leroy, A., Bolatto, A. D., Simon, J. D., & Blitz, L. 2005, *ApJ*, 625, 763
- Li, Y., Mac Low, M.-M., & Klessen, R. S. 2005a, *ApJ*, 620, L19
- , 2005b, *ApJ*, 626, 823
- , 2006, *ApJ*, 639, 879
- Luna, A., Bronfman, L., Carrasco, L., & May, J. 2006, *ApJ*, 641, 938
- Machacek, M. E., Bryan, G. L., & Abel, T. 2001, *ApJ*, 548, 509
- Martin, C. L., & Kennicutt, R. C. 2001, *ApJ*, 555, 301
- Mathis, J. S., Mezger, P. G., & Panagia, N. 1983, *A&A*, 128, 212
- Matthews, L. D., Gao, Y., Uson, J. M., & Combes, F. 2005, *AJ*, 129, 1849
- McGaugh, S. S. 2005, *ApJ*, 632, 859
- McKee, C. F., & Ostriker, E. C. 2007, *ARA&A*, 45, 565
- Miller, G. E., & Scalo, J. M. 1979, *ApJS*, 41, 513
- Misiriotis, A., Xilouris, E. M., Papamastorakis, J., Boumis, P., & Goudis, C. D. 2006, *A&A*, 459, 113
- Mo, H. J., Mao, S., & White, S. D. M. 1998, *MNRAS*, 295, 319
- Möllenhoff, C., & Heidt, J. 2001, *A&A*, 368, 16
- Murgia, M., Crapsi, A., Moscadelli, L., & Gregorini, L. 2002, *A&A*, 385, 412
- Navarro, J. F., Frenk, C. S., & White, S. D. M. 1996, *ApJ*, 462, 563
- , 1997, *ApJ*, 490, 493
- Nieten, C., Neininger, N., Guélin, M., Ungerechts, H., Lucas, R., Berkhuijsen, E. M., Beck, R., & Wielebinski, R. 2006, *A&A*, 453, 459
- Padoan, P., Nordlund, A., & Jones, B. J. T. 1997, *MNRAS*, 288, 145
- Passot, T., & Vázquez-Semadeni, E. 1998, *Phys. Rev. E*, 58, 4501
- Pelupessy, F. I., Papadopoulos, P. P., & van der Werf, P. 2006, *ApJ*, 645, 1024
- Press, W. H., & Schechter, P. 1974, *ApJ*, 187, 425
- Press, W. H., Teukolsky, S. A., Vetterling, W. T., & Flannery, B. P. 1992, *Numerical recipes in C. The art of scientific computing* (Cambridge: University Press, [c]1992, 2nd ed.)
- Rafikov, R. R. 2001, *MNRAS*, 323, 445
- Rana, N. C. 1987, *A&A*, 184, 104
- , 1991, *ARA&A*, 29, 129
- Robertson, B., Bullock, J. S., Cox, T. J., Di Matteo, T., Hernquist, L., Springel, V., & Yoshida, N. 2006a, *ApJ*, 645, 986
- Robertson, B., Cox, T. J., Hernquist, L., Franx, M., Hopkins, P. F., Martini, P., & Springel, V. 2006b, *ApJ*, 641, 21
- Robertson, B., Hernquist, L., Cox, T. J., Di Matteo, T., Hopkins, P. F., Martini, P., & Springel, V. 2006c, *ApJ*, 641, 90
- Robertson, B., Yoshida, N., Springel, V., & Hernquist, L. 2004, *ApJ*, 606, 32
- Rosenberg, J. L., & Schneider, S. E. 2002, *ApJ*, 567, 247
- Rubin, V. C., Waterman, A. H., & Kenney, J. D. P. 1999, *AJ*, 118, 236
- Safronov, V. S. 1960, *Annales d'Astrophysique*, 23, 979
- Salpeter, E. E. 1955, *ApJ*, 121, 161
- Scalo, J., Vázquez-Semadeni, E., Chappell, D., & Passot, T. 1998, *ApJ*, 504, 835
- Schaye, J. 2004, *ApJ*, 609, 667
- Schaye, J., & Dalla Vecchia, C. 2008, *MNRAS* in press (astro-ph/0709.0292)
- Schmidt, M. 1959, *ApJ*, 129, 243
- Schuster, K. F., Kramer, C., Hirschfeld, M., Garcia-Burillo, S., & Mookerjee, B. 2007, *A&A*, 461, 143
- Sheth, R. K., & Tormen, G. 1999, *MNRAS*, 308, 119
- Sijacki, D., Springel, V., di Matteo, T., & Hernquist, L. 2007, *MNRAS*, 380, 877
- Silk, J. 1997, *ApJ*, 481, 703
- Smith, L. F., Mezger, P. G., & Biermann, P. 1978, *A&A*, 66, 65
- Springel, V. 2000, *MNRAS*, 312, 859
- , 2005, *MNRAS*, 364, 1105
- Springel, V., Di Matteo, T., & Hernquist, L. 2005, *MNRAS*, 361, 776
- Springel, V., & Hernquist, L. 2003a, *MNRAS*, 339, 289
- , 2003b, *MNRAS*, 339, 312
- Springel, V., Yoshida, N., & White, S. D. M. 2001, *New Astronomy*, 6, 79
- Stecher, T. P., & Williams, D. A. 1967, *ApJ*, 149, L29+
- Steinmetz, M., & Müller, E. 1995, *MNRAS*, 276, 549
- Sternberg, A., McKee, C. F., & Wolfire, M. G. 2002, *ApJS*, 143, 419
- Stinson, G., Seth, A., Katz, N., Wadsley, J., Governato, F., & Quinn, T. 2006, *MNRAS*, 373, 1074
- Talbot, Jr., R. J. 1980, *ApJ*, 235, 821
- Tan, J. C. 2000, *ApJ*, 536, 173
- Tasker, E. J., & Bryan, G. L. 2006, *ApJ*, 641, 878
- , 2007, *ApJ* submitted (astro-ph/0709.1972), 709
- Tassis, K. 2007, *MNRAS*, 382, 1317
- Tassis, K., Kravtsov, A. V., & Gnedin, N. Y. 2008, *ApJ*, 672, 888
- Thacker, R. J., & Couchman, H. M. P. 2000, *ApJ*, 545, 728
- Toomre, A. 1964, *ApJ*, 139, 1217
- Truelove, J. K., Klein, R. I., McKee, C. F., Holliman, II, J. H., Howell, L. H., & Greenough, J. A. 1997, *ApJ*, 489, L179+
- Tully, R. B., & Fisher, J. R. 1977, *A&A*, 54, 661
- van Hoof, P. A. M., Weingartner, J. C., Martin, P. G., Volk, K., & Ferland, G. J. 2001, in *Astronomical Society of the Pacific Conference Series*, Vol. 247, *Spectroscopic Challenges of Photoionized Plasmas*, ed. G. Ferland & D. W. Savin, 363+
- Vorobyov, E. I. 2003, *A&A*, 407, 913
- Wada, K. 2007, *ArXiv e-prints*, 710
- Wada, K., & Norman, C. A. 2001, *ApJ*, 547, 172
- , 2007, *ApJ*, 660, 276
- Weingartner, J. C., & Draine, B. T. 2001, *ApJS*, 134, 263
- White, S. D. M., & Frenk, C. S. 1991, *ApJ*, 379, 52
- White, S. D. M., & Rees, M. J. 1978, *MNRAS*, 183, 341
- Wild, V., Hewett, P. C., & Pettini, M. 2007, *MNRAS*, 374, 292
- Wolfe, A. M., & Chen, H.-W. 2006, *ApJ*, 652, 981
- Wolfire, M. G., McKee, C. F., Hollenbach, D., & Tielens, A. G. G. M. 2003, *ApJ*, 587, 278
- Wong, T., & Blitz, L. 2002, *ApJ*, 569, 157
- Wu, J., Evans, II, N. J., Gao, Y., Solomon, P. M., Shirley, Y. L., & Vanden Bout, P. A. 2005, *ApJ*, 635, L173
- Wyse, R. F. G. 1986, *ApJ*, 311, L41
- Wyse, R. F. G., & Silk, J. 1989, *ApJ*, 339, 700
- Yang, C.-C., Gruendl, R. A., Chu, Y.-H., Mac Low, M.-M., & Fukui, Y. 2007, *ApJ*, 671, 374
- Yepes, G., Kates, R., Khokhlov, A., & Klypin, A. 1997, *MNRAS*, 284, 235
- Young, J. S., & Scoville, N. Z. 1991, *ARA&A*, 29, 581
- Zwaan, M. A., & Prochaska, J. X. 2006, *ApJ*, 643, 675
- Zwaan, M. A., Staveley-Smith, L., Koribalski, B. S., & et al. 2003, *AJ*, 125, 2842



## APPENDIX

Truelove et al. (1997) showed that hydrodynamical calculations that do not properly resolve pressure forces on scales where self-gravity begins to dominate over gaseous pressure support are susceptible to a numerical instability that leads to the rapid artificial fragmentation of gas. Truelove et al. (1997) suggest a constraint on the spatial resolution of hydrodynamical mesh calculations such that the Jeans length  $\lambda_{\text{Jeans}}$  is locally larger than the grid resolution  $\Delta x$ . This resolution requirement for grid codes can be expressed in terms of a constraint on the “Jeans number”  $J = \Delta x / \lambda_{\text{Jeans}} < 0.25$  to properly resolve the Jeans scale and prevent such artificial fragmentation.

Similarly, the inability of SPH codes to capture pressure forces properly on scales less than the smoothing length can also allow for numerically-induced fragmentation if the smoothing length is of order the Jeans length (Bate & Burkert 1997). As discussed by Bate & Burkert (1997) and in §2.3, the requirement that the Jeans scale is resolved an SPH calculation by some number  $N_{\text{Jeans}}$  of SPH kernels is  $2N_{\text{Jeans}}N_{\text{neigh}}m_{\text{gas}} < m_{\text{Jeans}}$ , where  $m_{\text{gas}}$  is the SPH particle mass and  $N_{\text{neigh}}$  is the number of SPH neighbors. A similar requirement can be formulated in terms of relevant spatial scales (e.g., Klein et al. 2004). Owing to the temperature dependence of the sound speed ( $c_s \propto \sqrt{T}$  for ideal gas) and the dependence of the Jeans scale on density and temperature, it is clear that for a given number of gas particles  $N_{\text{gas}}$  used in an SPH calculation, the lower the temperature floor allowed the more potentially susceptible the simulated fluid will be to numerical Jeans fragmentation.

Simulations of the ISM in galaxies with molecular coolants must be especially cautious given the typical numerical resolutions, high densities, and potentially low temperatures. For example, for the typical conditions of the average ISM in a Milky Way-size galaxies (number density of  $n_{\text{H}} = 1 \text{ cm}^{-3}$ , sound speed  $c_s = 10 \text{ km s}^{-1}$ ), the Jeans mass is  $m_{\text{Jeans}} \sim 6.5 \times 10^7 M_{\odot}$ , which is comparable to or smaller than the gas mass resolution in many recent simulations of disk galaxy formation. However, for molecular gas ( $n_{\text{H}} \gtrsim 100 \text{ cm}^{-3}$ ) with a sound speed  $c_s = 1 \text{ km s}^{-1}$  (corresponding to the temperature  $T = 100 \text{ K}$ ), the Jeans mass would be only  $m_{\text{Jeans}} \sim 6.5 \times 10^3 M_{\odot}$  — far smaller than the gas mass resolution of the largest MW-sized galaxy formation simulations performed to date.

For SPH calculations in the literature, typical approaches for addressing numerical Jeans instability include improving the numerical resolution such that the Jeans scale is resolved with  $N_{\text{Jeans}} = 1$ , as suggested by Bate & Burkert (1997), or using sink particles to represent high density regions of the ISM (e.g. Li et al. 2005b, 2006; Booth et al. 2007). Each of these approaches have possible drawbacks, as the Bate & Burkert (1997) resolution criterion can clearly depend on the density, depending on the gas equation-of-state, and the sink particle method, depending on its implementation, may neither avoid numerical fragmentation nor properly capture the complicated chemical, thermodynamical, and radiative processes that operate in dense ISM gas (see, e.g., Commercon et al. 2008). Another possible solution is to use a stiffer equation-of-state for the gas (e.g., Springel et al. 2005; Schaye & Dalla Vecchia 2008).

Instead, the simulations presented in this paper adopt a pressure floor on the scale of the Jeans length through an approach similar to that implemented by Machacek et al. (2001) in grid codes. Machacek et al. (2001) adopt an effective pressure  $P_{\text{eff}}$  on the scale of the finest grid resolution  $\Delta x$ , given by

$$P_{\text{eff}} = KG\rho_b^2\Delta x^2/\mu \quad (1)$$

where  $\rho_b$  is the baryon density in the cell,  $\mu$  is the mean molecular mass,  $G$  is the gravitational constant, and  $K \approx 100$  is a parameter that sets the effective resolution of their simulations. If the effective pressure  $P \propto \rho u$  on the scale of the SPH kernel is set to ensure the Jeans scale is over-resolved by a factor  $N_{\text{Jeans}}$ , then the internal energy of gas particles with kernel mass  $m_{\text{SPH}} \sim N_{\text{neigh}}m_{\text{gas}}$  should be scaled as

$$u = u \times \begin{cases} \left(\frac{N_{\text{Jeans}}}{h_{\text{Jeans}}}\right)^{2/3} & : h_{\text{Jeans}} < N_{\text{Jeans}} \\ \left(\frac{2N_{\text{Jeans}}m_{\text{SPH}}}{m_{\text{Jeans}}}\right)^{2/3} & : m_{\text{Jeans}} < 2N_{\text{Jeans}}m_{\text{SPH}} \end{cases}, \quad (2)$$

which is Equation 10 from §2.3. A factor  $N_{\text{Jeans}} = 1$  would correspond to a density-dependent version of the Bate & Burkert (1997) criterion, while applying the effective pressure of Machacek et al. (2001) with  $K \sim 100$  and equating  $\Delta x \sim h$  would imply  $N_{\text{Jeans}} \gtrsim 1000$ . Klein et al. (2004) provide a survey of the literature and find that values of  $N_{\text{Jeans}} \sim 0.4 - 30$  for a fixed maximum density are in common usage.

As briefly mentioned in §2.3, we have performed a variety of resolution studies where we examine the range of  $N_{\text{Jeans}} = 1 - 100$  and found  $N_{\text{Jeans}} \approx 15$  to provide sufficient stability for the time interval in our simulations. Note, however, that more stringent criteria are likely to be required for longer periods of evolution for galaxies in cosmological simulations. The resolution studies utilized a galaxy model initialized with a virial velocity  $V_{\text{vir}} = 160 \text{ km s}^{-1}$ , spin  $\lambda = 0.033$ , NFW concentration  $c = 9$ , disk mass fraction  $m_{\text{d}} = 0.05$ , bulge mass fraction  $m_{\text{b}} = 0.0167$ , and disk gas fraction  $f_{\text{gas}} = 0.2$  according to the method described in §2.6. The dark matter halo, bulge, stellar disk, and gaseous disk were resolved with  $N_{\text{DM}} = 120,000$ ,  $N_{\text{b}} = 40,000$ ,  $N_{\text{d}} = 128,000$ , and  $N_{\text{g}} = 400,000$  particles respectively, and the halo and baryonic particle gravitational softenings were set to  $\epsilon_{\text{DM}} = 100h^{-1} \text{ pc}$  and  $\epsilon_{\text{b}} = 50h^{-1} \text{ pc}$ . The mass contained within the SPH kernel with  $N_{\text{neigh}} = 64$  for this galaxy model was typically  $m_{\text{SPH}} = 2 \times 10^6 M_{\odot}$ . The galaxy model was evolved with two ISM models, the atomic cooling treatment with a temperature floor of  $T = 10^4 \text{ K}$  (the GD-SF model) and the atomic and molecular cooling treatment with a temperature floor of  $T = 10^2 \text{ K}$  (the H<sub>2</sub>D-SF model). Figure 14 shows the disk galaxy evolved with a density-dependent pressure floor described by Equation 10 with  $N_{\text{Jeans}} = 15$  (upper row) and without a pressure floor (lower row) evolved in isolation for  $t = 0.2 \text{ Gyr}$ . The systems without a pressure floor quickly fragment if the effective temperature floor is either  $T = 10^2 \text{ K}$  (lower middle panel) or  $T = 10^4 \text{ K}$  (lower left panel), as the Jeans mass is initially not resolved at the highest gas densities for either temperature. By design, the simulations that include the suggested pressure floor do not fragment on the Jeans scale (upper row). The pressurization on the Jeans scale used to ameliorate

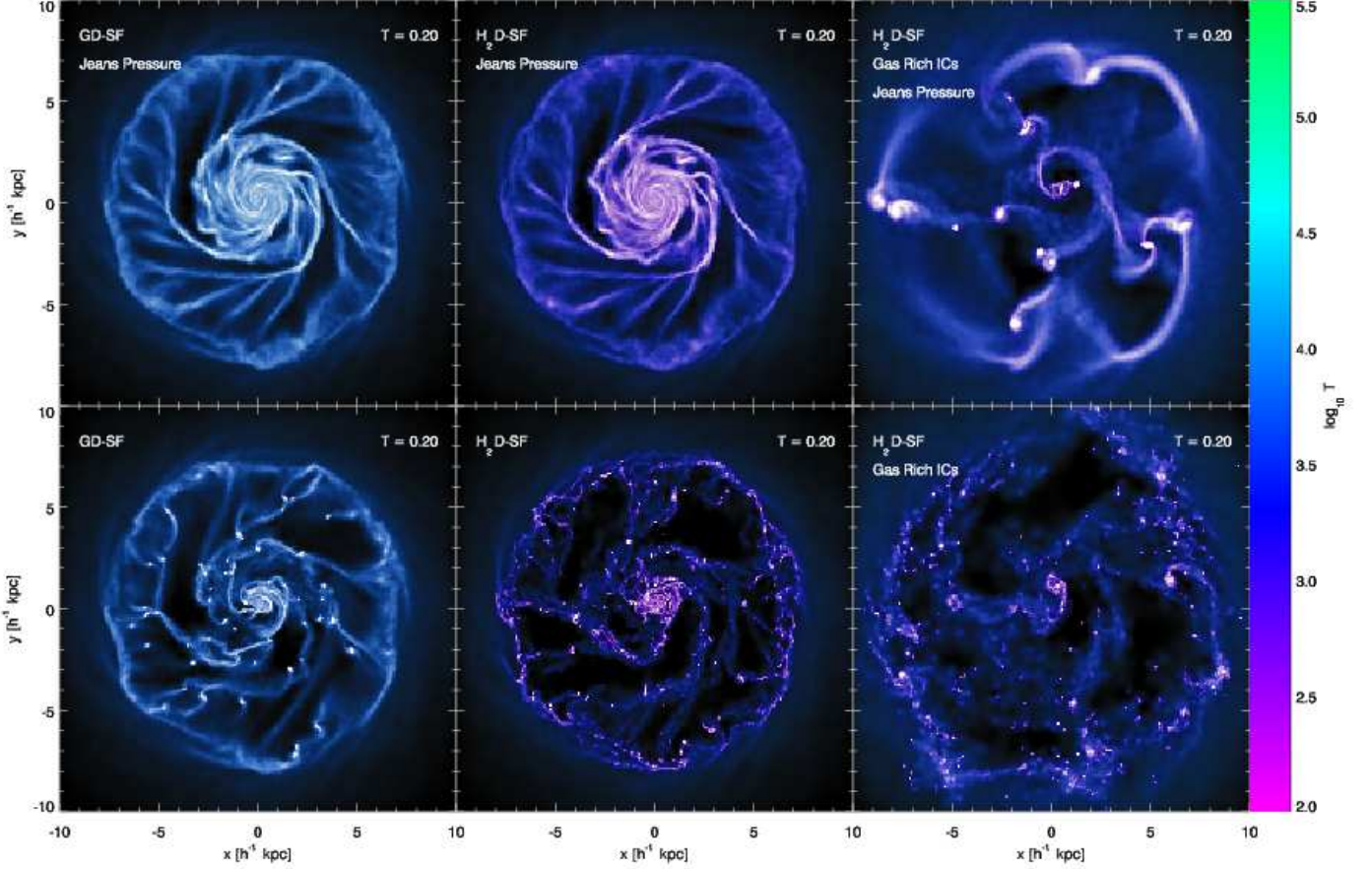


FIG. 14.— Results of simulations of an isolated galaxy model with a circular velocity of  $v_{\text{circ}} = 160 \text{ km s}^{-1}$  evolved with (upper row) and without (lower row) a pressure floor to resolve the local Jeans mass and length. The image intensity tracks the surface density while the color reflects the gas effective temperature. For galaxy systems of this mass and disk structure with gas fractions of  $f_{\text{gas}} = 0.2$  and simulated with  $N = 400,000$  gas particles, the local Jeans mass in dense regions is smaller than the typical mass in an SPH kernel if ISM is modeled with either atomic cooling and a  $T = 10^4 \text{ K}$  temperature floor (lower left panel) or atomic and molecular cooling with a  $T = 10^2 \text{ K}$  temperature floor (lower middle panel). These systems are susceptible to numerical fragmentation since, owing to the limited resolution, the local gas pressure is artificially low on the scale where the gas is marginally stable against collapse through self-gravity (Truelove et al. 1997). To avoid this numerical artificiality, a pressure-floor is introduced to increase the local sound speed until the Jeans scale is resolved by several SPH kernels. Our prescription allows for galaxy models with either atomic cooling at temperatures  $T > 10^4 \text{ K}$  (upper left panel) or atomic and molecular cooling at temperatures  $T > 10^2 \text{ K}$  (upper middle panel) to be evolved stably. Systems that are extremely gas-rich (e.g.,  $f_{\text{gas}} = 0.99$ , right panels) can still become globally unstable and undergo large scale fragmentation if a pressure floor is used (upper right panel), but fragmentation occurs at much smaller scales and is qualitatively different without such preventative measures (lower right panel).

artificial fragmentation does not insure that simulated disks will avoid other instabilities, such as global Toomre (1964) instability. The right panels of Figure 14 show the  $V_{\text{vir}} = 160 \text{ km s}^{-1}$  disk model with the disk gas fraction increased to  $f_{\text{gas}} = 0.99$ , evolved for  $t = 0.2 \text{ Gyr}$  in isolation. The gas rich model simulated without a pressure floor violently fragments, but the gas rich model evolved using a pressure floor also undergoes fragmentation on a much larger mass scale. As discussed in Springel & Hernquist (2003a), Robertson et al. (2004) and Springel et al. (2005), systems like this gas rich model that are violently Toomre-unstable when using an ideal gas or weakly pressurized equation-of-state can be stabilized by adopting a more strongly pressurized ISM equation-of-state, but we do not examine such models here.

Separating artificial fragmentation and physical Jeans fragmentation owing to self-gravity may be difficult without detailed resolution studies that examine the convergence of the growth rate of perturbations on different size scales. For Galaxy-mass systems with the disk structure we utilize and gas fractions of  $f_{\text{gas}} = 0.2$  simulated with  $N = 400,000$  gas particles, the local Jeans mass in dense regions is smaller than the typical mass in an SPH kernel if either an ISM model with atomic cooling and a  $T = 10^4 \text{ K}$  temperature floor or (the GD-SF model) or an ISM model with atomic + molecular cooling and a  $T = 10^2 \text{ K}$  temperature floor (the H<sub>2</sub>D-SF model) is used, by a factor of  $m_{\text{Jeans}}/2N_{\text{Jeans}}m_{\text{SPH}} \sim 100$  for a  $T = 10^4 \text{ K}$  temperature floor or  $m_{\text{Jeans}}/2N_{\text{Jeans}}m_{\text{SPH}} > 10,000$  for a  $T = 10^2 \text{ K}$  temperature floor. The simulations that include a pressure floor maintain  $m_{\text{Jeans}}/2N_{\text{Jeans}}m_{\text{SPH}} \approx 1$  by design, with a small scatter induced by fluctuations in  $m_{\text{SPH}}$  from changing particle masses from star formation and the small allowed range of neighbors  $N_{\text{neigh}} = 62 - 66$ . Given the values of the Jeans mass for the typical densities and temperatures of the ISM ( $m_{\text{Jeans}} \sim 10^3 - 10^7 M_{\odot}$ , see above), our calculations thus suggest that simulating molecular cooling in Milky Way-sized disks of  $M_{\text{gas}} \approx 10^{10} M_{\odot}$  with SPH *without* using an artificial pressure floor would require  $N \sim 10^9 - 10^{10}$  gas particles to avoid numerical Jeans fragmentation if gas is allowed to cool to 100 K. We delay such resolution studies for future work (and faster computers).

Artificial fragmentation of the ISM in disks may be closely related to the angular momentum problem for producing realistic disk galaxies in cosmological simulations (see, e.g., §6 of Robertson et al. (2004) and Robertson et al. (2006a)). The simulations of a Milky Way analogue galaxy model presented in this appendix contain  $N_{\text{gas}} = 400,000$ , which exceeds the numerical resolution of many disk galaxies formed in cosmological simulations to date. Both Truelove et al. (1997) and Bate & Burkert (1997) comment on the possible implications of numerical Jeans fragmentation for studies of galaxy formation; based on these test simulations we suggest that to reliably follow the formation and evolution of disks using SPH simulations a pressure floor similar to our Equation 10 should be used. Prescriptions that mimic pressurization from the multiphase structure of the ISM that may develop through feedback from star formation (e.g., Yepes et al. 1997; Hultman & Pharasyn 1999; Springel 2000; Thacker & Couchman 2000; Springel & Hernquist 2003a; Stinson et al. 2006; Schaye & Dalla Vecchia 2008) may also serve to ameliorate numerical Jeans fragmentation by raising the sound speed as a function of the mean ISM density. This affect is apparent in numerical tests examining the stability of isolated disks by Springel et al. (2005) using various ISM equations-of-state. We plan to revisit the implications of numerical Jeans fragmentation on cosmological simulations of galaxy formation in future work. Lastly, we note that since disks that are Toomre-unstable are also roughly Jeans-unstable (see, e.g., Krumholz & McKee 2005), numerical Jeans fragmentation will artificially reinforce any natural correspondence between gravitational instability and star formation. Simulations that examine the relation between star formation and the Toomre instability parameter  $Q_{\text{sg}}$  should therefore explicitly demonstrate that the Jeans scale is properly resolved at all densities.

## APPENDIX

As discussed in §3.4, the simulated galaxies display a correlation between the SFR surface density  $\Sigma_{\text{SFR}}$  and the product of the total gas surface mass density  $\Sigma_{\text{gas}}$  and the angular frequency  $\Omega$  in regions where the molecular gas and total gas densities are comparable. The correlation in our simulations is similar to the observed  $\Sigma_{\text{SFR}} - \Sigma_{\text{gas}}\Omega$  correlation (e.g., Kennicutt 1998; Kennicutt et al. 2007). Since the star formation relation implemented in the simulations calculates the SFR density  $\dot{\rho}_*$  as proportional to the product of the molecular fraction  $f_{\text{H}_2}$  and the gas density scaled with the local dynamical time  $\rho_g^{1.5}$  (Equation 4), the  $\Sigma_{\text{SFR}} - \Sigma_{\text{gas}}\Omega$  correlation would occur if the angular frequency scaled with the density as  $\Omega \propto \sqrt{\rho_g}$ . Given that the gas density is a local quantity while orbital frequency is determined by the overall mass distribution and potential of the galaxy, it is not immediately clear why such a relation should hold. Here we show that the relation between  $\rho_g$  and  $\Omega$  with a similar scaling exists for self-gravitating exponential disks or exponential disks embedded in realistic dark matter potentials.

Given the axisymmetry of the disk galaxy models, the angular frequency is related to the density through Poisson's equation

$$\frac{d^2\Phi}{dz^2} + \frac{d^2\Phi}{dR^2} + \Omega^2 = 4\pi G\rho_{\text{total}}. \quad (1)$$

(Equation 26 in §3.4). Below, the scaling of the angular frequency  $\Omega$  with the local disk density  $\rho_{\text{disk}}$  is calculated in the limiting cases of potentials dominated by disks ( $\rho_{\text{total}} \approx \rho_{\text{disk}}$ ) or dark matter halos ( $\rho_{\text{total}} \approx \rho_{\text{DM}}$ ) for exponential disks ( $\rho_{\text{disk}} \propto \exp[-R/R_d]$ ), and we show that for the examined cases  $\Omega \propto \sqrt{\rho_{\text{disk}}B(R/R_d)}$ , where  $B(R/R_d) \sim \mathcal{O}(1)$  is a weak function of the disk radius  $R$  that depends on the form of the dominate potential.

*Exponential Disk-Dominated Potentials,  $\rho_{\text{disk}} \gg \rho_{\text{DM}}$* 

For a flattened system, Binney & Tremaine (1987) recognized that as the vertical scale  $h$  of the density distribution decreases the first term on the left hand side of Equation 26 begins to dominate and eventually

$$\frac{d^2\Phi}{dz^2} \simeq 4\pi G\rho. \quad (2)$$

If the surface density of the disk is exponential, the axisymmetric density distribution of the disk can be written as

$$\rho_d(R, z) = \frac{A\Sigma_0}{R_d} \exp(-R/R_d)f(z) \quad (3)$$

where  $f(z) \propto \text{sech}^2(z)$  is determined by Equation 2, and the constant  $A$  is determined by taking  $f(0) = 1$  and the integral constraint from the disk mass. Using the methods of §2.6.3 of Binney & Tremaine (1987), one can show that the rotation curve in the plane of a very thin exponential disk is

$$v_c^2(R) = 4\pi G\Sigma_0 R_d y^2 [I_0(y)K_0(y) - I_1(y)K_1(y)], \quad (4)$$

where  $y \equiv R/R_d$  (Freeman 1970). Substituting for  $\Sigma_0/R_d$  from Equation 3, as is appropriate if the gas densities in the disk plane decrease in proportion to the surface density, we find

$$\begin{aligned} \Omega_{\text{disk}}(R) &= \{4\pi GA^{-1}\rho_d(R, z)\exp(y) \times [I_0(y)K_0(y) - I_1(y)K_1(y)]\}^{1/2} \\ &= \sqrt{\rho_d}B_{\text{disk}}(R/R_d). \end{aligned} \quad (5)$$

The function  $B_{\text{disk}}(x)$  is a weak function of the disk surface density  $\Sigma(R)$ . Over the inner 95% of the disk mass ( $x \simeq \{0.355, 4.75\}$ ), the fractional deviation from the  $\Omega \propto \sqrt{\rho_d}$  correlation, normalized to the disk properties at one scale length, is only  $B(0.355)/B(1) - 1 = 0.48$  near the disk center and  $B(4.75)/B(1) - 1 = -0.26$  in the disk exterior.

*Halo-Dominated Potentials*,  $\rho_{\text{DM}} \gg \rho_{\text{disk}}$

In the case of  $\rho_{\text{total}} \approx \rho_{\text{DM}}$ , the angular frequency can be determined directly from the integrated mass  $M$  within a radius  $R$  as

$$\Omega^2 = \frac{GM(< R)}{R^3}. \quad (7)$$

There are a wide variety of possible dark matter halo profiles, but we limit ourselves to three salient models.

Dark matter halos in cosmological simulations on average follow the Navarro et al. (1996) (NFW) dark matter halo profile, given by

$$\rho_{\text{DM}}(R, z) = \frac{4\rho_s}{(\sqrt{R^2 + z^2}/r_s)(1 + \sqrt{R^2 + z^2}/r_s)^2}, \quad (8)$$

where  $\rho_s$  is the density at the scale radius  $r_s$ . If we substitute for the disk density

$$\rho_s = f_d^{-1} \rho_d(R, z) \exp(R/R_d - r_s/R_d), \quad (9)$$

then the angular frequency in the disk plane of a NFW profile can be written

$$\Omega_{\text{NFW}}(R) = \sqrt{\rho_d} B_{\text{NFW}}(R/r_s), \quad (10)$$

where the function

$$B_{\text{NFW}}(x) = \left\{ 16\pi G f_d^{-1} \exp\left(\frac{r_s(x-1)}{R_d}\right) \left[ \frac{(1+x)\ln(1+x) - x}{x^3(1+x)} \right] \right\}^{1/2} \quad (11)$$

is, again, a weak function of the disk surface density  $\Sigma(R)$ . Over the inner 95% of the disk mass, the fractional deviation from the  $\Omega \propto \sqrt{\rho_d}$  correlation, normalized to the disk properties at one scale length, is only  $B_{\text{NFW}}(0.355R_d/r_s)/B_{\text{NFW}}(R_d/r_s) - 1 = 0.27$  near the disk center and  $B_{\text{NFW}}(4.75R_d/r_s)/B_{\text{NFW}}(R_d/r_s) - 1 = 1.45$  in the disk exterior.

Alternatively, we can consider the Hernquist (1990) profile

$$\rho_{\text{H}}(R, z) = \frac{8\rho_a}{(\sqrt{R^2 + z^2}/a)(1 + \sqrt{R^2 + z^2}/a)^3}, \quad (12)$$

where  $\rho_a$  is the density at a scale radius  $a$ . The Hernquist (1990) profile is used as the DM halo profile in the galaxy models presented in this paper and has a density and potential similar to the NFW profile within the scale radius. Substituting for the disk density, we can write

$$\rho_a = f_d^{-1} \rho_d(R, z) \exp(R/R_d - a/R_d). \quad (13)$$

The mass profile of the Hernquist (1990) halo provides

$$\Omega_{\text{H}}(R) = \sqrt{\rho_d} B_{\text{H}}(R/a) \quad (14)$$

where the function

$$B_{\text{H}}(x) = \left\{ 32\pi G f_d^{-1} \exp\left[\frac{a(x-1)}{R_d}\right] \left[ \frac{1}{x(1+x)^2} \right] \right\}^{1/2} \quad (15)$$

has a scaling nearly identical to the function  $B_{\text{NFW}}(x)$  when  $x \ll 1$ , and is a correspondingly weak function of the disk surface density  $\Sigma(R)$ . Over the inner 95% of the disk mass, the fractional deviation from the  $\Omega \propto \sqrt{\rho_d}$  correlation, normalized to the disk properties at one scale length, is only  $B_{\text{H}}(0.355R_d/a)/B_{\text{H}}(R_d/a) - 1 = 0.26$  near the disk center and  $B_{\text{H}}(4.75R_d/a)/B_{\text{H}}(R_d/a) - 1 = 1.48$  in the disk exterior.

In real galaxies, it is thought that the dark matter halo will adiabatically compress in response to the dissipational formation of the disk (e.g., Blumenthal et al. 1986). Models of adiabatic compression suggest that the dark matter halo response tends to drive the halo profile to resemble an isothermal sphere over much of the disk (Gnedin et al. 2004). The isothermal density profile can be written

$$\rho_{\text{iso}}(R, z) = \frac{\rho_0}{(\sqrt{R^2 + z^2}/r_0)^2}, \quad (16)$$

where  $\rho_0$  is the density at an arbitrary scale radius  $r_0$ . For simplicity, we set  $r_0 = R_d$  and substitute for the disk density as

$$\rho_0 = f_d^{-1} \rho_d(R, 0) \exp(R/R_d - 1). \quad (17)$$

Integrating the isothermal density profile to find the enclosed mass provides the angular frequency in the disk plane as

$$\Omega_{\text{iso}}(R) = \sqrt{\rho_d} B_{\text{iso}}(R/R_d) \quad (18)$$

where

$$B_{\text{iso}}(x) = \{4\pi G f_d^{-1} x^{-2} \exp(x-1)\}^{1/2}. \quad (19)$$

The function  $B_{\text{iso}}(x)$  is also weak function of the disk surface density  $\Sigma(R)$ , and is of the same order as  $B_{\text{NFW}}$  or  $B_{\text{H}}$ . Over the inner 95% of the disk mass, the fractional deviation from the  $\Omega \propto \sqrt{\rho_d}$  correlation, normalized to the disk properties at one scale length, is only  $B_{\text{iso}}(0.355)/B_{\text{iso}}(1) - 1 = 1.04$  near the disk center and  $B_{\text{iso}}(4.75)/B_{\text{iso}}(1) - 1 = 0.37$  in the disk exterior.

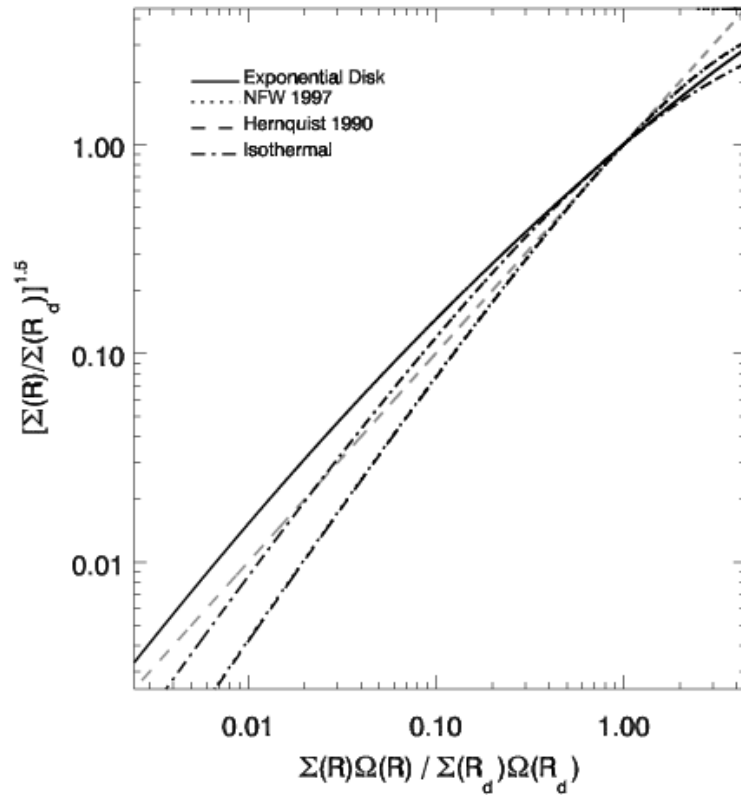


FIG. 15.— Relation between surface density  $\Sigma$  and angular frequency  $\Omega$  for a variety of disk galaxy model potentials. Shown is the quantity  $\Sigma^{1.5} \propto \Sigma_{\text{SFR}}$  plotted against the product  $\Sigma\Omega$  for exponential disks in a disk-dominated (solid line), Navarro et al. (1997) halo-dominated (dotted line), Hernquist (1990) halo-dominated (dashed line), or isothermal halo-dominated (dash-dotted line) potential, normalized to the disk properties at an exponential scale length. Deviations from the  $\Sigma^{1.5} \propto \Sigma\Omega$  correlation (indicated with a dashed grey line) are typically  $\sim \mathcal{O}(1)$  and are largest in the very center and exterior of the disk. The calculation suggests that the  $\Sigma_{\text{SFR}} \propto \Sigma\Omega$  may reflect the scaling of the local density in exponential gas disks with the characteristic shape of the potentials that host them, rather than an a fundamental connection between star formation and global disk processes.

#### The $\Sigma_{\text{SFR}} - \Sigma\Omega$ Correlation

Figure 15 summarizes the behavior of the functions  $\Omega_{\text{disk}}$ ,  $\Omega_{\text{NFW}}$ ,  $\Omega_{\text{H}}$ , and  $\Omega_{\text{iso}}$ . In the Hernquist (1990) and Navarro et al. (1996) halo potential models, the disk scale length-to-halo scale radius ratios were set to  $R_d/r_s = 0.1$  appropriate for observed spiral galaxies. The quantity  $\Sigma(R)^{1.5} \propto \Sigma_{\text{SFR}}$  is plotted as a function of the product  $\Sigma(R)\Omega(R)$ , normalized to the disk properties at the scale length  $R_d$  over the radial range  $R = [0, 5R_d]$ , for the potentials calculated in this Appendix. The quantity  $\Sigma\Omega$  closely tracks  $\Sigma^{1.5}$  throughout the disk, demonstrating that deviations from the  $\Omega \propto \sqrt{\rho_d}$  correlation are typically  $\sim \mathcal{O}(1)$ . Hence, the  $\Sigma_{\text{SFR}} - \Sigma\Omega$  relation may be understood in terms of the scaling of the local density in exponential disks with the angular frequency of realistic galaxy potentials, rather than some more fundamental relation connecting star formation processes in the ISM with global disk properties. Regions of galaxies with large molecular gas fractions ( $\Sigma_{\text{H}_2} \sim \Sigma_{\text{gas}}$ ) are then expected to follow the  $\Sigma_{\text{SFR}} - \Sigma\Omega$  relation, as demonstrated by our simulations (see §3.4). We note that while a different normalization would reduce the typical deviation from the  $\Sigma^{1.5}$  scaling, the high-density portion of the relation corresponding to the region where the rotation curve is rapidly increasing should produce a shallower relation than  $\Sigma_{\text{SFR}} \propto \Sigma\Omega$ . Weak evidence for this may exist in the available data (e.g., the inner-disk region of Figure 9 of Kennicutt et al. 2007).